

University of Alabama in Huntsville

**LOUIS**

---

Theses

UAH Electronic Theses and Dissertations

---

2020

## **Aerodynamic and heat transfer characteristics of a transonic turbine blade tip with pressure-side film cooling**

Michael Sampson

Follow this and additional works at: <https://louis.uah.edu/uah-theses>

---

### **Recommended Citation**

Sampson, Michael, "Aerodynamic and heat transfer characteristics of a transonic turbine blade tip with pressure-side film cooling" (2020). *Theses*. 365.  
<https://louis.uah.edu/uah-theses/365>

This Thesis is brought to you for free and open access by the UAH Electronic Theses and Dissertations at LOUIS. It has been accepted for inclusion in Theses by an authorized administrator of LOUIS.

**AERODYNAMIC AND HEAT TRANSFER CHARACTERISTICS OF A TRANSONIC  
TURBINE BLADE TIP WITH PRESSURE-SIDE FILM COOLING**

**by**

**MICHAEL SAMPSON**

**A THESIS**

**Submitted in partial fulfillment of the requirements for the degree of  
Master of Science in Mechanical Engineering  
in  
The Department of Mechanical and Aerospace Engineering  
to  
The School of Graduate Studies  
of  
The University of Alabama in Huntsville**

**HUNTSVILLE, ALABAMA**

**2020**

In presenting this thesis in partial fulfillment of the requirements for a master's degree from The University of Alabama in Huntsville, I agree that the Library of this University shall make it freely available for inspection. I further agree that permission for extensive copying for scholarly purposes may be granted by my advisor or, in his/her absence, by the Chair of the Department or the Dean of the School of Graduate Studies. It is also understood that due recognition shall be given to me and to The University of Alabama in Huntsville in any scholarly use which may be made of any material in this thesis.

Michael Sander

(Student signature)

4/20/2020

(Date)

## THESIS APPROVAL FORM

Submitted by Michael Sampson in partial fulfillment of the requirements for the degree of Master of Science in Mechanical Engineering and accepted on behalf of the Faculty of the School of Graduate Studies by the thesis committee.

We, the undersigned members of the Graduate Faculty of The University of Alabama in Huntsville, certify that we have advised and/or supervised the candidate on the work described in this thesis. We further certify that we have reviewed the thesis manuscript and approve it in partial fulfillment of the requirements for the degree of Master of Science in Mechanical Engineering.

Phillip M. Ligrani      04-20-2020      Committee Chair

*Dr. Phillip Ligrani*      (Date)

Jason T Cassibry 4/19/2020

*Dr. Jason Cassibry*

R. G. Frederick      4/18/2020

*Dr. Robert Frederick*

D. Keith Hollingsworth      04/23/2020      Department Chair

*Dr. Keith Hollingsworth*

**Shankar  
Mahalingam**

Digitally signed by Shankar Mahalingam  
DN: cn=Shankar Mahalingam, o=College of  
Engineering, ou=Dean, email=sm0026@uah.edu,  
c=US  
Date: 2020.04.23 14:17:10 -05'00'

College Dean

*Dr. Shankar Mahalingam*

**David Berkowitz**

Digitally signed by David Berkowitz  
DN: cn=David Berkowitz, o=University of Alabama in  
Huntsville, ou=Graduate Dean,  
email=berkowed@uah.edu, c=US  
Date: 2020.04.23 16:55:32 -05'00'

Graduate Dean

*Dr. David Berkowitz*

## **ABSTRACT**

The School of Graduate Studies  
The University of Alabama in Huntsville

Degree Master of Science in Engineering


Program Mechanical Engineering

Name of Candidate Michael Sampson

Title Aerodynamic and Heat Transfer Characteristics of a Transonic Turbine Blade Tip with Pressure-Side Film Cooling

Currently, there is a deficit of experimental data for surface heat transfer characteristics and thermal transport processes associated with tip gap flows, and a lack of understanding of performance and behavior of film cooling as applied to blade tip surfaces. As a result, many avenues of opportunity exist for development of creative tip configurations with innovative external cooling arrangements. Described is the development of experimental facilities, including a Supersonic/Transonic Wind Tunnel and a linear cascade for investigations of aerodynamics and surface heat transfer characteristics of a transonic turbine blade tip with a unique squealer geometry and an innovative film cooling arrangement. Of interest is development of a two-dimensional linear cascade with appropriate cascade airfoil flow periodicity. Included are boundary layer flow bleed devices, downstream tailboards, and augmented cascade inlet turbulence intensity. The present linear cascade approach allows experimental configuration parameters to be readily varied. Tip gap magnitudes are scaled so that ratios of tip gap to inlet boundary layer thickness, ratios of tip gap to blade axial chord length, and ratios of tip gap magnitudes to blade true chord length match engine hardware configurations. Ratios of inlet boundary layer thickness to tip gap range from 3 to 5. An innovative, compound angle film cooling configuration is utilized for one blade tip configuration. With these experimental components, results are presented for engine representative transonic Mach numbers, Reynolds numbers, and film cooling parameters, including density ratios, which are achieved using foreign gas injection with carbon dioxide. Transient, infrared thermography approaches are employed to measure spatially-resolved distributions of surface heat transfer coefficients, adiabatic surface temperature, and adiabatic film

cooling effectiveness. Presented are experimental measurements and spatially resolved surface distributions of dimensional heat transfer coefficient, heat transfer coefficient ratio, and different types of adiabatic film cooling effectiveness. These results show differing behaviour depending on the film cooling flow condition, including film cooling blowing ratios which are varied from 0.49 to 3.85. These data also show significant variations spatially along the surface including along the suction side squealer rim, along the pressure side squealer rim, and within the squealer recess region. Film cooling effectiveness data at these locations increase to values as high as 0.08 for blowing ratios of 2.01, 3.18, and 3.85. With a blowing ratio of 3.18, the heat transfer coefficient data varied as much as 30 percent relative to the baseline data with no film cooling.

Abstract Approval:	Committee Chair	Phillip M. Ligrani	04/22/2020
		<i>Dr. Phillip Ligrani</i>	
	Department Chair		04/23/2020
		<i>Dr. Keith Hollingsworth</i>	
	Graduate Dean	David Berkowitz	<small>Digitally signed by David Berkowitz DN: cn=David Berkowitz, o=University of Alabama in Huntsville, ou=Graduate Dean, email=berkowitz@uah.edu, c=US Date: 2020.04.23 16:55:50 -05'00'</small>
		<i>Dr. David Berkowitz</i>	

## **ACKNOWLEDGEMENTS**

I would like to sincerely thank my advisor Dr. Phillip Ligrani for his valuable guidance and support to successfully complete this thesis. I would also like to thank to Hongzhou Xu from Solar Turbines, Inc. for sponsoring this project. I would like to thank my teammates Hallie Collopy, Erin McNabb, Jacob Moseley, Avery Fairbanks, Jonothan Autrey, Chandler Larson, Kyle Goethals, Matthew Cox, and Amy Symmonds for helping me with the experimental procedures and data analysis. I would like to thank Dan Jones for his help with the high pressure piping, compressor maintenance, and troubleshooting of electronic components. I would also like to thank Austin Click for helping with the infrared thermography setup. I would like to thank my wife, family, and friends for their continued support.



## TABLE OF CONTENTS

	Page
List of Figures .....	x
List of Symbols .....	xiv
List of Subscripts .....	xv
I. INTRODUCTION	
1.1 Overview .....	1
1.2 Literature Survey .....	2
1.3 Present Investigation .....	5
1.4 Organization of the Thesis .....	6
II. EXPERIMENTAL APPARATUS AND PROCEDURES	
2.1 SuperSonic/TranSonic/WindTunnel (SS/TS/WT) .....	7
2.2 Test Facility .....	13
2.3 Measurement of Experimental Parameters .....	21
2.4 Film Cooling Supply, Conditions, and Parameters .....	22
2.5 Pressure Measurement Techniques .....	29
2.6 Temperature Measurement Techniques .....	34
2.7 Heat Transfer Measurement Techniques .....	34
2.8 Experimental Uncertainty Magnitudes .....	37
III. EXPERIMENTAL RESULTS	
3.1 Experimental Test Conditions .....	38
3.2 Mach Number and Pressure Ratio Distributions .....	39
3.3 Blade Film Cooling Geometry .....	47
3.4 Baseline Data with Comparisons .....	50
3.5 Data Defects .....	53
3.6 Data for BR=3.18 .....	57

3.7	Comparison of First Type of Film Cooling Effectiveness .....	61
3.8	Comparison of Second Type of Film Cooling Effectiveness .....	64
IV.	SUMMARY AND CONCLUSIONS	
6.1	Summary and Conclusions .....	67
	APPENDIX A: Experimental Conditions.....	69
	APPENDIX B: Data File Directory .....	79
	APPENDIX C: Software Directory .....	84
	REFERENCES .....	85

## LIST OF FIGURES

Figure	Page
1 Schematic diagram of high pressure and low pressure piping supply systems for the SS/TS/WT – SuperSonic/TranSonic/WindTunnel at the University of Alabama in Huntsville.....	1
2 Schematic diagram of high pressure and low pressure piping supply systems for the SS/TS/WT – SuperSonic/TranSonic/WindTunnel at the University of Alabama in Huntsville.....	4
3 Air supply system for the SS/TS/WT – SuperSonic/TranSonic/WindTunnel. (a) 2500 psia portion of the high-pressure piping system. (b) 300 psia portion of the high-pressure piping system. (c) Low-pressure 300 psia piping system.....	7
4 Photograph of laboratory test cell with wind tunnel test sections. On the right is a supersonic flow test section employed for investigation of supersonic flows with different types of shockwaves.....	8
5 Inlet ducting and flow management apparatus for turbine blade cascade wind tunnel branch.....	9
6 Cascade dimensions. Dimensions are in mm.....	11
7 Three-dimensional view of the linear cascade.....	12
8 Downstream-looking view of the entrance of the linear cascade. ....	13
9 Details of two circumferential bleed slots. ....	14
10 Photograph of assembled linear cascade.....	15
11 Fully assembled turbine blade cascade instrumented to measure pressure distributions. ....	15
12 FLIR camera mounted on top of the turbine blade cascade for use in film cooling heat transfer experiments.....	16
13 Thermocouple routing box used to protect fragile thermocouple wires during wind tunnel tests. ....	22
14 System employed to supply cooled carbon dioxide film cooling air to the instrumented blade.....	23

15	Cross-section view of sonic orifice device. ....	16
16	Mounting hole arrangement, Blade span, and squealer recess depth as shown on the 90% span pressure measurement turbine blade. These dimensions are the same for every blade presented in this experiment. Dimensions are in mm. ....	16
17	Instrumented central film cooled turbine blade. ....	16
18	Cut-away view of the plenum within the instrumented airfoil, used to supply film cooling flow. ....	16
19	Locations of tip surface thermocouples, used for <i>in situ</i> calibration of infrared camera images. ....	16
20	Transparent view of the film cooling turbine blade equipped with film cooling passages, thermocouple passages, plenum, and plenum pressure taps. ....	16
21	Film cooling hole orientation and wall thickness. Dimensions are in mm. ....	16
22	Pressure side pressure tap locations. Dimensions are in mm. ....	16
23	Suction side pressure tap locations. Dimensions are in mm. ....	16
24	Blade tip pressure tap locations. Dimensions are in mm. ....	16
25	End wall static pressure tap arrangement. Dimensions are in mm. ....	16
26	Schematic diagram of laboratory arrangement employed for transient, spatially-resolved surface heat transfer measurements for the present turbine blade tip configuration. ....	16
27	Example of variation of local heat flux with surface temperature for one test surface location during a typical transient test seen in Zhang et al. (2011) ....	16
28	Pressure variations with time during a typical blow down experiment. ....	16
29	Central blade isentropic Mach number distributions at 50 percent span. (a) Suction surface. (b) Pressure surface. ....	16
30	Central blade isentropic Mach number distributions at 90 percent span. (a) Suction surface. (b) Pressure surface. ....	16
31	Blade tip pressure tap locations. Dimensions are in mm. ....	16
32	Squealer recess blade measurements. (a) Total to static pressure ratio. (b) Isentropic Mach number. ....	16
33	End wall static pressure tap arrangement. Dimensions are in mm. ....	16
34	Total to static pressure ratio for 0.5 axial chord lengths downstream of the trailing edges of the blades. ....	16

35	Total to static pressure ratio for 1.0 axial chord length downstream of the trailing edges of the blades. ....	16
36	Isometric view of the pressure side film cooled turbine blade model with the B1 film cooling configuration. ....	16
37	Transparent top view of the pressure side film cooled turbine blade model with the B1 film cooling configuration. ....	16
38	Detailed, transparent top view of the film cooling geometry of the B1 film cooling configuration. ....	16
39	Detailed, transparent pressure side view of the film cooling hole geometry of the B1 film cooling configuration. ....	16
40	Heat transfer coefficient data 2020-01-07-1835 c0 baseline data, no film cooling, with BR=0 and a tip gap of 1.4 mm for the B1 film cooling configuration. ....	16
41	Heat transfer coefficient data 2020-01-12-1520 c0 baseline, no film cooling, with BR=0 and a tip gap of 1.4 mm for the B1 film cooling configuration. ....	16
42	Numerically-predicted result. Aerothermal Performance of Shroudless Turbine Blade Tips with Relative Casing Movement Effects (A. S. Viridi, Q. Zhang, L. He, H. D. Li, R. Hunsley), Journal of Propulsion and Power, January 2015 .....	16
43	Experimentally-measured result. Aerothermal Performance of Shroudless Turbine Blade Tips with Relative Casing Movement Effects (A. S. Viridi, Q. Zhang, L. He, H. D. Li, R. Hunsley), Journal of Propulsion and Power, January 2015.....	16
44	Blade tip thermocouple insert locations for the B1 film cooling configuration. ....	16
45	(a) Top view showing thermocouple locations and (b) exact thermocouple locations, measured in the axial direction. ....	16
46	Local errors due to thermocouple installation. ....	16
47	Local error due to scratch on zinc selenide viewing window. ....	16
48	Heat transfer coefficient data 2020-01-12-1445 c23 with BR=3.18 and a tip gap of 1.4 mm for the B1 film cooling configuration. ....	16
49	Heat transfer coefficient ratio data 2020-01-12-1445 c23 with BR=3.18 and a tip gap of 1.4 mm for the B1 film cooling configuration. ....	16
50	Adiabatic film cooling effectiveness data 2020-01-12-1445 c23 with BR=3.18 and a tip gap of 1.4 mm for the B1 film cooling configuration. ....	16

51	Adiabatic film cooling effectiveness data 2020-01-12-1445 c23 with BR=3.18 and a tip tap of 1.4 mm for the B1 film cooling configuration.....	16
52	Adiabatic film cooling effectiveness data 2020-01-12-1320 c16 with BR=0.49 and a tip gap of 1.4 mm for the B1 film cooling configuration.....	16
53	Adiabatic film cooling effectiveness data 2020-01-07-1930 c15 with BR=1.12 and a tip gap of 1.4 mm for the B1 film cooling configuration.....	16
54	Adiabatic film cooling effectiveness data 2020-01-12-1350 c18 with BR=2.01 and a tip gap of 1.4 mm for the B1 film cooling configuration.....	16
55	Adiabatic film cooling effectiveness data 2020-01-12-1505 c26 with BR=3.85 and a tip gap of 1.4 mm for the B1 film cooling configuration.....	16
56	Adiabatic film cooling effectiveness data 2020-01-12-1320 c16 with BR=0.49 and a tip gap of 1.4 mm for the B1 film cooling configuration.....	16
57	Adiabatic film cooling effectiveness data 2020-01-07-1930 c15 with BR=1.12 and a tip gap of 1.4 mm for the B1 film cooling configuration.....	16
58	Adiabatic film cooling effectiveness data 2020-01-12-1350 c18 with BR=2.01 and a tip gap of 1.4 mm for the B1 film cooling configuration.....	16
59	Adiabatic film cooling effectiveness data 2020-01-12-1505 c26 with BR=3.85 and a tip gap of 1.4 mm for the B1 film cooling configuration.....	16
A1	(a) Constants for facility and (b) measured information for 2020-01-12-1320 c16 data. ....	118
A2	(a) Film cooling calculations and (b) variable properties for 2020-01-12-1320 c16 data. ..	118
A3	(a) Constants for facility and (b) measured information for 2020-01-07-1930 c15 data. ....	118
A4	(a) Film cooling calculations and (b) variable properties for 2020-01-07-1930 c15 data. ..	118
A5	(a) Constants for facility and (b) measured information for 2020-01-12-1350 c18 data. ....	118
A6	(a) Film cooling calculations and (b) variable properties for 2020-01-12-1350 c18 data. ..	118
A7	(a) Constants for facility and (b) measured information for 2020-01-12-1445 c23 data. ....	118
A8	(a) Film cooling calculations and (b) variable properties for 2020-01-12-1445 c23 data. ..	118
A9	(a) Constants for facility and (b) measured information for 2020-01-12-1505 c26 data. ....	118
A10	(a) Film cooling calculations and (b) variable properties for 2020-01-12-1505 c26 data...	118

## LIST OF SYMBOLS

BR	film cooling blowing ratio
$C_D$	discharge coefficient
$C_x$	axial chord length
$\dot{m}_c$	coolant mass flow rate
$d_c$	film cooling hole diameter
$\rho_c$	coolant density
$\rho_m$	main flow density
R	ideal gas constant
N	number of items
$d_c$	film cooling hole diameter
h	iso-energetic heat transfer coefficient
$h_{NFC}$	heat transfer coefficient with no film cooling
$M_c$	coolant Mach number
$A_c$	area of each film cooling hole
$\dot{q}_o''$	wall heat flux
$Re_c$	film coolant Reynold's number
T	temperature
$V_c$	average coolant flow velocity for one film cooling hole
$V_m$	main flow local freestream velocity
$\gamma$	ratio of specific heats
$\eta_{AD-corrected}$	first type of adiabatic film cooling effectiveness
$\eta_{AD-corrected-new}$	second type of adiabatic film cooling effectiveness

## LIST OF SUBSCRIPTS

$x$	axial coordinate
AW-FC	adiabatic wall value with film cooling
AW-NFC	adiabatic wall value without film cooling
$c$	film cooling value or coolant value
$m$	main flow value
$s$	static flow value
$t$	stagnation flow value
$0$	stagnation value
$W$	surface value
avg	average value
ideal	ideal value
inlet	inlet value



# CHAPTER 1

## INTRODUCTION

### 1.1 Overview

Flow within the gap between the turbine blade and the casing of a transonic gas turbine engine is extremely complex because of significant local and overall flow unsteadiness, increased local flow mixing, three-dimensionality, local flow skewing, excessive magnitudes of local flow shear, local flow separation regions, local flow reversals, as well as oblique and normal shock waves, including families of oblique shock waves. Such characteristics make understanding and investigating associated thermal processes, thermal transport, and surface heat transfer variations a challenge. In addition, for many configurations, design challenges result because of compromises which must be made to simultaneously reduce both aerodynamic losses and surface thermal loading. This is because attempts to satisfy these two goals may give opposite and contradictory overall turbine component performance characteristics. For example, component and flow condition alterations, which decrease aerodynamic losses downstream of a tip gap, may increase surface thermal loading, and component and flow condition alterations, which decrease surface thermal loading, may increase aerodynamic losses. This includes the use of film cooling, which must be employed with innovative designs and conditions, in order to optimize the aerodynamic and thermal performance of a particular turbine blade tip and the associated tip gap. The present investigation is motivated by such considerations. Employed is one unique film cooling arrangement, whose goal is to improve the thermal protection of surfaces as they are exposed to a complex and challenging flow environment.

Tip clearances within turbines are required because thermal-mechanical constraints require engine manufacturers to use unshrouded blades, and because these unshrouded blades require a tip clearance to avoid striking the casing. Such constraints include the effects of increasing the rotational speed of shrouded blades. With such tip clearances or tip gaps present, the resulting over-tip leakage flow has high velocity and high temperature, leading to high local heat transfer rates and large material surface temperature gradients on the tip, as well as aerodynamic losses. At engine-scale conditions typical of a single-stage high-pressure aero-engine turbine, a large proportion of the tip flow is transonic. This means that shock waves form within the tip gap,

creating large local pressure gradients, which significantly affect local boundary layer development along the tip. According to Zhang et al. (2011), important variations of surface heat transfer are presented from a family of oblique shock waves, which are subject to repeated reflections. Results from those investigations show virtual visualizations of density gradient distributions associated with oblique and normal shock waves along the leakage flow streamlines direction. Associated surface heat flux distribution on the blade tip surface show the locations of oblique shock waves within the tip gap. As such, there are two main mechanisms that affect the local heat transfer coefficient on the tip. These are first shear stress, which is largely set by the boundary-layer thickness, and the second is turbulent mixing, which is affected by local streamwise pressure gradient. Underneath each oblique shock reflection, the boundary-layer experiences a large adverse pressure gradient, which leads to an increase in turbulence generation. In the reattachment region, after this separation region, heat transfer levels are high because the separation promotes turbulence production. Downstream of the reattachment region, flow is supersonic and accelerates rapidly thus causing a reduction in turbulence, which reduces the heat transfer. Thus, there is a rapid increase in surface heat transfer as the flow above moves across the shock wave. The result is a pattern of high and low tip surface heat transfer stripes, normal to the flow direction, which are due to rapid acceleration and deceleration, which occur prior to and across the shock wave reflections.

## **1.2 Literature Survey**

Additional turbine blade tip investigations, which illustrate surface heat transfer and aerodynamic variations within turbine blade tip gap flows, are numerous. Blade tip arrangements which are employed in these studies utilize squealer tip and smooth blade tip configurations. Squealer tip configurations are investigated by Zhang et al. (2011), Dunn and Haldeman (2000), Green et al. (2005), Key and Arts (2006), Hofer and Arts (2009), Viridi et al. (2013), Wheeler and Saleh (2013), Li et al. (2014), Wang et al. (2015), Zhou (2015), Jung et al. (2016), Kim et al. (2016), Arisi et al. (2016), Ma et al. (2017), Zhu et al. (2017), and Kim et al. (2019). Smooth blade tips are investigated by Thorpe et al. (2005), Green et al. (2005), Key and Arts (2006), O'Dowd et al. (2010, 2011), Wheeler et al. (2011), Zhang et al. (2011), Shyam et al. (2011) Atkins et al. (2012), Wheeler and Saleh (2013), Anto et al. 2013, Viridi et al. (2013), Wheeler and Sandberg (2013), Li et al. (2014), Zhang et al. (2014), Zhang and He (2014), Wang et al. (2015), Zhou

(2015), Jung et al. (2016), Gao et al. (2017), and Kim et al. (2019). Most of these investigations (which involved experimental measurements) employ annular or linear cascades with stationary blades.

Discussed here are past studies which consider the aerodynamics for transonic turbine blades with both flat and squealer tip arrangements. Zhang et al. (2011) utilize both smooth and squealer-tipped blades with three different tip gaps in a transonic heat transfer experiment. From their spatially resolved temperature profiles produced by infrared thermography, they show that thermal signatures toward the leading and trailing edges are more pronounced as tip gap increases. Dunn et al. (2000) use 9 heat flux gauges to determine the Nusselt number for a recessed squealer tipped blade under transonic flow conditions in a full scale engine environment. They find that the highest Nusselt number is on the suction side near the blades trailing edge. Green et al. (2005) attempt to fill the gap of capabilities of current CFD software to account for complex geometry (such as squealer rims) and validate it with experimental data. Their research involves flat and squealer tipped blades at transonic Mach numbers. They find that shroud pressure and velocity remains similar for both geometries except at the 60% span location. The CFD under-predicts the accelerations at the 90% span location near the shock, but compares well for the remainder of the surface. Hofer and Arts (2009) investigate the aerodynamics of a squealer tip in a transonic flow regime. Contrary to established flat blade tip behavior, the squealer tip proves to reduce leakage jet velocity and is not as sensitive to Reynolds number changes. Wheeler and Saleh (2013) present experimental results which examine the effect of cooling injection on transonic tip flows for both squealer and flat tipped blades. Their experiment proves that at cooling mass flows above 2% of the main flow, a squealer-tipped blade experiences more aerodynamic loss than the flat-tip. Li et al. (2014) present results from a numerical investigation of the effect of squealer cavity depth on flow characteristics. They show that the cavity depth affects the subsonic leakage flow losses more than the supersonic region. Simulated relative casing motion has much more impact on subsonic flow than transonic flow. Jung et al. (2016) provide numerical analysis data which compares the aerodynamics of transonic blades with flat, curved, and squealer-tipped geometry. Their simulation shows that a squealer with a cutback applied to the trailing edge shows the least aerodynamic losses.

Discussed here are past studies which consider heat transfer measurements for transonic turbine blades with both flat and squealer tip arrangements. Viridi et al. (2013) investigate the

aerothermal performance of a flat and squealer tipped transonic turbine blade with different tip gaps. They show that the front 50% of the blade is subsonic and the heat transfer coefficient increases with tip gap, while the opposite trend applies to the aft 50% due to the flow being supersonic. Shyam et al. (2011) analyze the unsteady heat transfer of a flat blade tip and the endwall in a highly loaded transonic turbine stage. Their experiment shows that the flow chokes at the aft 70% portion of the blade. They also identify hot spots on the pressure side leading edge and on both sides of the trailing edge. In addition, the heat transfer seems more dependent on shear ratio than pressure ratio. Wang et al. (2015) perform numerical investigation of the impact of cooling injection on the transonic over-tip leakage flow and squealer aerothermal design optimization. Their simulation ranks the performance of plane-tip and squealer-tipped blades with added cooling. They find that a flat tip is shown to perform better than a squealer tip in terms of thermal load without the added losses associated to tip leakage flow. Zhang et al. (2014) investigate the effect of inlet turbulence on a transonic linear cascade with flat blade tips. The experiment confirms Wheeler's study of effect of inlet turbulence. They find that as the inlet turbulence intensity increases, the tendency for the tip leakage vortex to reattach on the suction side surface decreases. They also show that a lower turbulence intensity results in a higher heat transfer along the suction side near the trailing edge. Anto et al. (2013) examine the effects of tip gap and exit Mach number on turbine blade tip and near-tip heat transfer for a flat-tipped blade. They utilize oil flow visualization, thin film gauges to measure heat flux, and infrared thermography. Exit Mach numbers are 0.7, 0.85, and 1.05. The maximum heat transfer in all cases is on the suction side caused by the tip leakage vortex at 94% span at  $s/C=0.66$ . They attribute the high heat transfer in this area to leakage flow separation. Leakage flow vortices on the suction side dominate the heat transfer.

Discussed here are past studies which consider heat transfer measurements with film cooling for transonic turbine blades with both flat and squealer tip arrangements. Zhu et al. (2017) discuss a CFD simulation which assesses the rotating effect on transonic squealer tip cooling performance. Compared to the stationary casing, they find that the pressure side film cooling injection with a moving casing reduces the heat transfer region on the cavity floor and substantially increases the blade tip film cooling effectiveness. Investigations by O'Dowd et al. (2010) present experimental results where heat transfer on a flat-tipped transonic turbine blade is measured with three different tip gaps and utilize infrared thermography to produce a spatially resolved

temperature profile. Their results show that the thermal signatures along the leading and trailing edges of airfoils increase with tip gap. Zhou (2015) and Ma et al (2017) present experimental results for transonic, squealer tipped blades. They explain that in the presence of pressure-side film cooling holes, stripes of high and low film cooling effectiveness show on a spatially-resolved plot of the blade tip. Ma et al. (2017) also conclude that more film cooling holes are not always more effective, as cooling injection in certain locations do not benefit the heat transfer distribution. Kim et al. (2016) investigate the optimization of a high pressure, transonic turbine blade cavity with conjugate heat transfer analysis. Their experiment uses depth, front blend radius, and aft blend radius of the cavity as design variables. They perform experiments on 30 different configurations, all having cooling holes down the span of the blade and dusting holes on the tip, and show that the blade without a cavity is advantageous from a heat transfer perspective. However, the total pressure loss coefficient increases over 5% for this configuration. O'Dowd et al. (2011) compare different methods for analyzing infrared thermography data for heat transfer analysis experiments. They conclude that the Impulse method has the lowest uncertainty and that transient data has the most consistent results using heat flux reconstruction methods.

### **1.3 Present Investigation**

Within the present test facility, investigated are spatially-resolved distributions of surface adiabatic film cooling effectiveness and surface heat transfer coefficients for a transonic turbine blade tip. The tip contains a squealer rim, and a single row of film cooling holes is located on the pressure-side of the blade very near to the blade tip. Also measured are surface static pressure distributions, and associated isentropic Mach numbers, around the blade surface at the 50 percent airfoil span location, around the blade surface at the 90 percent airfoil span location, the blade tip, and the endwall. A two-dimensional linear cascade is employed with four flow passages and five complete blades is employed, which includes radial and circumferential boundary layer flow bleed devices, and an inlet grid to augment cascade inlet passage turbulence intensity. The cascade is designed to provide geometric similarity with the engine application environment, including inlet boundary layer thickness, blade configuration (including blade axial chord length, and blade true chord length), cascade arrangement (including blade pitch, blade span, and inlet flow angle), blade tip geometry, squealer depth, squealer wall thickness, and tip gap magnitudes.

## **1.4 Organization of the Thesis**

The present thesis is composed of 4 chapters, 4 appendices, and a reference list. Chapter 2 presents the SuperSonic/TranSonic/WindTunnel (SS/TS/WT), test facility, measurement of experimental parameters, film cooling supply, pressure measurement techniques, and heat transfer measurement techniques. Portions of the material in Chapter 2 (as well as other parts of the thesis) are taken verbatim from Collopy et al. (2020) and Sampson et al. (2019). Chapter 3 presents experimental data for Mach number profiles and spatially-resolved distributions of surface adiabatic film cooling effectiveness and surface heat transfer coefficient. Chapter 4 presents the summary and conclusions of the thesis. Appendix A presents an uncertainty analysis. Appendix B presents a data file directory. Appendix C presents the software directory.

## **CHAPTER 2**

### **EXPERIMENTAL APPARATUS AND PROCEDURES**

Presented in the present chapter are discussions of the SuperSonic/Transonic/WindTunnel (SS/TS/WT), test facility, measurement of experimental parameters, pressure measurement techniques, and heat transfer measurement techniques.

#### **2.1 SuperSonic/TranSonic/WindTunnel (SS/TS/WT)**

The wind tunnel is a blow-down facility. The working fluid is dried air. The facility is comprised of a high-pressure piping system, a low-pressure piping system, two test section assemblies, and exhaust piping. Compressors, air storage tanks, ball valves, knife gate valves, spectacle blind valves, pressure relief valves, burst disks, analog pressure gauges, digital pressure transducers, and an air diverter plenum control the air in the high and low-pressure piping systems. The many components in this system allow it to produce a wide variety of conditions for different testing environments.

The high-pressure piping system connects to the low-pressure piping system. A spectacle blind valve is used to isolate the air in the high-pressure piping system from the air in the low-pressure piping system. Figures 1 and 2 show schematic diagrams of high pressure and low pressure piping supply systems for the SS/TS/WT – SuperSonic/TranSonic/WindTunnel. With this newly developed and fully operational facility, extensive test capabilities are provided, which allow either: (i) rapid change of test conditions, with extensive number of tests in a single day, or (ii) very long testing times for measurements requiring extended testing times. The current facility has an air supply capability of 50 cubic meters, which, ordinarily, is comprised of 32 cubic meters of air supplied at 300 psia and 18 cubic meters of air supplied at 2500 psia.

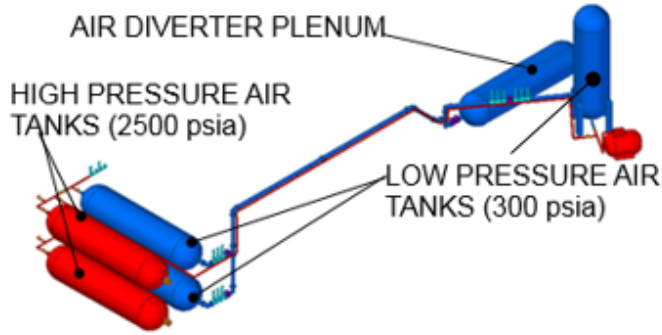


Figure 1. Schematic diagram of high pressure and low pressure piping supply systems for the SS/TS/WT – SuperSonic/TranSonic/WindTunnel at the University of Alabama in Huntsville.

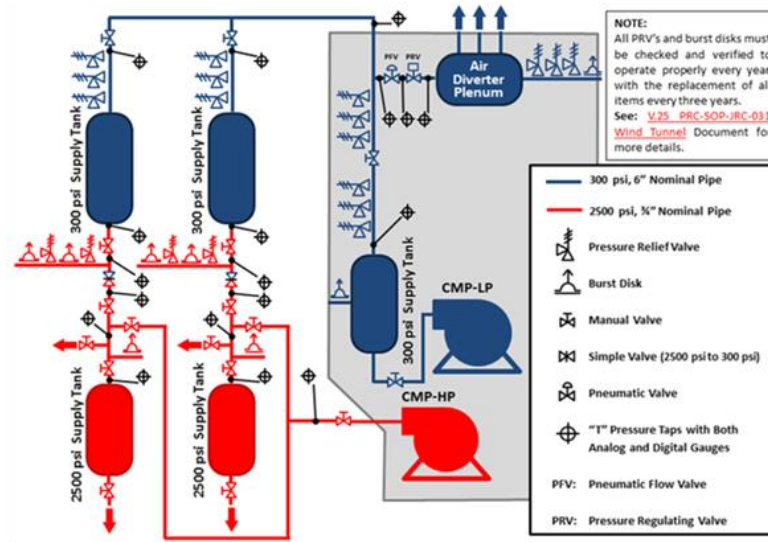


Figure 2. Schematic diagram of high pressure and low pressure piping supply systems for the SS/TS/WT – SuperSonic/TranSonic/WindTunnel at the University of Alabama in Huntsville.



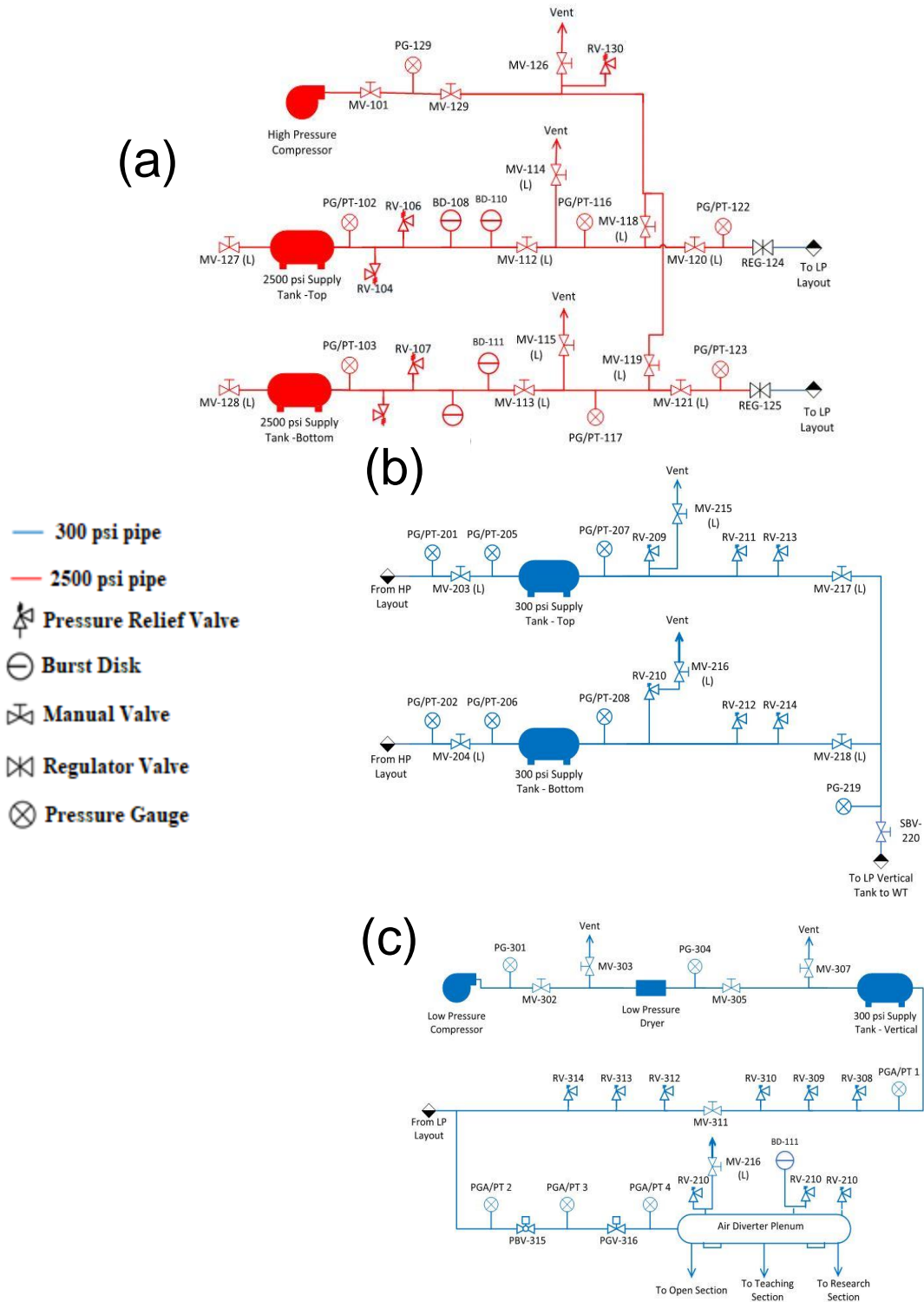


Figure 3. Air supply system for the SS/TS/WT – SuperSonic/TranSonic/WindTunnel. (a) 2500 psia portion of the high-pressure piping system. (b) 300 psia portion of the high-pressure piping system. (c) Low-pressure 300 psia piping system.

With this arrangement, the 2500 psia air supply is employed to replenish the 300 psia air supply, so that (i) and (ii) are easily implemented. Within Figures 1, 2, and 3a-c, blue items denote 300 psia air supply items, and red items denote 2500 psia air supply items. Figure 3a is a schematic diagram of the 2500 psia portion of the high-pressure piping system. Figure 3b shows a schematic diagram of the 300 psia portion of the high-pressure piping system. Figure 3c shows a schematic diagram of the low-pressure piping system. A legend is also included within Figs. 3a-c to define the symbols used in the schematic diagrams.

The low pressure tanks are used as the primary source of supply pressure during a wind tunnel blow down. To accommodate numerous tests in a single sitting, the high pressure tanks are used to recharge the low pressure tanks between blow downs. This cuts down recharge time from several hours to approximately 10 minutes. This is done by opening all of the valves between one high pressure tank and the low pressure tank(s) that are being recharged. The recharging flow is controlled by a pressure regulator located in front of each low pressure tank. The low pressure tanks can also be recharged using the low pressure compressor by opening all valves in between the low pressure tank(s) that are being charged. This process can take several hours depending on how depleted the tanks are, but allows the recharge of the high pressure tanks using the high pressure compressor simultaneously.

With this facility, cascade geometric scaling, engine representative Mach numbers, and engine representative Reynolds numbers are readily achieved. The facility also includes provision to employ foreign gas cooling (for example, carbon dioxide CO<sub>2</sub> gas) to achieve engine representative film cooling density ratios.

The low-pressure compressor, used to pressurize the low-pressure piping system, is a Quincy QR 350 model BM350HPDT Compressor. A Bauer Compressors BP26-E3 high-pressure compressor pressurizes the high-pressure piping system. Each compressor includes an air dryer and air filters. During testing, flow through the test section is regulated using several different valves. The first is a Southern Controls 330AITFM-CH-SQ pneumatic valve system, which is comprised of a Trueline ball valve, a pneumatic actuator, a switch, and a solenoid. The actuator, switch, and solenoid are manufactured by CSS and have model numbers of VAD09, M, and 4, respectively. Next is the 667-EWT-DVC6200 Fisher pressure regulating valve. The pressure

regulating valve is controlled by a Fisher FIELDVUE DVC6200 Digital Valve Controller. Digital valve controller settings are programmed using a Moore Industries 535 display.

Following these valve systems is an air diverter plenum, with a volume of 14 cubic meters, which ensures that disturbances which occur within the piping system do not propagate into the test section. The diverter plenum has three air output pipes, which lead to three independent test section branches. Only one of the three test section branches is used in the present research effort. The entrances to the other two sections are blocked by a closed spectacle blind valve and by a circular sliding gate valve. Figure 4 shows a photograph of the laboratory test cell with wind tunnel test sections. Shown within this photograph is a supersonic flow test section employed for investigations of supersonic flows with different types of shockwaves. Note that this test section is not employed within the present turbine blade tip investigation. The photograph within Figure 4 is included to illustrate the capabilities of the wind tunnel system.

Following the test section is an exhaust plenum with exhaust ducts and vents attached. These different vents and cuts then direct the exhaust air either outside of the test cell building or elsewhere within the test cell laboratory. Spectacle blind valves are used when needed to block air from passing between exhaust plenums and between different test section branches. Each of the three exhaust ducts, which leads outside of the test cell building, connects to a New York Blower Company A1602302 noise baffling segment.

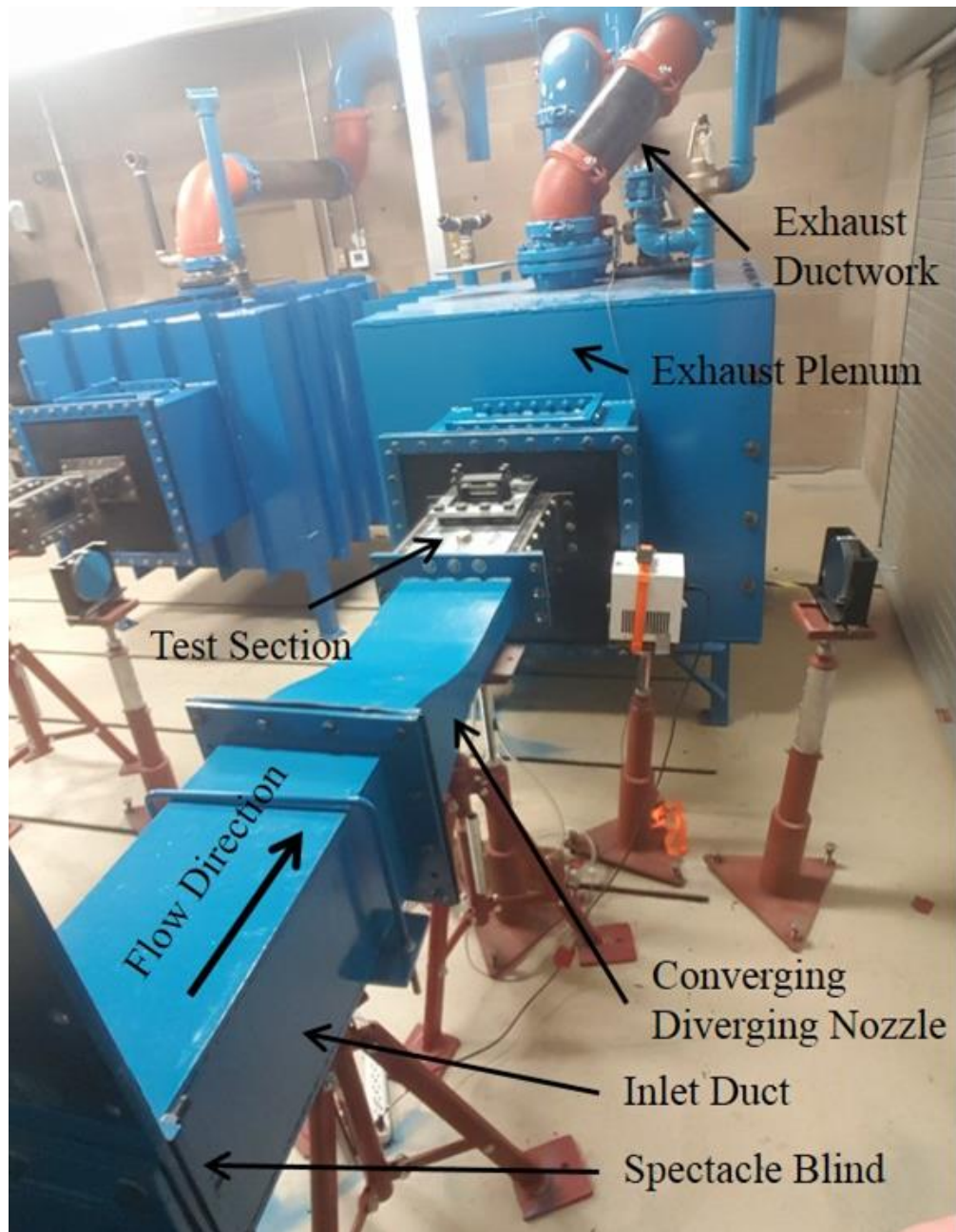


Figure 4. Laboratory test cell with wind tunnel test sections. On the right is a supersonic flow test section employed for investigation of supersonic flows with different types of shockwaves.

## 2.2 Test Facility

Presented in this subsection are discussions of the inlet ducting and transonic turbine blade cascade. Figure 5 presents the inlet ducting and flow management apparatus for the associated turbine blade cascade wind tunnel branch. For all test cases, a bar grid is employed to augment the mainstream turbulence intensity level, to approximately 6 to 7 percent, at the exit of the nozzle, upstream of the test section. Three Kanthol-D wire mesh heaters are also employed within the inlet duct system to generate a timewise step increase in air flow static temperature of the mainstream air, after all facility flow conditions are established. These mesh heaters are connected in series to an Ametek Sorensen SGA60/500D 30 kilowatt DC power supply.

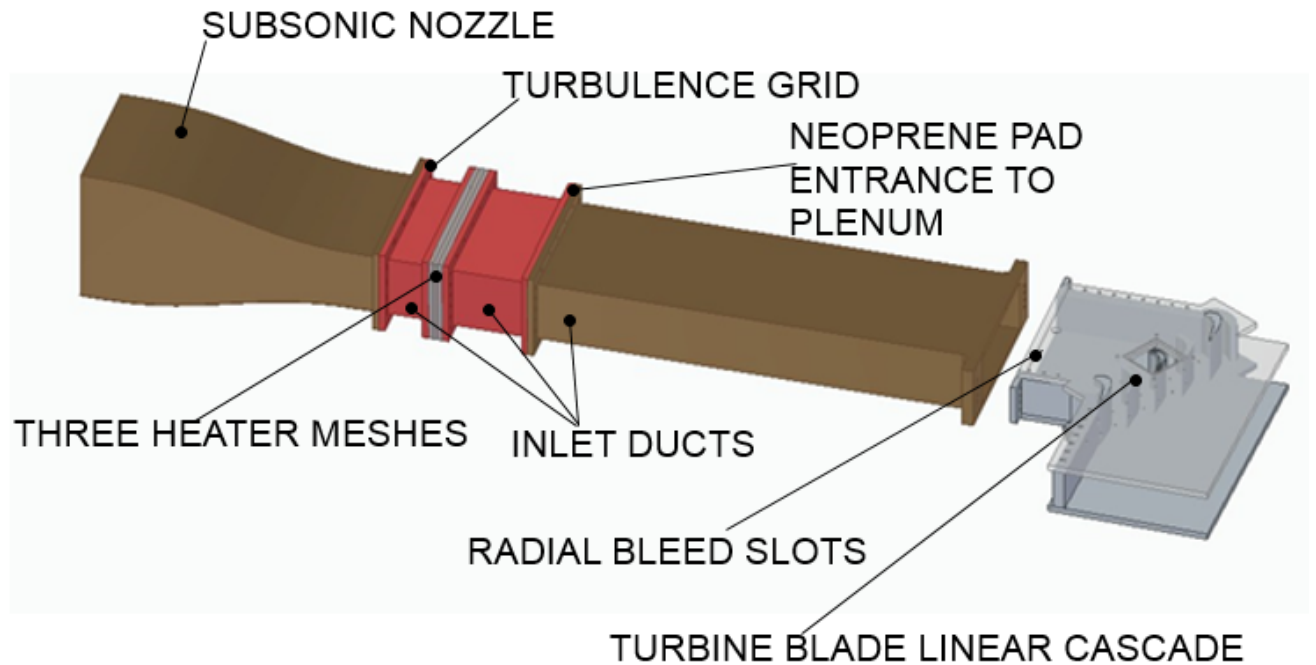


Figure 5. Inlet ducting and flow management apparatus for turbine blade cascade wind tunnel branch.

Figure 6 presents the dimensions for the cascade. Shown in Figures 7 and 8 are three-dimensional schematic views of this linear cascade apparatus. A downstream-looking view of the entrance of this cascade is given in Figure 8, with relative dimensions and locations of the blade tip, the tip gap, and the casing wall. The present tip gap magnitude is 1.40 mm. Details regarding the two circumferential bleed slots are provided in Figure 9. A photograph of the assembled linear cascade is then shown in Figure 10. For the present cascade, 3 complete blades, and 2 half-blades, with 4 complete blade passages are employed. Note that each blade within the linear cascade is

two-dimensional, without additional angularity or twist. The cascade inlet flow angle is 29 degrees. Also included are appropriate boundary layer flow radial and circumferential bleed systems, and tailboard apparatus. Figure 11 shows a photo of the fully assembled cascade, instrumented to measure pressure distributions around the circumference of the central blade. The plastic tubing seen in this photo connect each pressure tap to its own Honeywell FP2000 pressure transducer. Figures 12 and 13 are photos showing the fully assembled cascade, instrumented to measure blade tip surface temperature. Figure 12 shows the FLIR camera in place directly above the zinc selenide viewing window. The camera is attached via a custom-made steel mounting apparatus, complete with mounting holes placed to match the dimensions of the camera's stock mounting location. Figure 13 is a photo showing the thermocouple routing box below the cascade. The type T thermocouples used for *in situ* infrared thermography calibration are very fragile and need to be shielded from the high-speed airflow in the wind tunnel plenum, so they are protected by a thick plastic routing box that is securely attached to the bottom of the cascade.

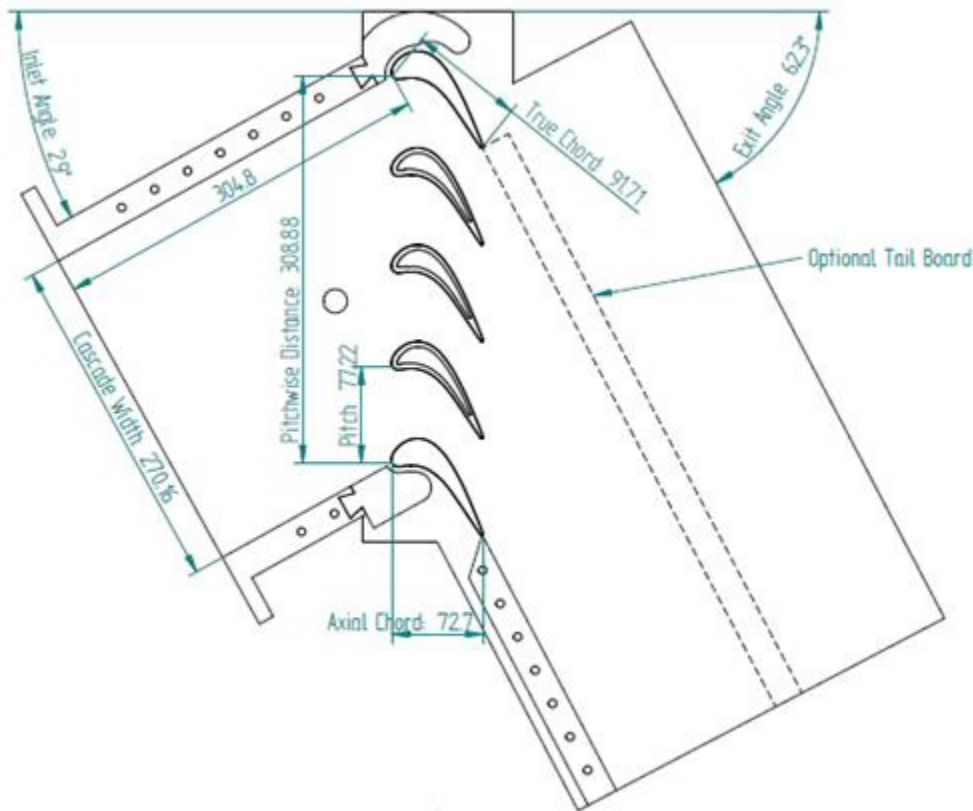


Figure 6. Cascade dimensions. Dimensions are in mm.

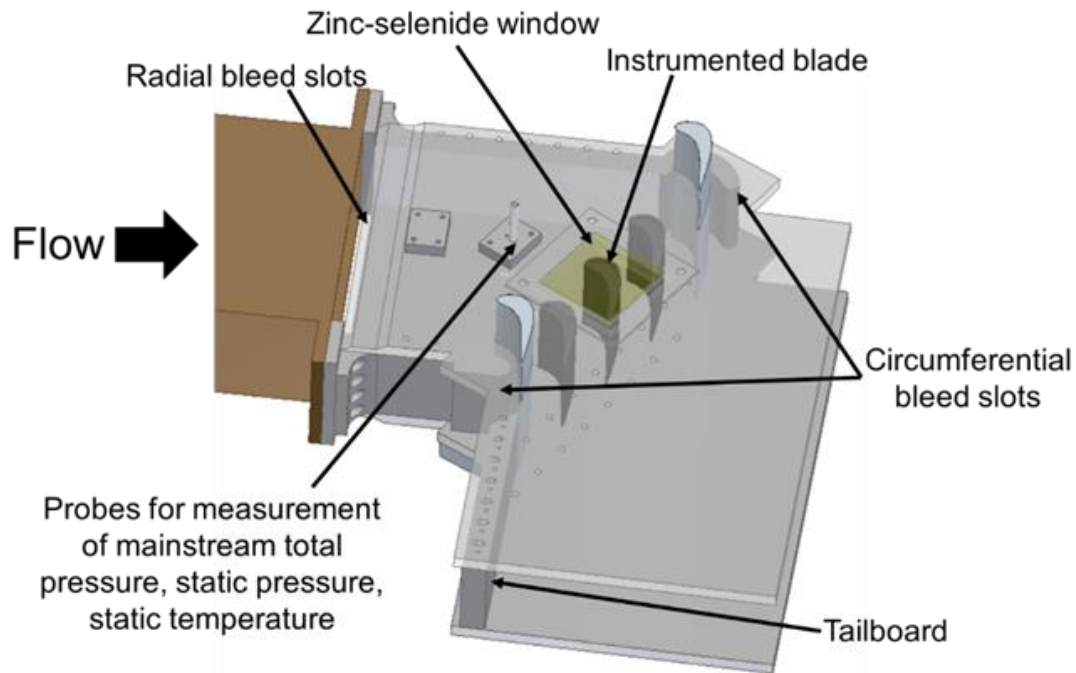


Figure 7. Three-dimensional view of the linear cascade.

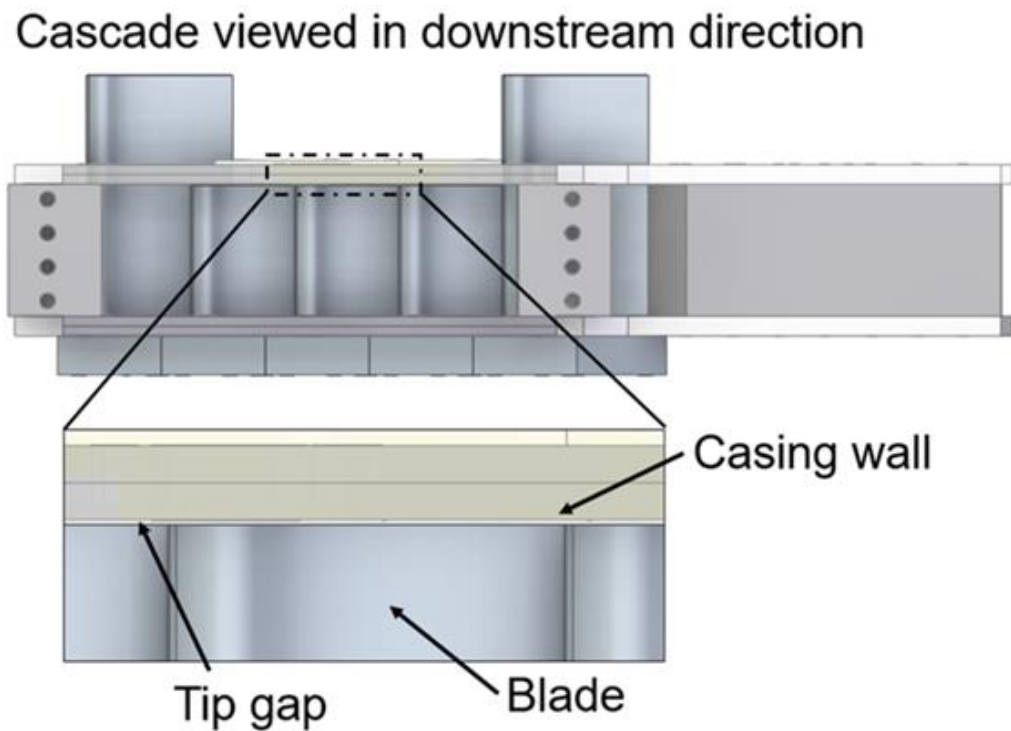


Figure 8. Downstream-looking view of the entrance of the linear cascade.



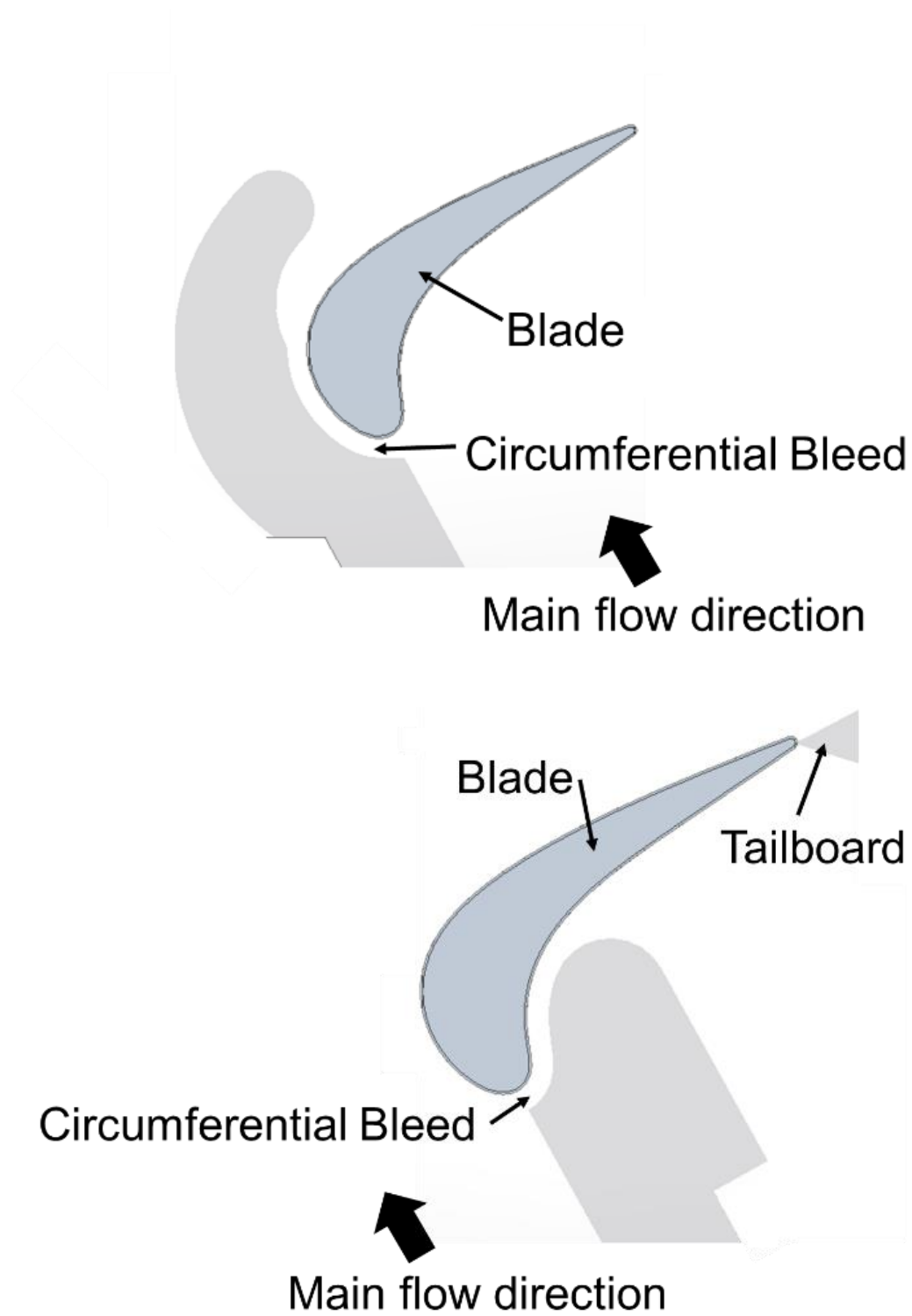


Figure 9. Details of two circumferential bleed slots.





Figure 10. Assembled linear cascade.

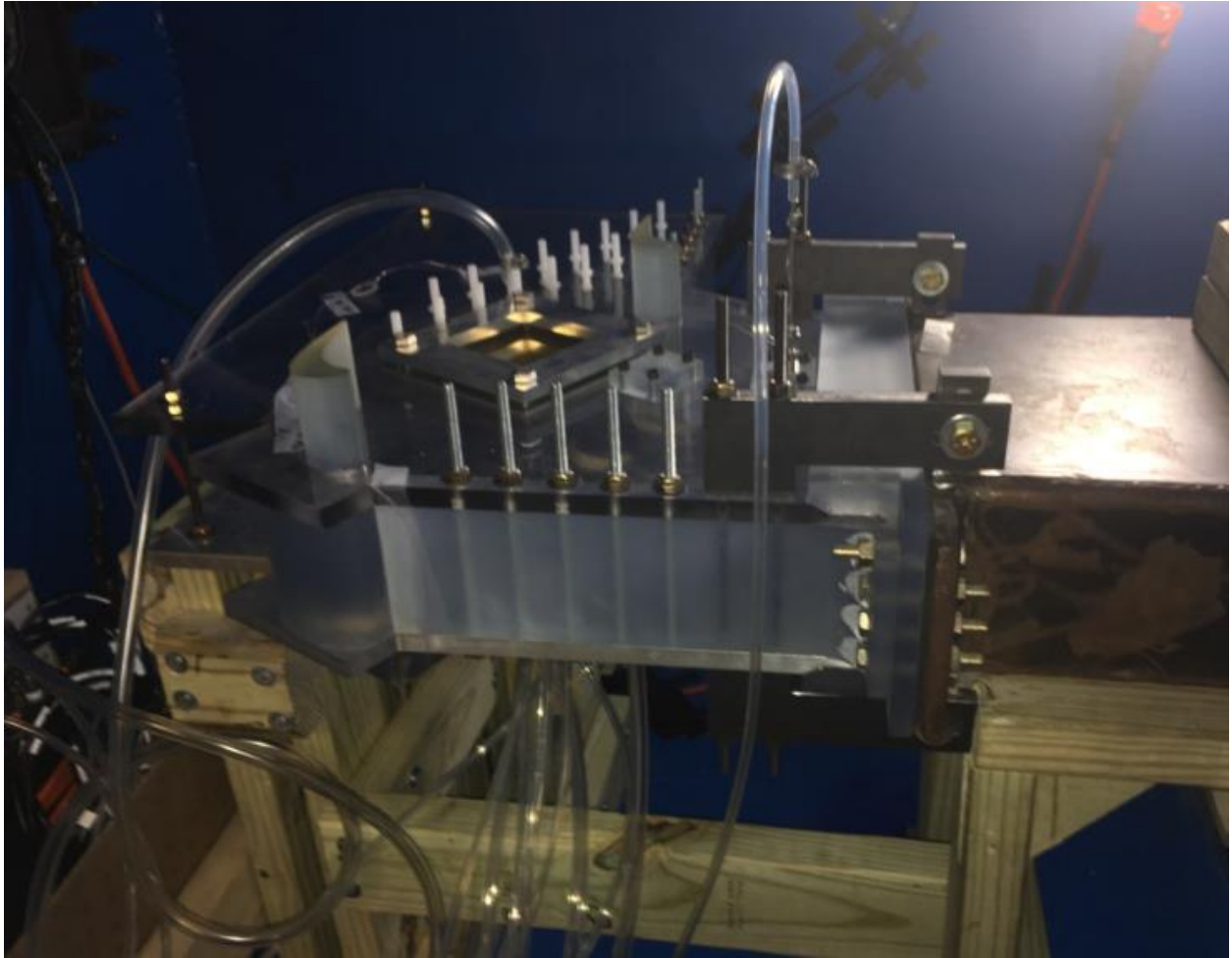


Figure 11. Fully assembled turbine blade cascade instrumented to measure pressure distributions.



Figure 12. FLIR camera mounted on top of the turbine blade cascade for use in film cooling heat transfer experiments.



Figure 13. Thermocouple routing box used to protect fragile thermocouple wires during wind tunnel tests.

A cascade inlet boundary layer thickness is employed, which is produced using an inlet duct of appropriate length located at the entrance to the cascade. Expected values of von Karman shape factor for the inlet boundary layer are expected to be 1.31 to 1.34. With this arrangement, and with the scale factor employed, ratios of inlet boundary layer thickness to tip gap are approximately equal to 3 and 5. As such, tip clearance magnitudes within the experimental apparatus are scaled so that ratios of tip gap to inlet boundary layer thickness, ratios of tip gap magnitudes to blade axial chord length, and ratios of tip gap magnitudes to blade true chord length match engine hardware configurations. Measurement of inlet boundary layer profiles is accomplished using a miniature stagnation pressure probe along with a wall static pressure tapping.

Surface heat transfer characteristics are measured using the transient impulse-response measurement approach, employed with infrared thermography. To create this arrangement, a thermal transient is induced within the flow to provide a step in mainstream temperature after flow characteristics are established. With this approach, spatially-resolved distributions of surface adiabatic film cooling effectiveness and surface heat transfer coefficients are provided for different film cooling flow conditions. Mach numbers, Reynolds numbers, film cooling discharge coefficients, film cooling blowing ratios, film cooling velocity ratios, film cooling momentum flux ratios, and film cooling density ratios match engine environment values. Such representative density ratios are provided by employing carbon dioxide as the film coolant. Both the configuration and experimental conditions employed in the present study are unique, including the film cooling configuration, and squealer blade tip arrangement, which makes the results provided by the present investigation distinctive and different from all past investigations.

## **2.3 Measurement of Experimental Parameters**

With the present experimental arrangement, the facility has the capability to vary a number of different parameters including: tip gap magnitude, squealer depth, film cooling configuration, and all film cooling characterization parameters, for one blade airfoil, with one squealer tip configuration. Note that the same inlet Reynolds number, exit Reynolds number, inlet Mach number, exit Mach number, and turbine blade geometry configuration (as modelled with the linear cascade) are employed for all tests.

The following experimental parameters are measured for each experimental configuration considered.

(1) Spatially-resolved distributions of surface adiabatic effectiveness and surface heat transfer coefficient on the blade tip, and all associated quantities, including flow temperatures and surface temperatures. With infrared thermography, and transient testing techniques, simultaneous measurements are made of spatially-resolved distributions of surface heat transfer coefficient and adiabatic wall temperature within a single blow-down test. From these results, spatially-resolved distributions of adiabatic film cooling effectiveness are determined. Note that the experimental approach requires a means to provide a step in mainstream temperature after flow characteristics are established.

(2) Surface static pressure variations using surface static pressure taps at discrete locations on the blade tip, on the end wall, and at different blade span locations to document blade profile static pressure variations.

(3) Cascade inlet static pressure, inlet stagnation pressure, recovery temperature, and turbulence intensity.

(4) Film cooling mass flow rates, temperatures, static pressures, and all associated quantities to determine all associated film cooling parameters, including local and spatially-averaged magnitudes of discharge coefficients, density ratios, velocity ratios, blowing ratios, and momentum flux ratios. Blowing ratios range from 0.5 to 3.0 to match engine operating conditions.

## **2.4 Film Cooling Supply, Conditions, and Parameters**

In regard to film cooling flow conditions and parameters determination, the mass flow rate for the film cooling is  $\dot{m}$  and is measured upstream of the linear cascade coolant plenum (within the instrumented turbine blade). Figure 14 shows a diagram of the carbon dioxide injection system. The CO<sub>2</sub> flow is set using a pressure regulator attached to the supply tank. The gas flows from the tank, through the regulator, and is metered using a custom-made 3-D printed sonic orifice device, seen in Figure 15. This device chokes the CO<sub>2</sub> flow so the mass flow rate can be accurately calculated. Upstream of the throat, it utilizes a static pressure tap and a hole where a thermocouple is inserted to measure the stagnation temperature. Note that the static pressure upstream of the sonic orifice is also the stagnation pressure at this location.

The stagnation temperature for the film cooling is measured within the coolant supply flow, as  $T_{tc}$ , within the plenum which is located within the blade being tested. The static density of the film coolant  $\rho_c$  is determined using the ideal gas equation of state. The film cooling static pressure

is the same as the local and adjacent freestream value. Next, the film cooling flow velocity is determined using an equation of the form

$$V_c = \dot{m}_c / (\rho_c N_c A_c) \quad (1)$$

where  $A_c$  is the area of each film cooling hole and  $N_c$  is the number of film cooling holes with this hole area. An iterative analysis approach is then employed to determine temperatures which satisfy Eqn. (1) and the associated equation of state relationships. Upon completion of this process, correct values for film cooling flow static density, velocity, and static temperature are determined. Next, the viscosity of the air is calculated using appropriate analytic models. The blowing ratio is then the ratio of local film cooling mass flux to local mainstream mass flux.

Discharge coefficients, blowing ratios, Reynolds numbers, and Mach numbers (where each quantity is spatially-averaged for all film cooling holes of a particular diameter and area), are given by the following equations.

$$C_D = (\rho_c V_c)_{avg} / (\rho_c V_c)_{ideal} = (\dot{m}_c / N_c A_c) / \sqrt{2 \rho_c \Delta P_c} \quad (2)$$

$$BR_{avg} = (\rho_c V_c)_{avg} / (\rho_m V_m)_{avg} = (\dot{m}_c / N_c A_c) / (\rho_m V_m)_{avg} \quad (3)$$

$$Re_{c, avg} = (\rho_c V_c)_{avg} d_c / \mu_c = (\dot{m}_c / N_c A_c) d_c / \mu_c \quad (4)$$

$$M_{c, avg} = (V_c)_{avg} / \sqrt{\gamma R T_c} = (\dot{m}_c / \rho_c N_c A_c) / \sqrt{\gamma R T_c} \quad (5)$$

Within equation (2), the local dynamic pressure  $\Delta P_c$  is the difference between the film supply stagnation pressure, and the local film static pressure, which is the same as the local main flow static pressure at the location of the film cooling hole exits.

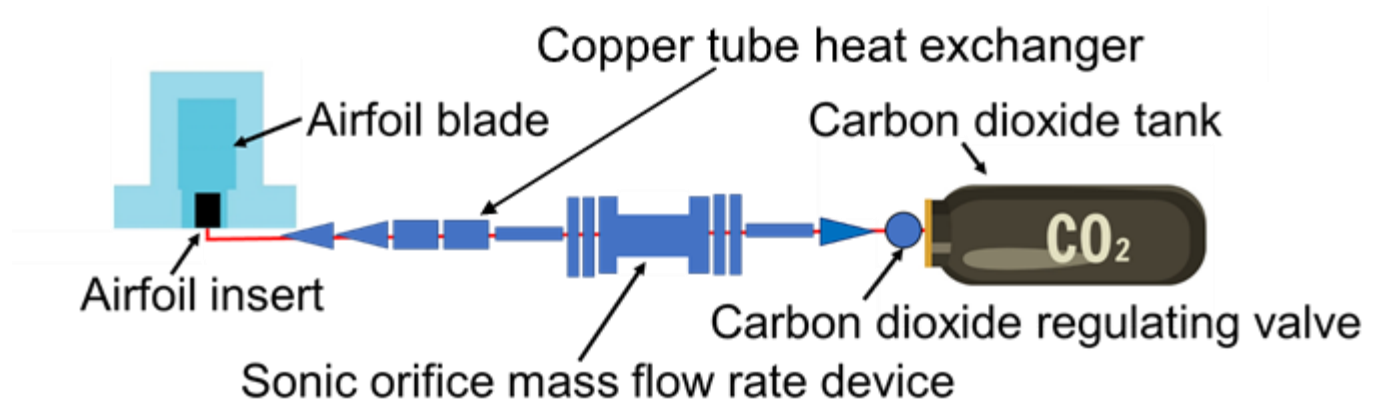


Figure 14. System employed to supply cooled carbon dioxide film cooling air to the instrumented blade.

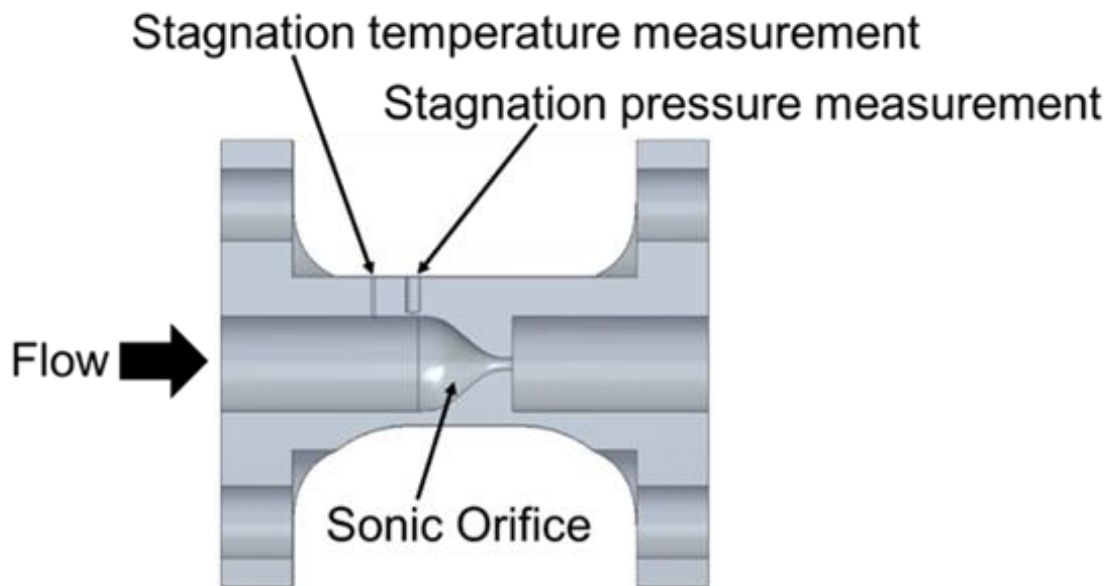


Figure 15. Cross-section view of sonic orifice device.



Details regarding the instrumented central turbine blade are given in Figures 16, 17, and 18. Evident in Figure 16 are the squealer rim and 3 mm deep squealer recess. Figures 17, 20, 21 show the film cooling blade, which utilizes five pressure side film cooling holes. The diameter of each film cooling hole is 0.95 mm. Note that each of these holes are located within a circumferential/axial plane, and is angled  $45^\circ$  relative to this plane. An inclination angle of  $40^\circ$  is employed for each hole, relative to a plane which is tangent to the local blade surface at the hole exit location (Figure 21). A cut-away view of the plenum within the instrumented airfoil, which is used to supply film cooling flow, is shown in Figure 18. Included within this figure are the carbon dioxide supply connection location, pressure tap locations, shelves for mounting thermocouples, and the entrances of the pressure side film cooling holes. The locations of tip surface thermocouples, used for *in situ* calibration of infrared camera images, are shown in Figure 19. A total of 11 specially-calibrated, Omega 5TC-TT-T-40-72 fine-wire copper-constantan (Type T) thermocouples are employed for this purpose, where each is installed at a location which is 0.41 mm below the blade tip surface. Figure 20 shows a transparent view of the film cooling airfoil, depicting a more detailed view of the film cooling passages, thermocouple passages, plenum, and plenum pressure taps. Figure 21 shows a transparent view of the film cooling turbine blade equipped with film cooling passages, thermocouple passages, plenum, and plenum pressure taps.

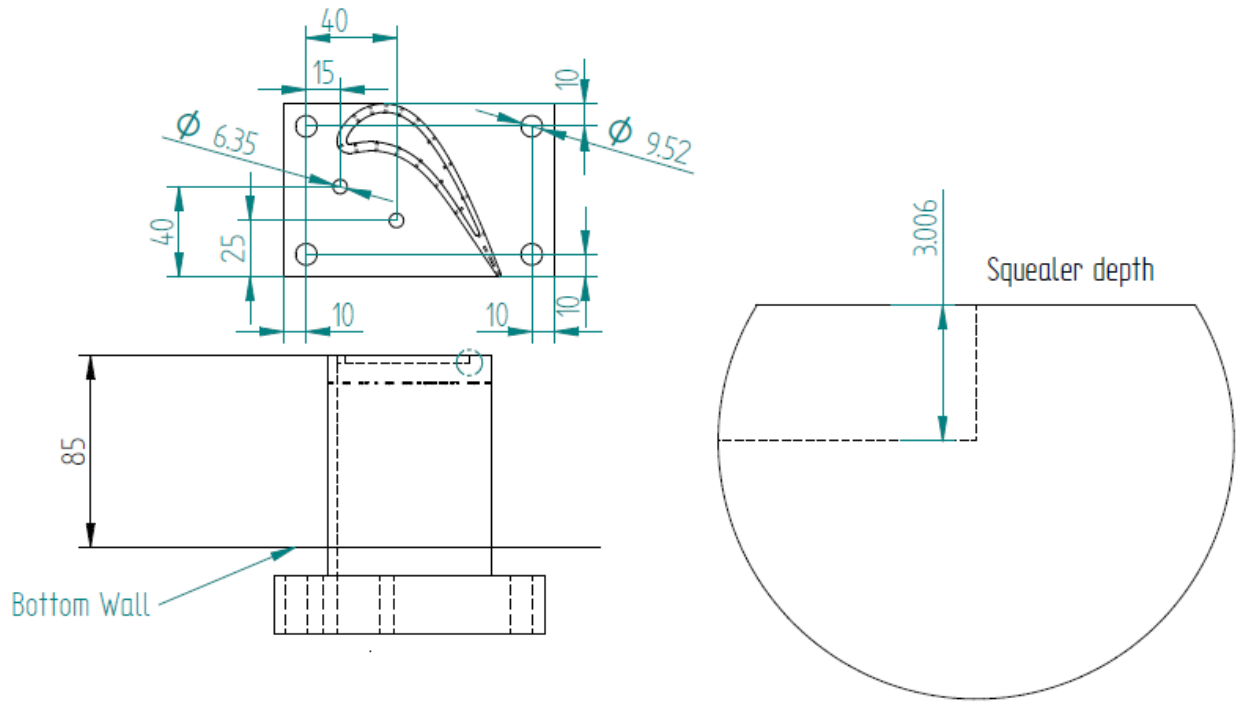


Figure 16. Mounting hole arrangement, Blade span, and squealer recess depth as shown on the 90% span pressure measurement turbine blade. These dimensions are the same for every blade presented in this experiment. Dimensions are in mm.

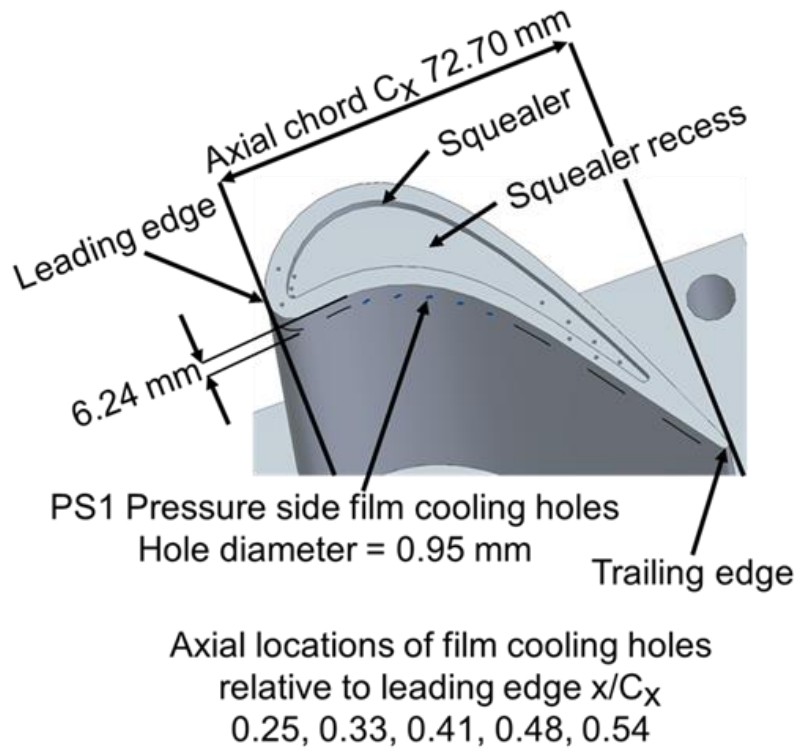


Figure 17. Instrumented central film cooled turbine blade.

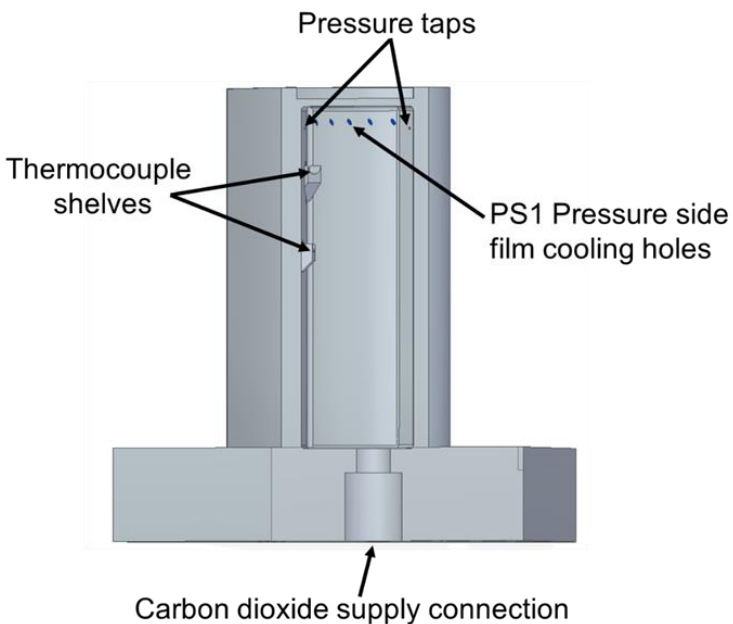


Figure 18. Cut-away view of the plenum within the instrumented airfoil, used to supply film cooling flow.

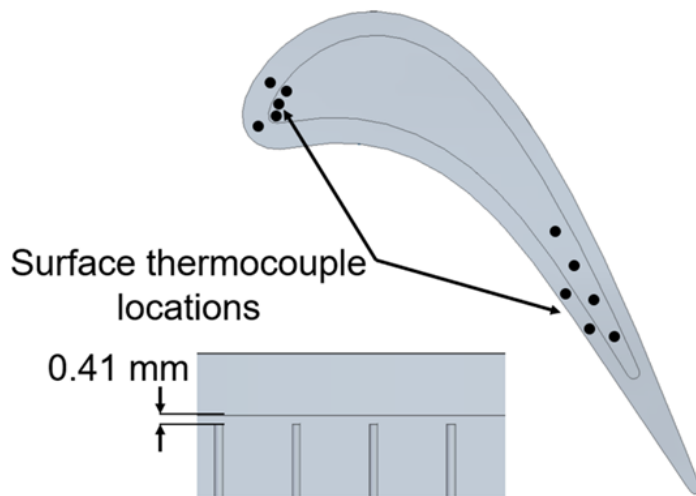


Figure 19. Locations of tip surface thermocouples, used for *in situ* calibration of infrared camera images.

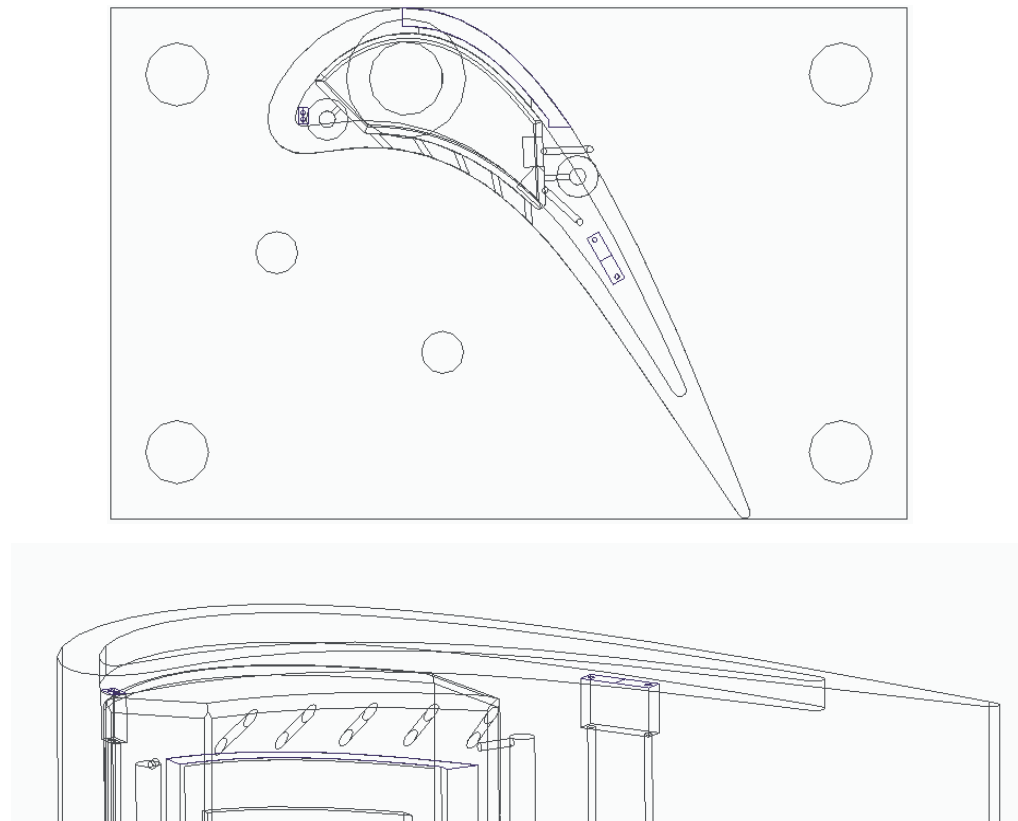


Figure 20. Transparent view of the film cooling turbine blade equipped with film cooling passages, thermocouple passages, plenum, and plenum pressure taps.

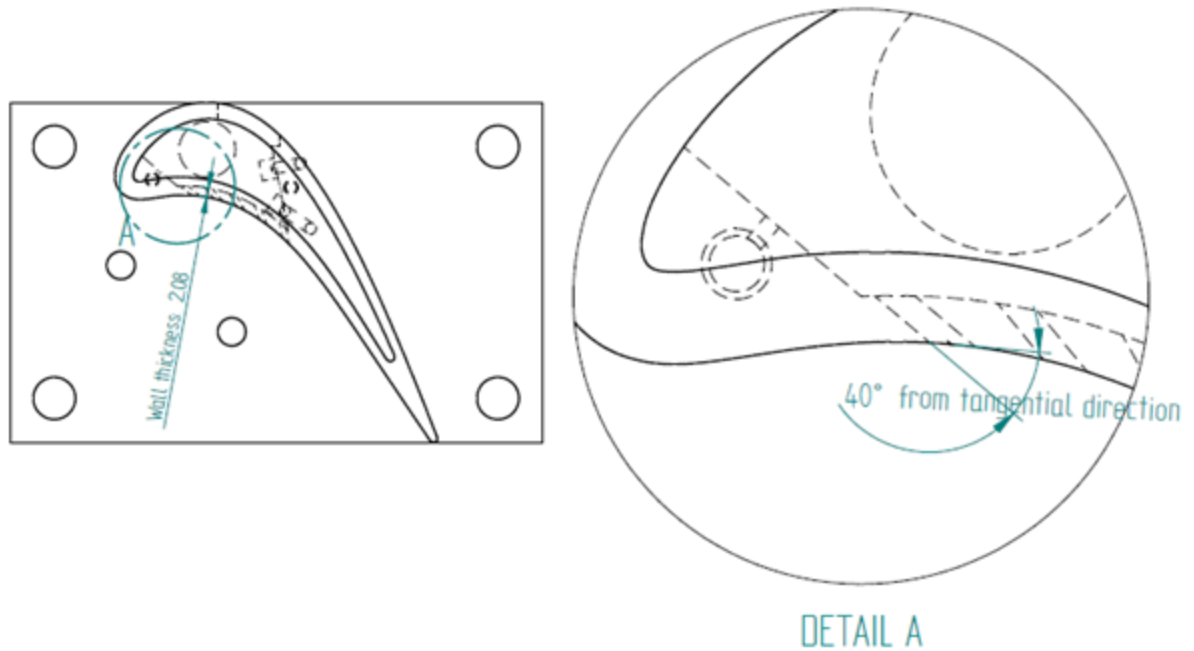


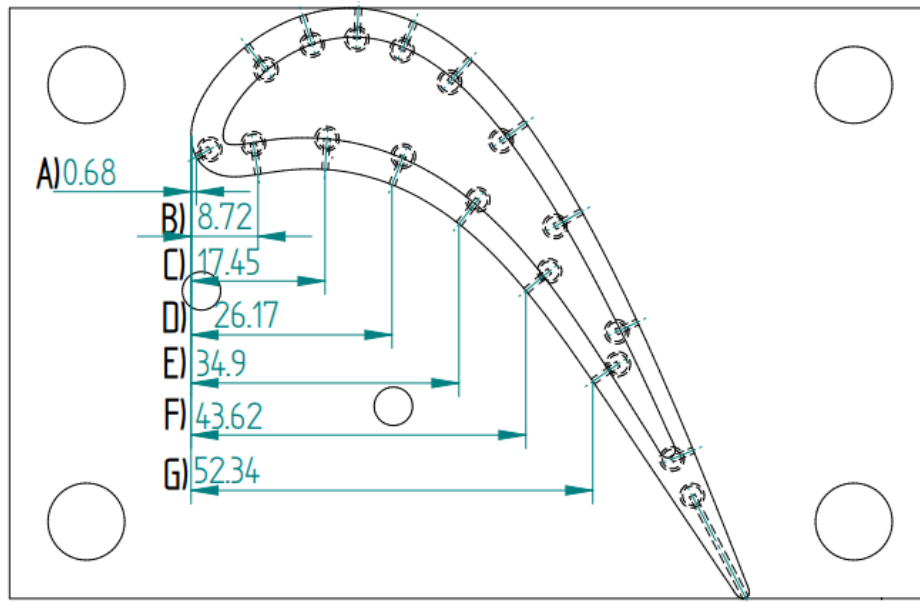
Figure 21. Film cooling hole orientation and wall thickness. Dimensions are in mm.

## 2.5 Pressure Measurement Techniques

The transonic turbine blade cascade utilizes a Kiel probe to measure the stagnation pressure at the inlet of the cascade. Static pressure is measured using 0.80 mm diameter pressure taps located on the bottom wall of the inlet, on the top wall downstream of the turbine blades, within the squealer recess region, and around the circumference of the turbine blades at 50 percent and 90 percent span locations. The Kiel probe and every pressure tap is connected to its own Honeywell FP2000 pressure transducer (part numbers: 023-0032-00 and 060-C54985172080). Each pressure transducer is wired to a National Instruments terminal block (NI 9923), which transmits the different analog signals into a National Instruments Voltage Input Module (NI 9209). The Voltage Input Module is installed within a National Instruments CompactDAQ USB Chassis (NI cDAQ-9174). The end result is a signal that is recorded using LabView 2019 Full Development version 19.0f2, saved to Microsoft Excel 2013 spreadsheet, and processed on a Dell desktop computer running Windows 7 Professional 64-bit (6.1, Build 7601).

All pressure transducers are calibrated using a dead weight tester provided by NASA MSFC. A dead weight tester consists of precisely calibrated weights, a piston, and piping with a working fluid (air, oil, or water) connected to the pressure measurement device being calibrated. Note that if multiple transducers are being calibrated, a manifold can be used to calibrate all of them at the same time. From the mass of the weights and the area of the cylinder, the correct pressure reading can be calculated. This process of adding weights and recording the output voltage is repeated incrementally for the entire advertised range of the transducer. Pressure is plotted as a function of voltage and a linear curve fit equation can be attained. This equation can then be applied to experimental data to accurately calculate stagnation and total pressure.

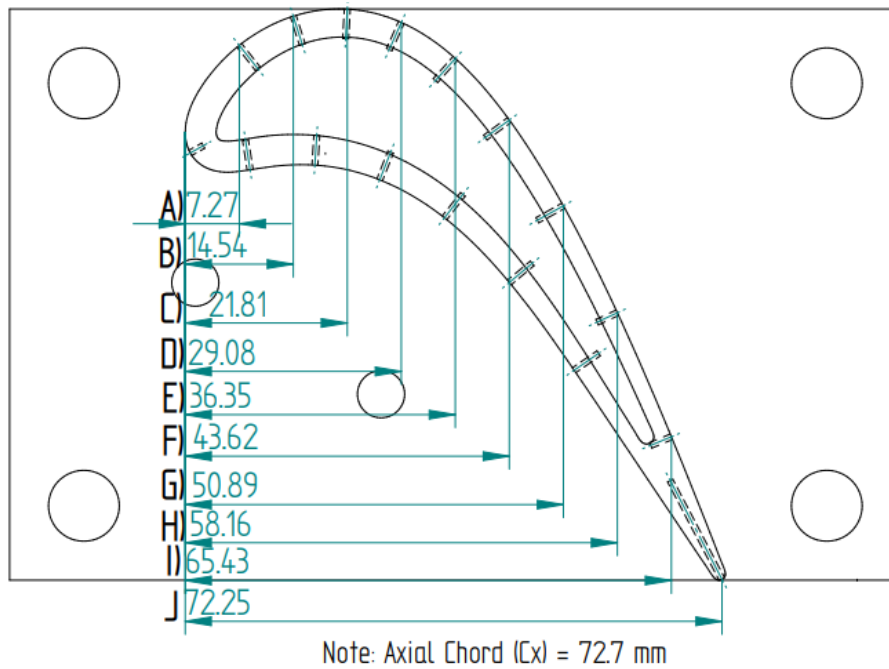
The blade employed to measure the pressure distribution is shown in Figures 22, 23, and 24. The blade in Figures 22 and 23 contain 17 surface static pressure taps which are positioned to measure circumferential pressure distribution for a given blade span location. The blade in Figure 28 contains 8 static pressure taps positioned within the squealer recess. Each pressure tap has a diameter of 0.80 mm and are oriented normal to the surface. The hole connected to each tap is initially 0.80 mm in diameter, then enlarges to 2.50 mm within the blade material. This hole further enlarges to 3.18 mm at the base of the blade to accommodate a 25.4 mm long piece of smooth-bore seamless 304 stainless steel tubing (0.069" ID, 1/8" OD). This steel tubing is used as the connection to the clear polyurethane tubing (1/8" ID, 1/4" OD) attached to the barbed hose fitting (McMaster-Carr part#: 5346k62) on a pressure transducer. A SharkBite push-to-connect coupling fitting is used to connect the polyurethane tubing on the base of the blade to the polyurethane tubing on the pressure transducer. With this arrangement, the isentropic Mach number distribution is determined for the circumference of the blade and for the tip of the central blade within the cascade.



Pressure Tap Locations	
Location	% Cx
A	0.9
B	12
C	24
D	36
E	48
F	60
G	72

Note: Axial Chord (Cx) = 72.7 mm

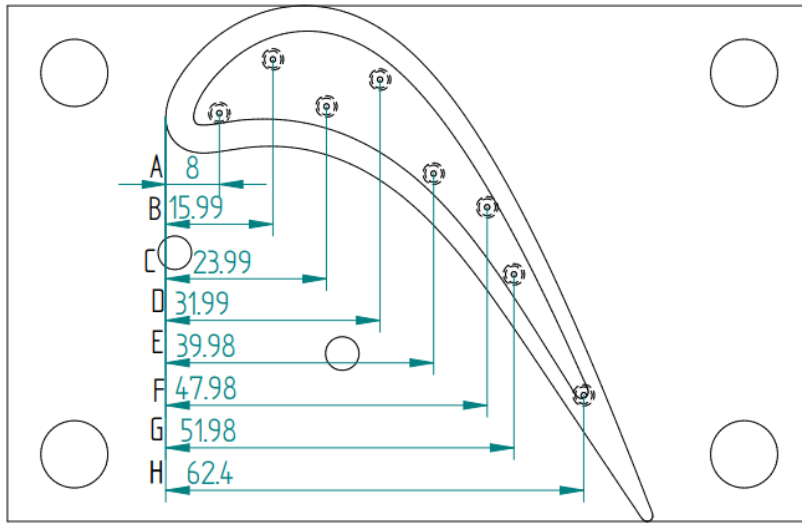
Figure 22. Pressure side pressure tap locations. Dimensions are in mm.



Pressure Tap Locations	
Location	% Cx
A	10
B	20
C	30
D	40
E	50
F	60
G	70
H	80
I	90
J	99.4

Note: Axial Chord (Cx) = 72.7 mm

Figure 23. Suction side pressure tap locations. Dimensions are in mm.



Pressure Tap Locations	
Location	% Cx
A	11
B	22
C	33
D	44
E	55
F	66
G	71.5
H	85.8

Note: Axial Chord (Cx) = 72.7 mm

Figure 24. Blade tip pressure tap locations. Dimensions are in mm.

The end wall in Figure 25 also uses 0.80 mm diameter static pressure taps normal to the flow surface. The pressure taps are located in two rows downstream of the turbine blades in the circumferential/radial plane. One row is 0.5 axial chord lengths downstream, and the other is 1.0 axial chord lengths downstream. The hole connected to each tap is initially 0.80 mm in diameter, then enlarges to 6.35 mm to accommodate a 1/4" outer diameter barbed tube fitting (McMaster-Carr part#: 1901k89). This fitting is used to connect the pressure tap to the clear polyurethane tubing (1/4" ID, 3/8" OD). The polyurethane tubing then connects to the barbed hose fitting on the pressure transducer.



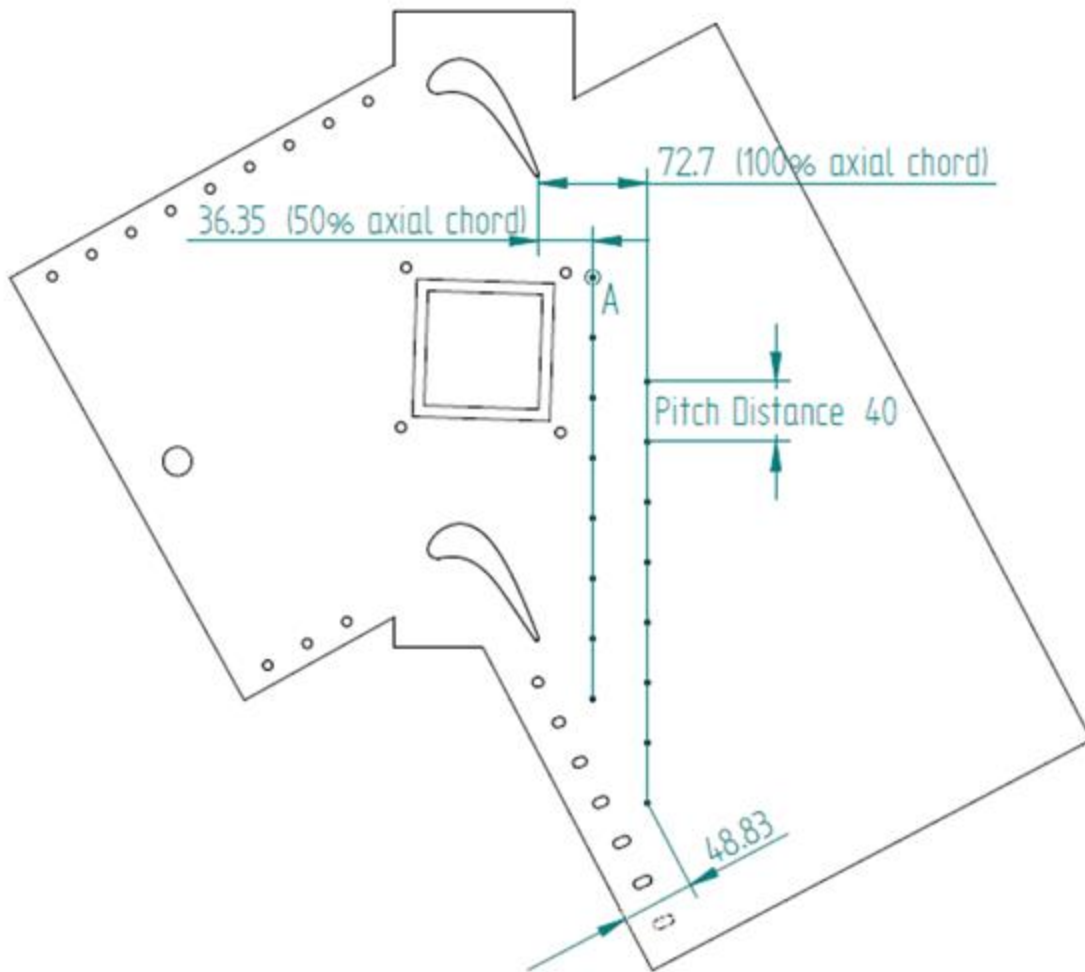


Figure 25. End wall static pressure tap arrangement. Dimensions are in mm.

## 2.6 Temperature Measurement Techniques

Omega 5TC-TT-T-40-72 fine-wire copper-constantan (Type T) thermocouples are used to measure the temperatures on the blade tip for infrared calibration, within the sonic orifice, and within the blade plenum. Omega 5TC-TT-T-20-36 20-gauge copper-constantan (Type T) thermocouples are used to measure the temperature at the cascade inlet. Thermocouple signals are acquired at a rate of 30 Hz using a National Instruments NI 9213 thermocouple input card installed in a National Instruments NI cDAQ-9188 chassis connected to the data acquisition computer. The signals are recorded using LabView 2019 Full Development version 19.0f2, saved onto a Microsoft Excel 2013 spreadsheet, and processed on a Dell desktop computer running Windows 7 Professional 64-bit (6.1, Build 7601). The thermocouples are calibrated by submerging them in a water bath kept at constant temperature using an Omega HCTB-3030 thermoregulator. The output voltage of the thermocouples are recorded at several different water temperatures and compared to a Fluke 1523 reference thermometer. From this data, a linear calibration equation is acquired and is applied to all subsequent thermocouple voltages. The maximum frequency response of each thermocouple junction is estimated to be approximately  $1.2 \times 10^{-4}$  to  $1.6 \times 10^{-4}$  seconds, which is approximately equivalent to 6 to 8 kHz. These thermocouples are installed along the surface on which measurements are made, which is adjacent to the associated tip gap flow.

## 2.7 Heat Transfer Measurement Techniques

A time-varying technique is employed to determine adiabatic surface temperature variations, adiabatic film cooling effectiveness distributions, and surface heat transfer coefficients. Figure 26 illustrates the arrangement used to measure spatially-resolved variations along the tip of a two-dimensional turbine blade airfoil. The key measurement component is a FLIR Systems Inc. ThermoVision® T650sc Infrared Camera (S/N 22700776), which is mounted external to the cascade top wall. This device senses temperature variations, as it views a blade tip surface through a zinc-selenide window, from a location which is external to cascade components. Figure 12 shows the FLIR camera mounted on top of the cascade.

Associated cascade blade components are comprised of Somos Watershed XC 11122 plastic, and are manufactured by Protolabs Inc. of Maple Plain, Minnesota, USA. This material is selected for cascade testing for several reasons. First, thermal conductivity is relatively low with a

value of 0.18 W/mK. Second, associated components are manufactured without shrinkage or distortion, and with high dimensional accuracy and low manufacturing tolerances, which means that scaled geometric similarity relative to actual engine hardware is maintained. Third, the strength of the material allows it to be employed for testing of airfoil components subject to large pressure differences, including intricate film cooling supply passages and complex film cooling hole array arrangements.

The present FLIR Infrared Camera functions at infrared wavelengths from 7.5  $\mu\text{m}$  to 13.0  $\mu\text{m}$ , as it detects infrared radiation emitted by the instrumented blade tip surface which is the subject of the measurements. Note that each instantaneous digital infrared image is calibrated as it is captured by the camera. A calibration relationship is developed for this purpose to provide a relationship between local surface temperature values (as measured by individual thermocouples) and different grayscale values which are associated with different magnitudes of surface infrared radiation. By employing FLIR ResearchIR software, a digital image acquisition rate of 30 Hz is employed as data are obtained using the infrared camera. Each individual infrared image then shows the instantaneous, spatial variation of surface temperature at one time.

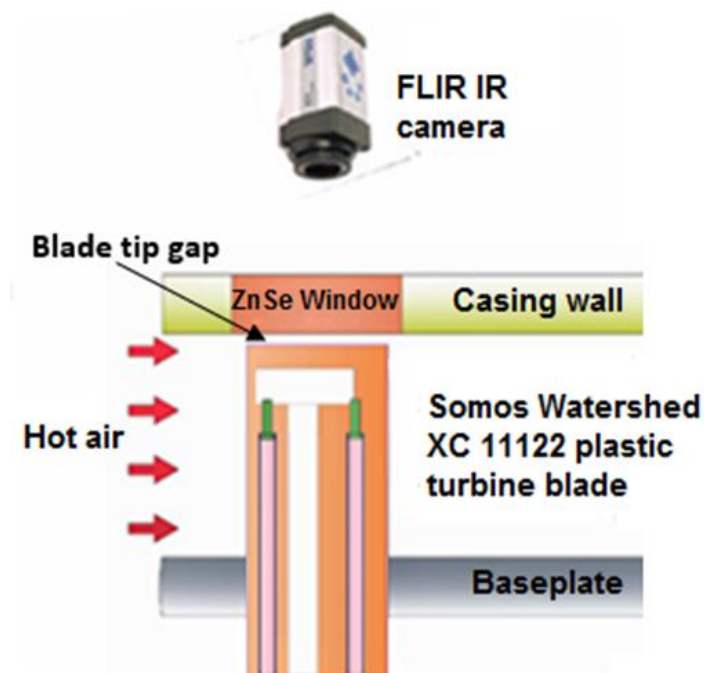


Figure 26. Schematic diagram of laboratory arrangement employed for transient, spatially-resolved surface heat transfer measurements for the present turbine blade tip configuration.

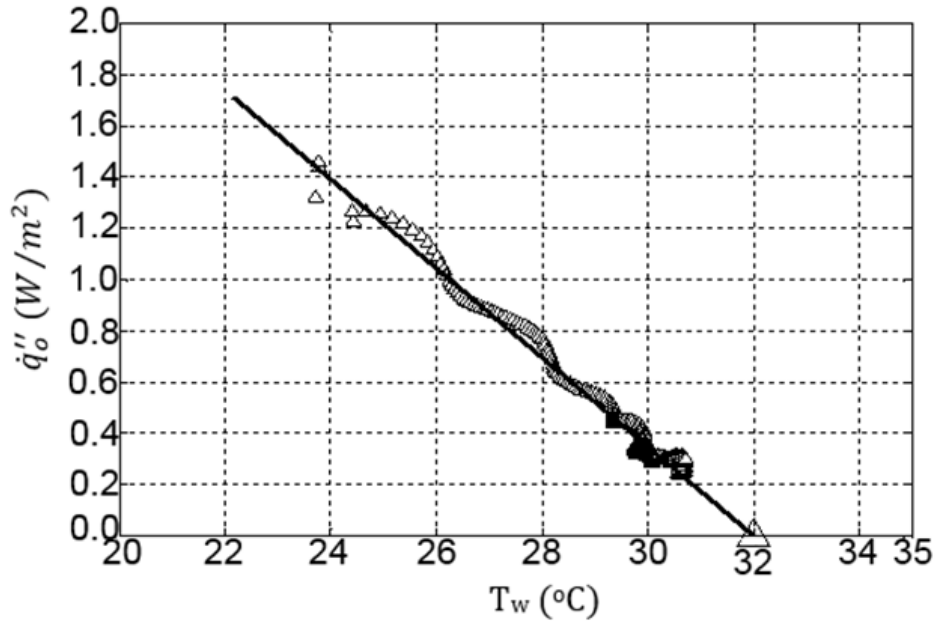


Figure 27. Example of variation of local heat flux with surface temperature for one test surface location during a typical transient test seen in Zhang et al. (2011)

The present study considers surface heat transfer characteristic for a range of film cooling flow conditions, film cooling geometry configurations, and blade tip arrangements. These data are produced using the impulse response method described by Oldfield (2008), which is “a computationally efficient method to reconstruct heat flux from discrete temperature samples taken at some sampling frequency.” This analysis approach relates surface heat flux changes to changes of surface temperature with time. Conditions imposed on this approach include semi-infinite solid material, and conduction heat transfer in only one direction. Note that heat transfer coefficient and film cooling effectiveness uncertainty estimates include variations which are not one-dimensional. This approach is needed since local, three-dimensional heat transfer variations are sometimes present near and adjacent to individual hole passages which are utilized for film cooling. Within the present investigation, overall temperature differences between blade surfaces and the mainstream air will range from 8 to 30 degrees Celcius. Overall temperature differences between

the film cooling air and the mainstream air, as needed to achieve appropriate flow conditions, range from 8 to 20 degrees Celcius.

For each surface location, heat flux changes with surface temperature are determined during the time interval after the time when the main flow temperature increases in a transient fashion, using procedures described earlier. Figure 27 provides an example of the variation of local heat flux with surface temperature, for one test surface location, during a typical transient test. From the resulting data, the magnitude of the slope is equal to the heat transfer coefficient and adiabatic wall temperature is extrapolated for the condition associated with zero surface heat flux. Measured spatially-resolved distributions of adiabatic surface temperature are then used to determine local values of the spatially-resolved surface effectiveness, using equations (6) and (7).

$$\eta_{AD-corrected} = (T_{AW-NFC} - T_{AW-FC}) / (T_{0-inlet} - T_{0-c}) \quad (6)$$

$$\eta_{AD-corrected-new} = (T_{AW-NFC} - T_{AW-FC}) / (T_{AW-NFC} - T_{0-c}) \quad (7)$$

Equation (6) gives local film cooling performance, normalized by two global parameters  $T_{0-inlet}$  and  $T_{0-c}$ . Equation (7) gives local film cooling performance, normalized by one global parameter  $T_{0-c}$ . The iso-energetic heat transfer coefficient and coefficient ratio are given by

$$\dot{q}_0'' = h(T_{AW-FC} - T_W) \quad (8)$$

$$HTC \text{ Ratio} = h/h_{NFC} \quad (9)$$

With this approach, spatially resolved distributions of surface adiabatic film cooling effectiveness and surface iso-energetic heat transfer coefficients are provided.

## 2.8 Experimental Uncertainty Magnitudes

Uncertainty estimates are based on 95 percent confidence level, and determined using procedures described by Kline and McClintock (1953) and by Moffat (1988). Uncertainty of adiabatic film cooling effectiveness is  $\pm 0.007$  for values less than or equal to 0.12. Uncertainty of adiabatic film

cooling effectiveness is  $\pm 6.0$  percent for values greater than 0.12. Uncertainty of iso-energetic heat transfer coefficient is  $\pm 8.5$  percent.

## **CHAPTER 3**

### **EXPERIMENTAL RESULTS**

Presented in this chapter are experimental test conditions, blade, end wall, and squealer recess Mach number and pressure ratio distributions, heat transfer coefficient distributions, heat transfer coefficient ratio distributions, and different types film cooling effectiveness data.

#### **3.1 Experimental Test Conditions**

Figure 28 shows pressure variations with time at typical different locations in the cascade and along the blade, during a typical blow down experiment. From these pressure variations, different quantities are determined such as pressure ratios and Mach numbers as they vary with time at different locations through the cascade test section during a typical experiment. All of these data are obtained for a tip gap of 1.40 mm. Data are given for the upstream static pressure on the end wall of the cascade, the downstream static pressure on the end wall of the cascade, the exhaust stagnation pressure, the inlet stagnation pressure, and static pressures at different locations along the airfoil. Pressures denoted 2 through 17 are different locations along the airfoil, including near the leading edge and trailing edge. These pressure tap locations on the blade surface are given in Figures 22 and 23. The locations denoted B through G on Figure 22 correspond to pressures 2 through 7 on Figure 28. The locations denoted A through J on Figure 23 correspond to pressure 8 through 17 on Figure 28.

Evident in the figure is a dramatic increase of all pressure levels starting at a time of 15 seconds, with a very important rise in pressures from 15 seconds to 18 seconds. From 18 seconds to 22 seconds, there is a decrease and an increase in the local pressure values as they vary with time. Pressures are then relatively steady for a 7 second period, from 22 to 29 seconds. After this period of steady test conditions, all pressures decrease with time as the test blow down is ending. Different pressure levels are evident for these different pressure transducers as a result of different flow conditions around the airfoil, at the inlet, and exit of the cascade facility. In general, all pressures are roughly invariant over the steady testing time extending from 22 to 29 seconds. This

illustrates that steady test conditions are readily achieved with the present test arrangement and facility settings.

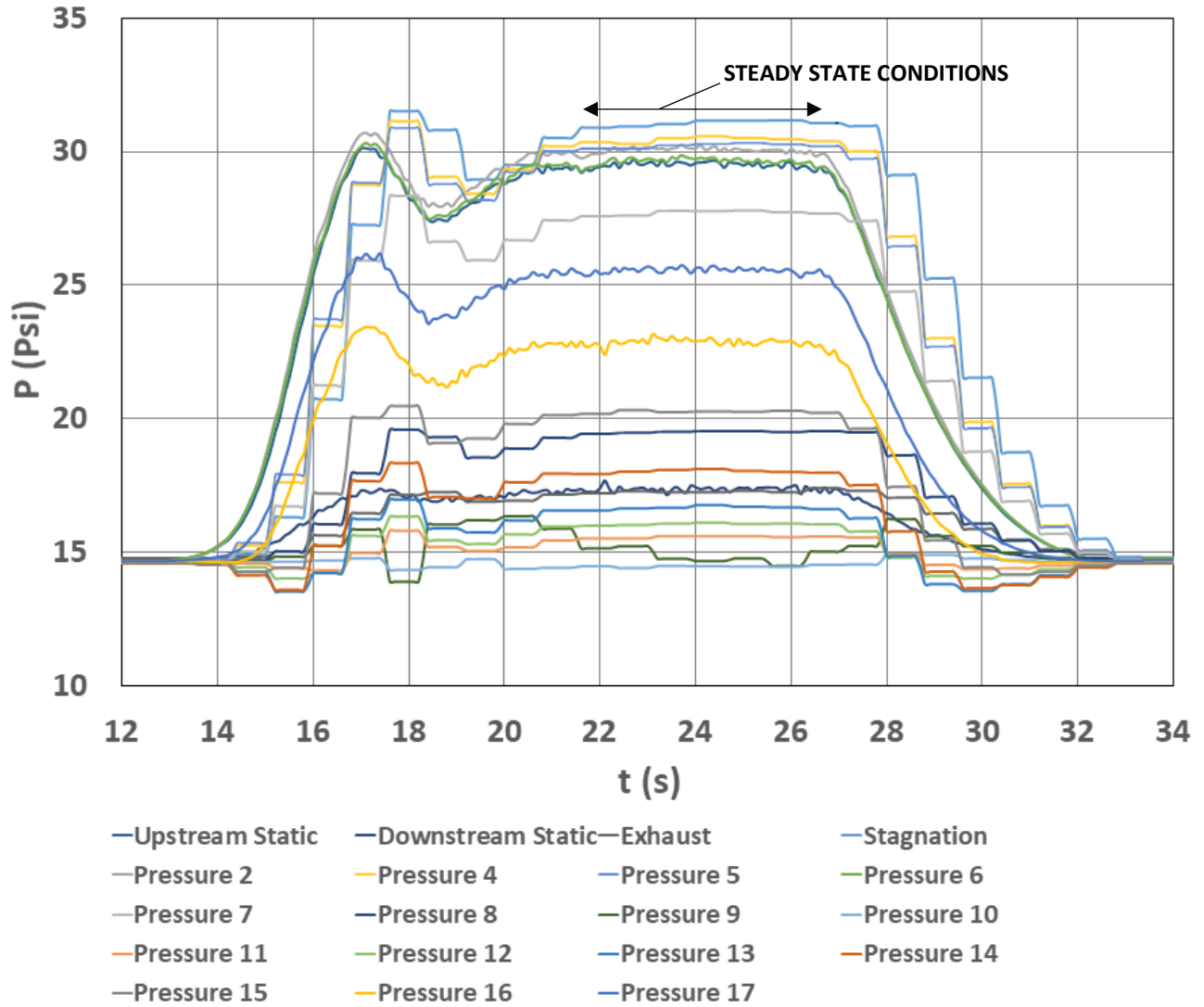


Figure 28. Pressure variations with time during a typical blow down experiment.

### 3.2 Mach Number and Pressure Ratio Distributions

Discussed in this section are the Mach number and static pressure ratio distributions around the blade profile, Mach number and static pressure ratio distributions within the squealer recess, and the static pressure ratio distributions for the end wall at 0.5 and 1.0 axial chord lengths downstream of trailing edges of the blades.

Figure 29 shows central blade isentropic Mach number distributions at 50 percent span for the blade suction surface, and for the blade pressure surface. Figure 30 shows central blade isentropic Mach number distributions at 90 percent span for the blade suction surface, and for the blade pressure surface. Note that the line denotes predicted Mach number distributions for the same airfoil. For both the 50 percent and 90 percent span locations, the pressure side of the blade is always subsonic, reaching a maximum value around Mach 0.8 at the trailing edge where it meets the flow from the suction side. Mach numbers for the flow on the suction side for the 50 percent location increase with streamwise development, reaching a maximum value of 1.1 at  $0.8 x/C_x$ . Mach numbers for the flow on the suction side at the 90 percent span location increase with streamwise development, reaching a maximum value of 1.24 at  $0.8 x/C_x$ . The experimental values generally match the numerically predicted values, especially at the upstream part of the airfoil. In all cases for the suction side, acceleration to sonic conditions occurs, followed by supersonic flow.

Figure 31 presents the blade tip static pressure tap locations within the squealer recess. Figure 32 shows the associated blade tip total to static pressure ratio and isentropic Mach number distributions. The Mach number is approximately 0.5 from  $0.11 x/C_x$  to  $0.44 x/C_x$ , followed by a local increase to approximately Mach 1.25 from  $0.55 x/C_x$  to  $0.86 x/C_x$ . Note that isentropic Mach numbers are only approximately representative of flow physics within the tip gap flow because of important variations of total pressure through this flow. Within the squealer recess, acceleration to sonic conditions appears to occur, followed by supersonic flow, which is present immediately downstream.

Figure 33 presents the end wall static pressure tap measurement locations. Figure 34 presents pressure ratio measurements for the row of pressure taps located 0.5 axial chord lengths downstream of the trailing edges of the blades. Figure 35 shows pressure ratio measurements for the row of pressure taps located 1.0 axial chord lengths downstream of the trailing edges of the blades. Data in Figures 34 and 35 are a composite of pressure variation data downstream of the flow passage periods downstream of the cascade. These are then assembled and made periodic relative to the spacing over one passage. As a result with this arrangement, the data in Figures 34 and 35 show approximate periodicity and repeatability, relative to different blade passages.



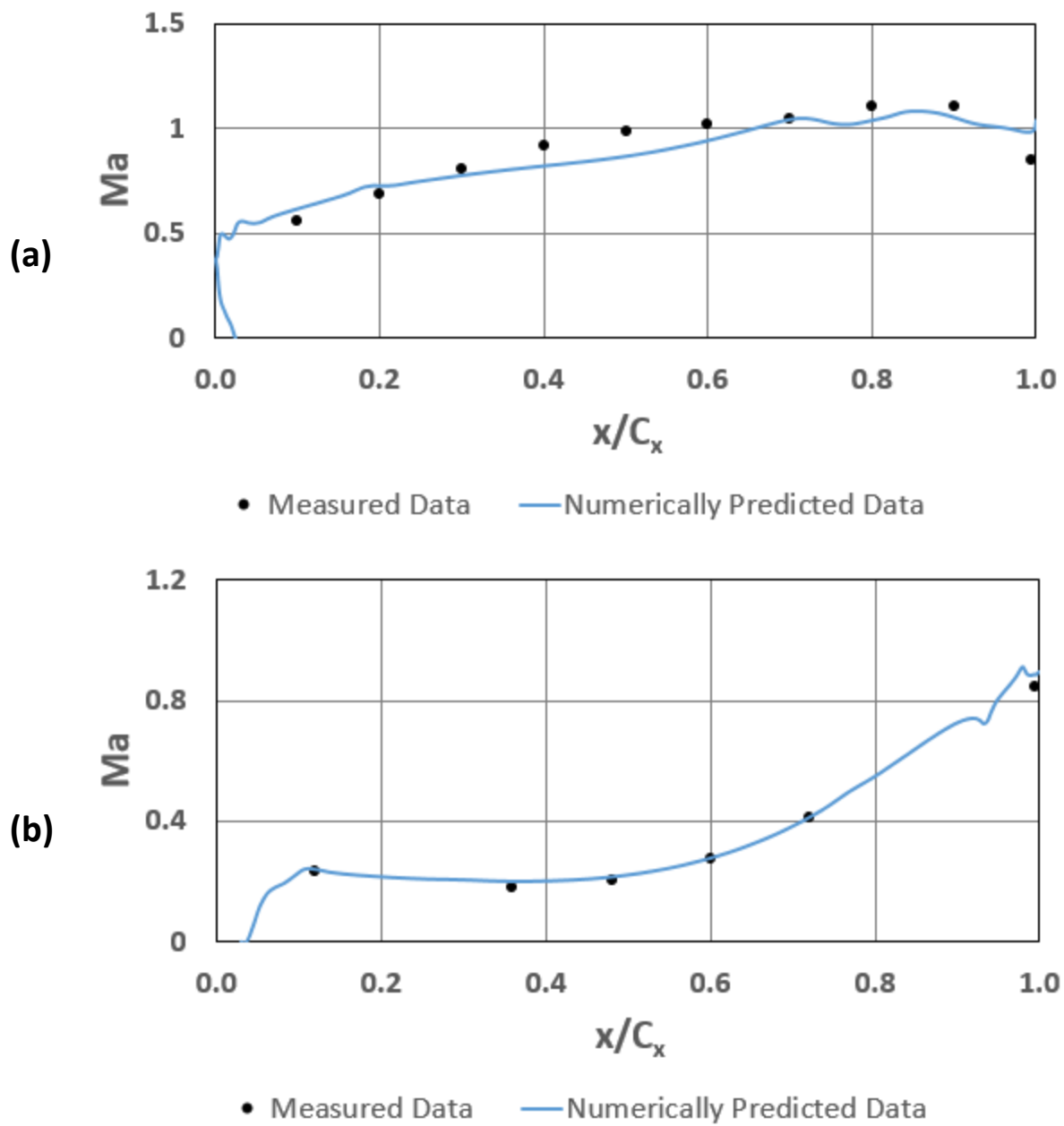


Figure 29. Central blade isentropic Mach number distributions at 50 percent span. (a) Suction surface. (b) Pressure surface.

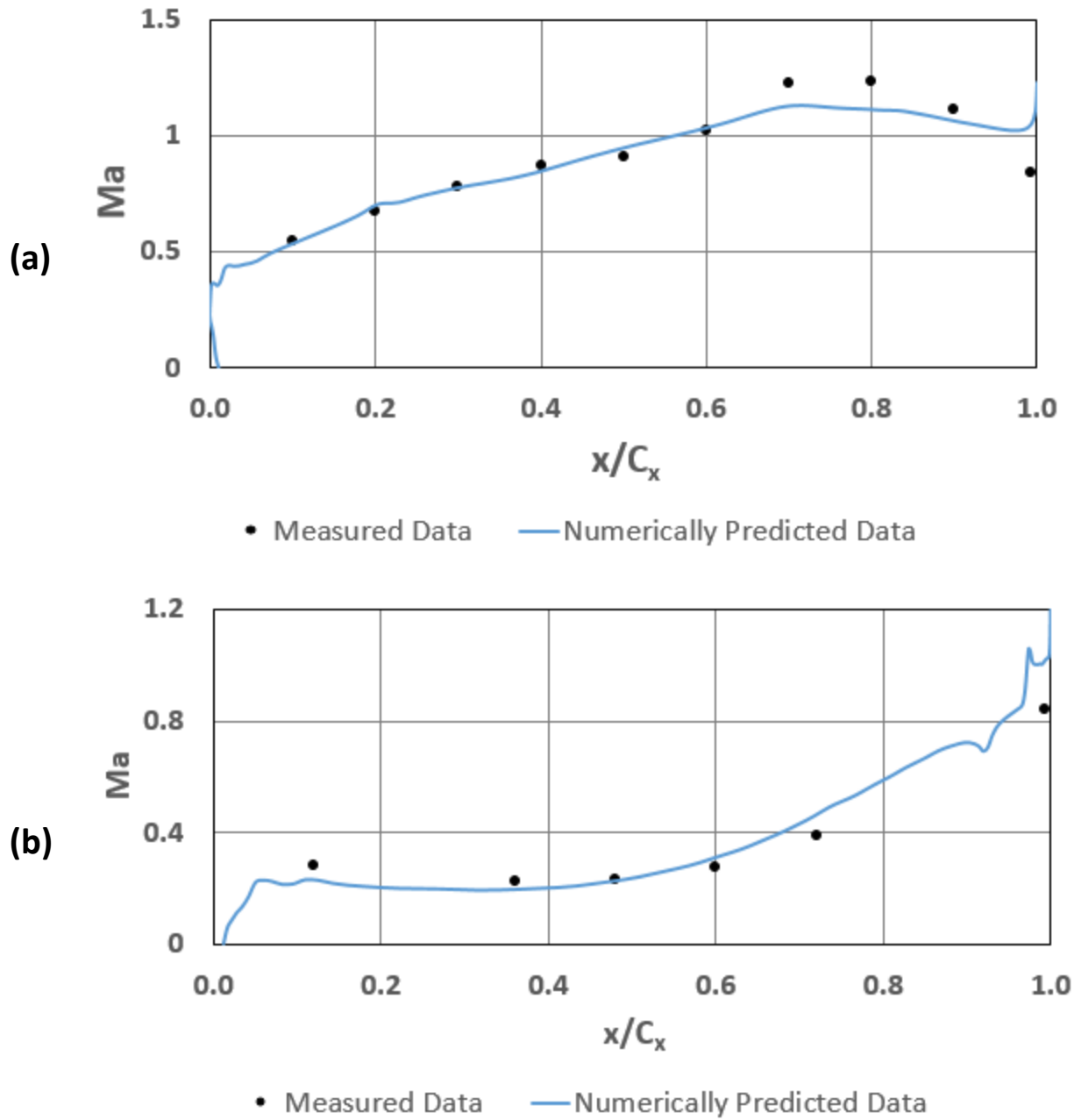
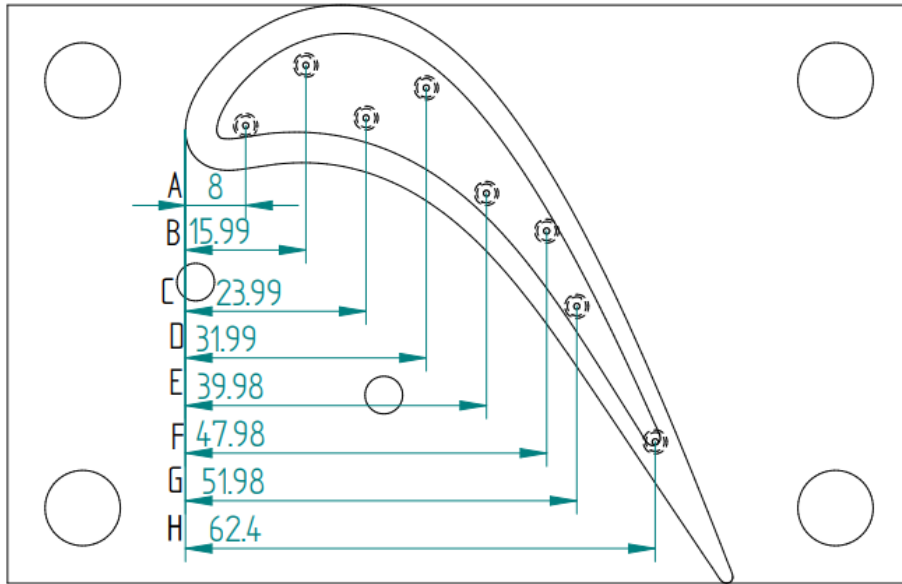


Figure 30. Central blade isentropic Mach number distributions at 90 percent span. (a) Suction surface. (b) Pressure surface.



Pressure Tap Locations	
Location	% $C_x$
A	11
B	22
C	33
D	44
E	55
F	66
G	71.5
H	85.8

Figure 31. Blade tip pressure tap locations. Dimensions are in mm.

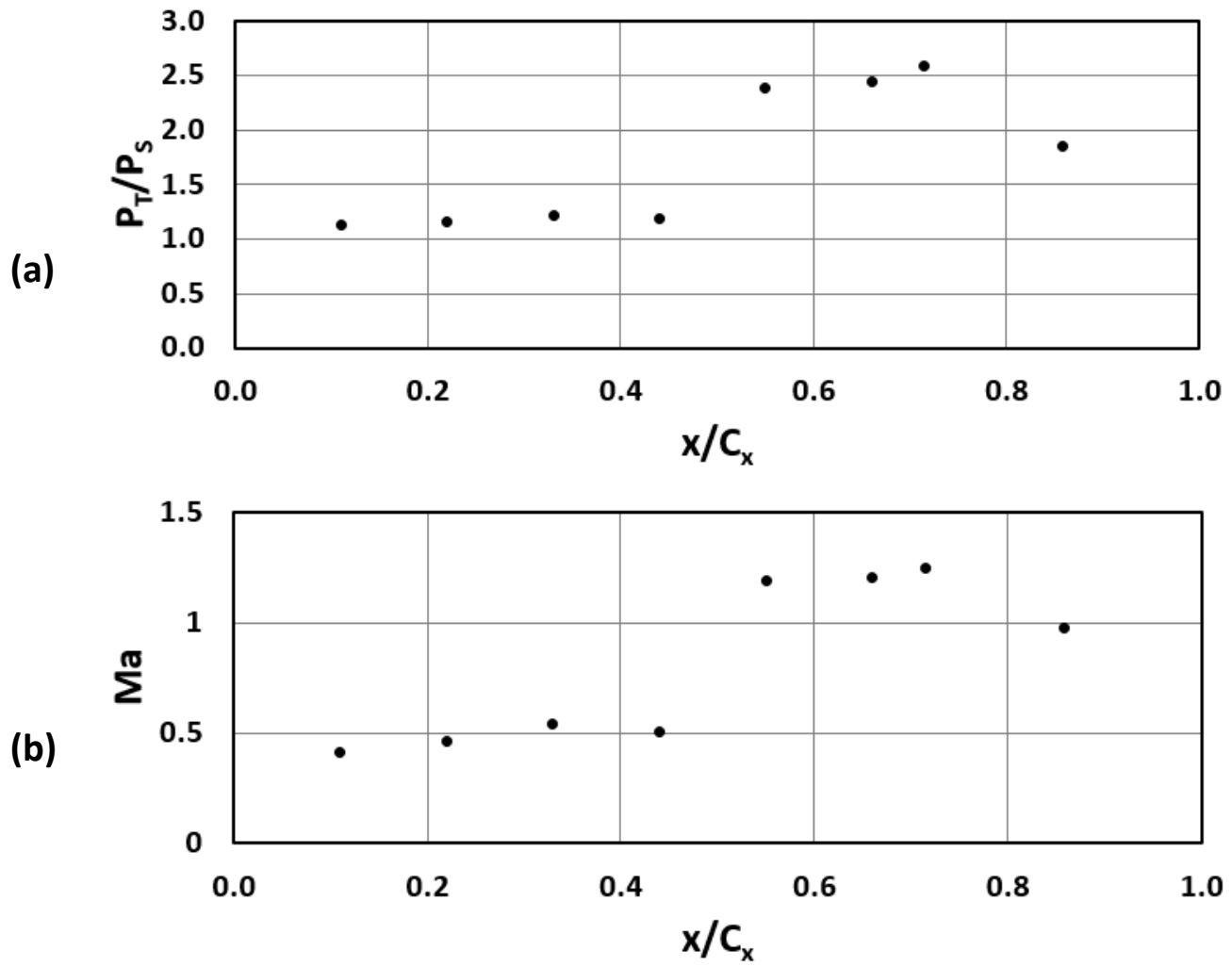


Figure 32. Squealer recess blade measurements. (a) Total to static pressure ratio. (b) Isentropic Mach number.

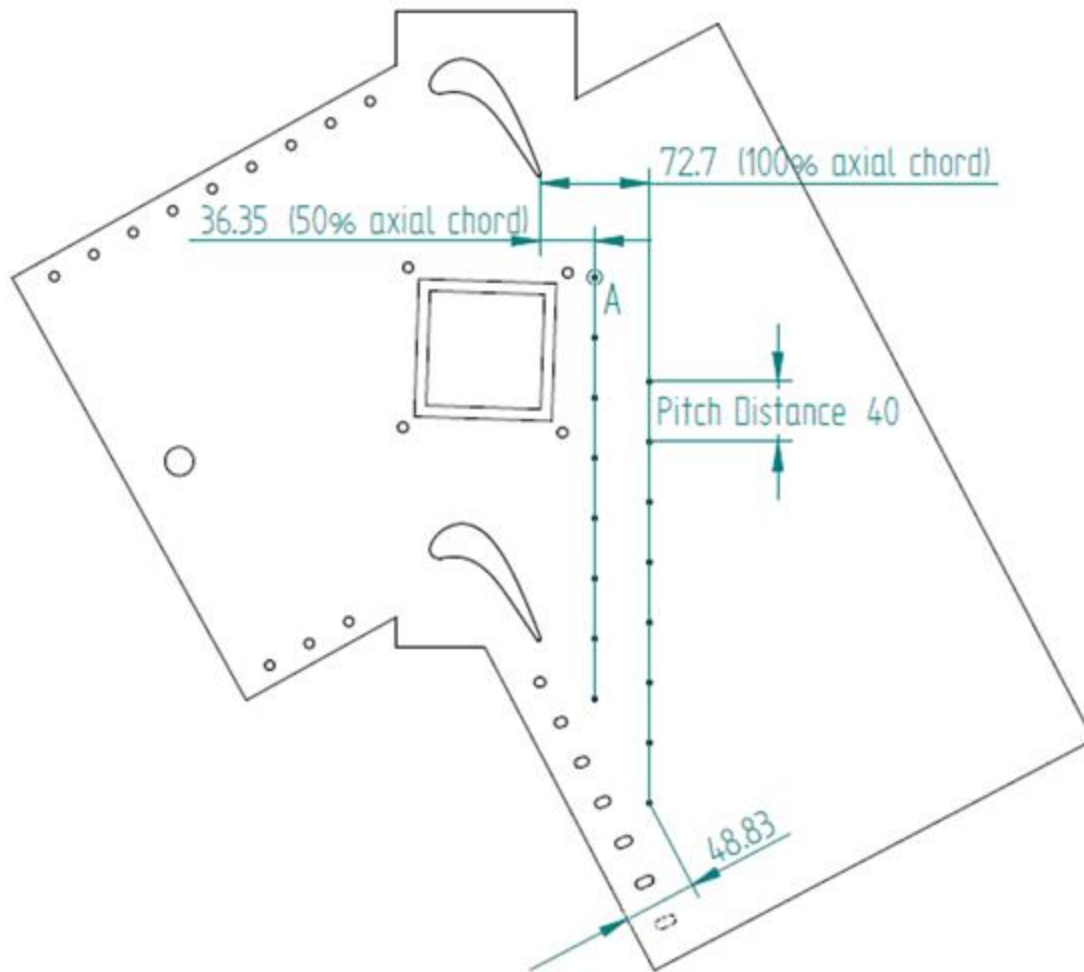


Figure 33. End wall static pressure tap arrangement. Dimensions are in mm.

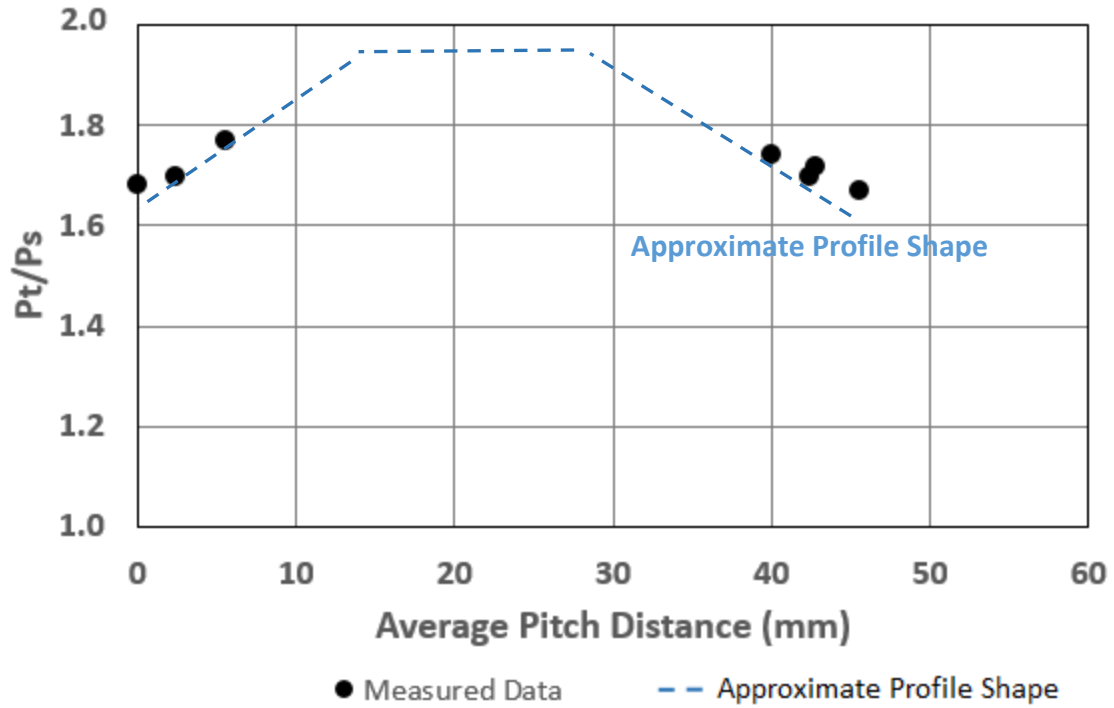


Figure 34. Total to static pressure ratio for 0.5 axial chord lengths downstream of the trailing edges of the blades.

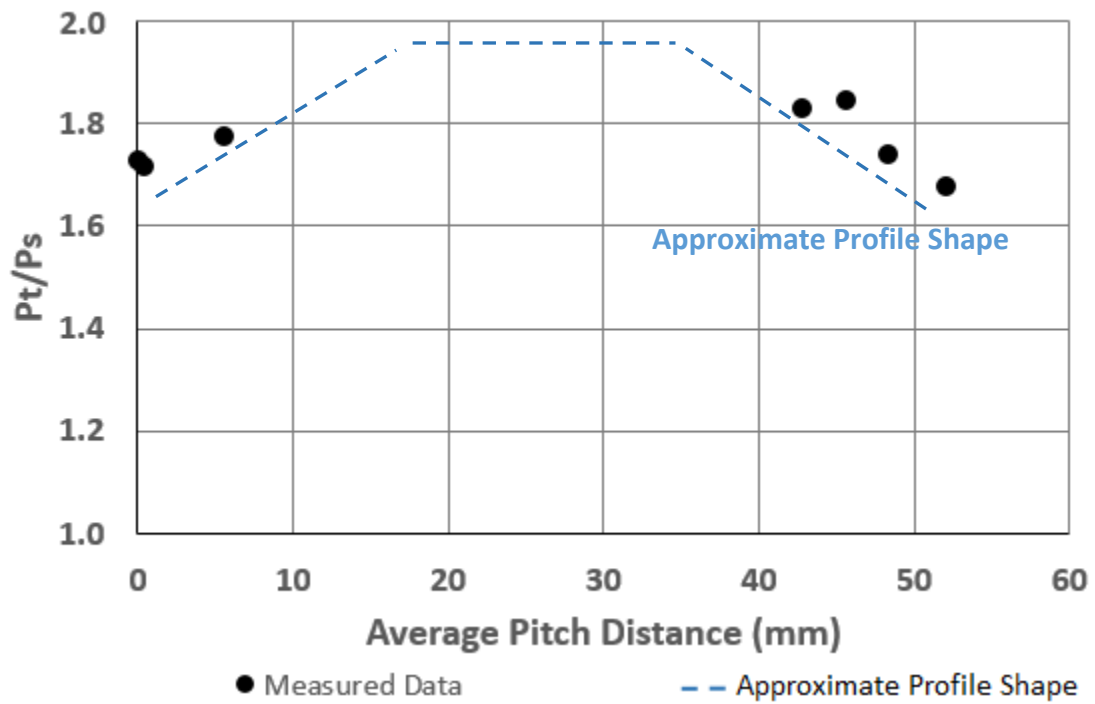


Figure 35. Total to static pressure ratio for 1.0 axial chord length downstream of the trailing edges of the blades.

### 3.3 Blade Film Cooling Geometry

The instrumented turbine blade utilizes five pressure-side film cooling holes, which are designated as the B1 film cooling configuration. Figures 36 through 39 show the details of this arrangement. The diameter of each film cooling hole is 0.95 mm. The length to diameter ratio of each hole is approximately 4.60. Note that each of these holes are located within a circumferential/axial plane, and are angled  $45^\circ$  relative to this plane. An inclination angle of  $40^\circ$  is employed for each hole, relative to a plane which is tangent to the local blade surface at the hole exit location. The hole spacing is 6.18 mm (6.5d), measured as surface arc length. Surface arc length is defined as the distance along the surface between two adjacent holes.

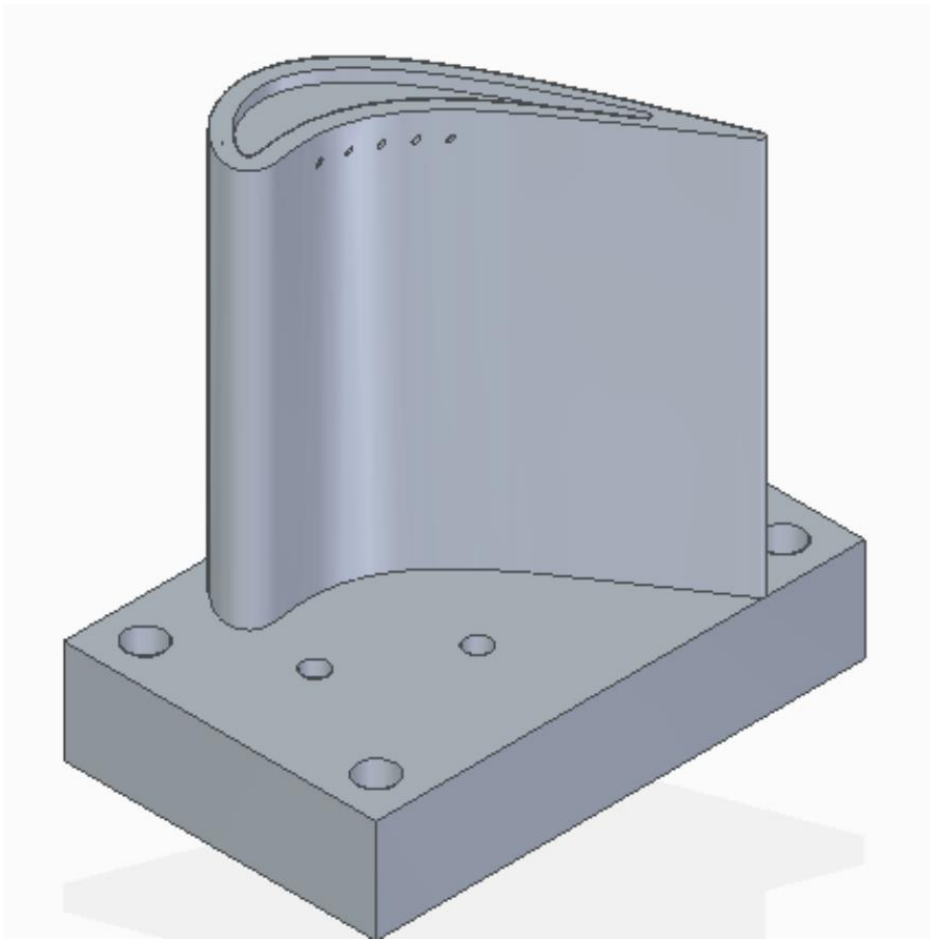


Figure 36. Isometric view of the pressure side film cooled turbine blade model with the B1 film cooling configuration.

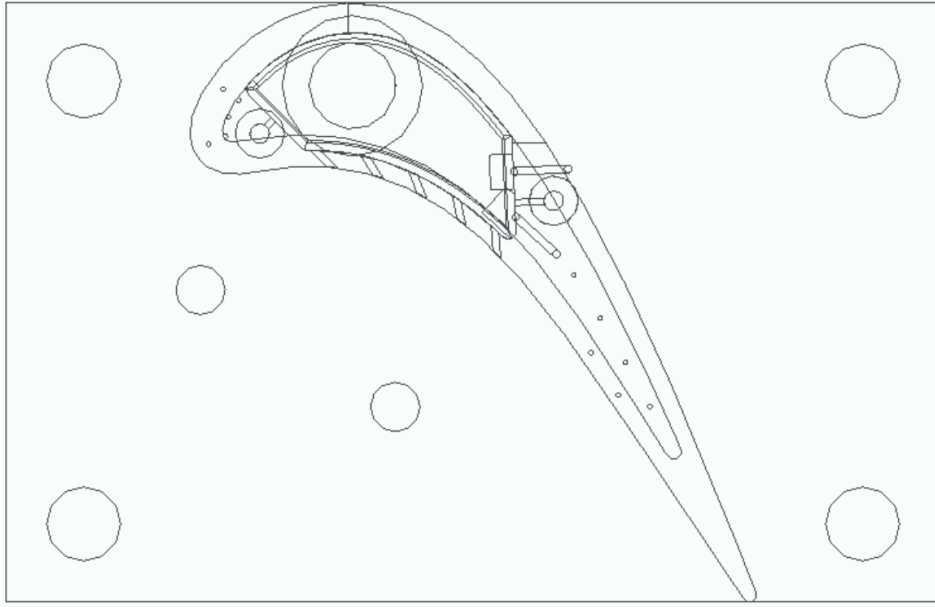


Figure 37. Transparent top view of the pressure side film cooled turbine blade model with the B1 film cooling configuration.

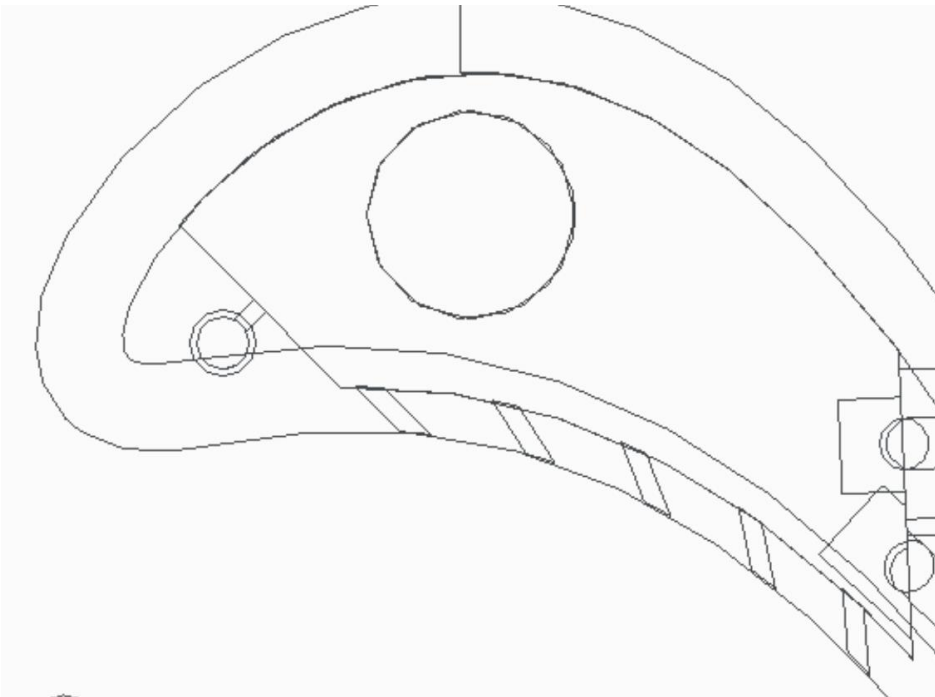


Figure 38. Detailed, transparent top view of the film cooling geometry of the B1 film cooling configuration.



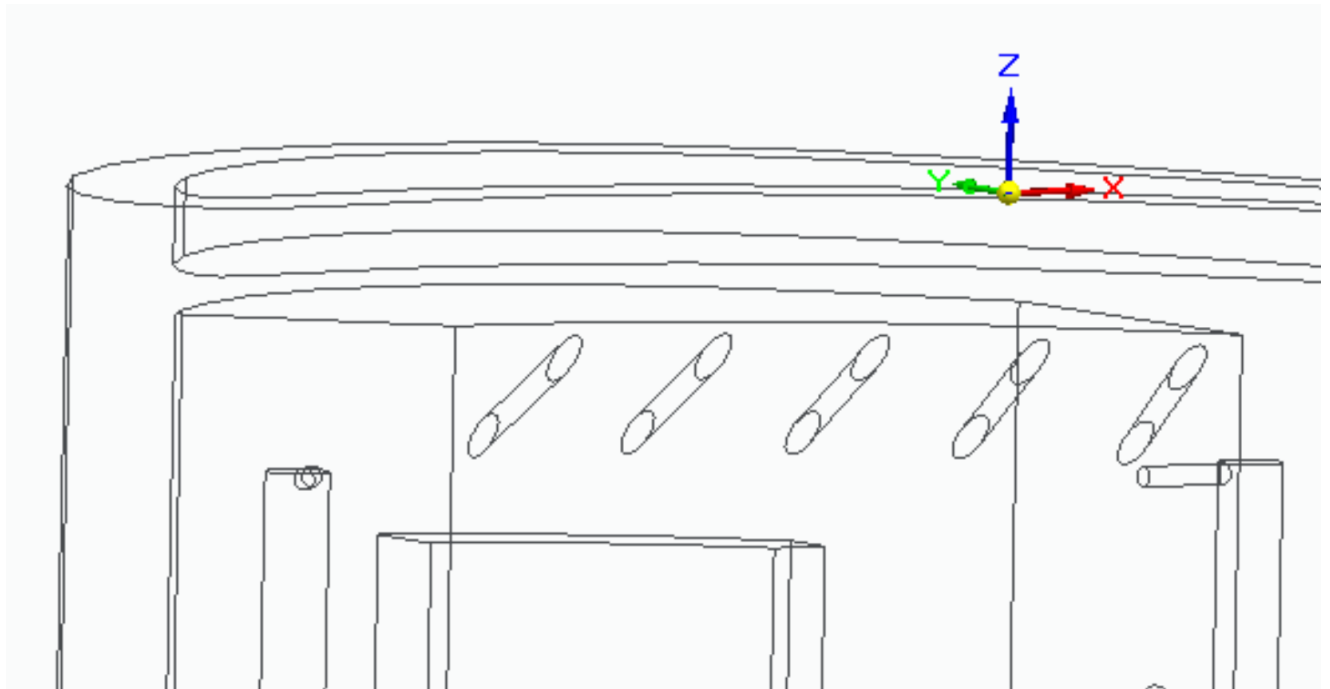


Figure 39. Detailed, transparent pressure side view of the film cooling hole geometry of the B1 film cooling configuration.

### 3.4 Baseline Data with Comparisons

Figure 40 presents heat transfer coefficient data 2020-01-07-1835 c0 baseline data, no film cooling, with BR=0 and a tip gap of 1.4 mm. Figure 41 presents heat transfer coefficient data 2020-01-12-1520 c0 baseline, no film cooling, with BR=0 and also a tip gap of 1.4 mm. Both of these baseline data sets are obtained with no film cooling (BR=0). Each data set is obtained with the B1 configuration airfoil. As these data are obtained, the film cooling holes are left open, but the film cooling supply passage is blocked internally.

Even though the two baseline data sets are obtained at different times, they are in excellent qualitative and quantitative agreement, including all surface heat transfer coefficient variations. Like other transonic blade tip data in the literature, these baseline data also show the higher heat transfer coefficients are present in the leading third of the airfoil surface. Dimensional heat transfer coefficient values further downstream of this region are generally lower. The initial high heat transfer coefficients on the leading edge and the upstream pressure side are high because of the initial development of a laminar boundary layer. Along the pressure side around mid-blade position, the values are lower because of separation along the squealer rim adjacent to the pressure side. Values just downstream of this location are in the vicinity of  $1700 \text{ W/m}^2 \text{ K}$ , where reattachment occurs. The separation occurs on top of the squealer rim, then reattachment occurs just downstream within the squealer recess. Local increases occur along trailing edge locations as well. Some of the changes occurring on the blade tip, both within the squealer recess and on the squealer rim, are due to the change from subsonic to supersonic flow. This is occurring around  $0.5 x/C_x$ , according to the data in Figure 32. This location corresponds to Y pixel locations between 300 and 400, and X pixel locations between 300 and 400.

The data in Figures 40 and 41 are also quantitatively and qualitatively similar to data from Viridi et al. (2015), especially the local heat transfer coefficient increases within the leading parts of the blade tip. The numerically predicted data from these researchers is shown in Figure 42, and the experimentally measured data from these researchers is shown in Figure 43. Note that the increases on the leading edge of the blade from the present investigation are less pronounced around the squealer rim, compared to the data from Viridi et al. (2015). Viridi et al. (2015) data are also obtained with a smooth-tipped blade, a squealer recess, a squealer rim, without film cooling, and a similar tip gap of 1.5 percent g/S, compared to our tip gap of 1.6 percent g/S.

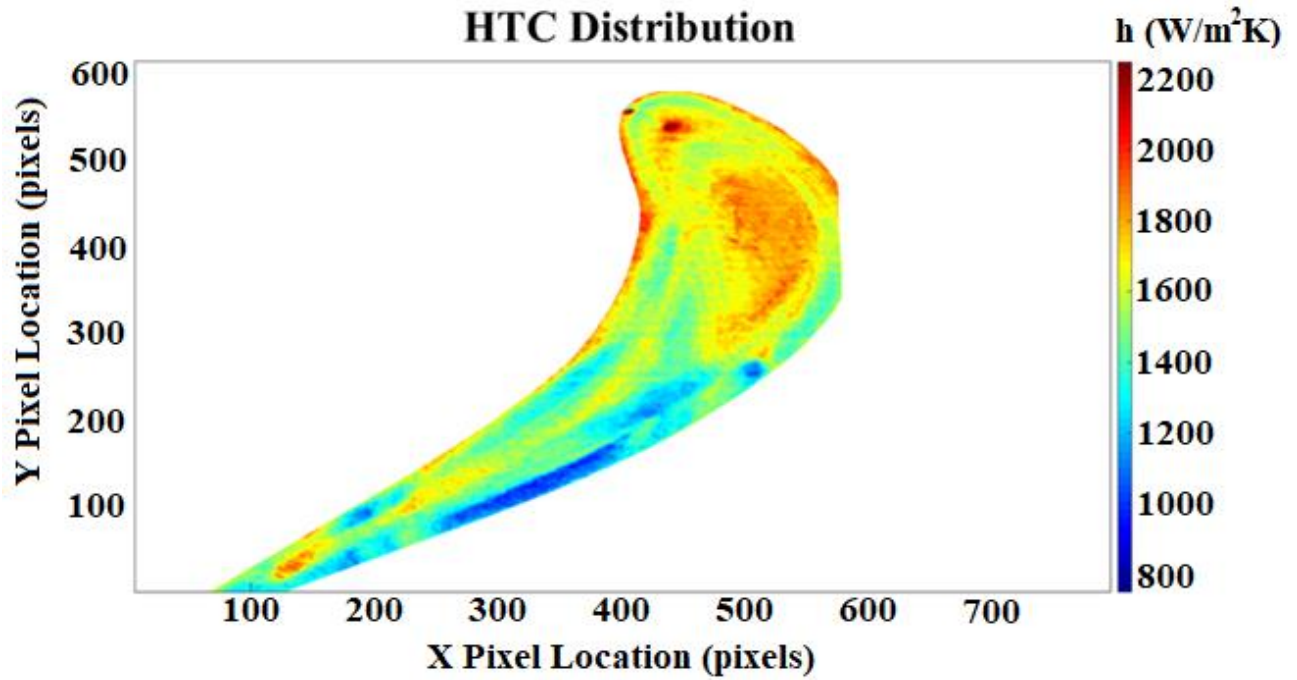


Figure 40. Heat transfer coefficient data 2020-01-07-1835 c0 baseline data, no film cooling, with BR=0 and a tip gap of 1.4 mm for the B1 film cooling configuration.

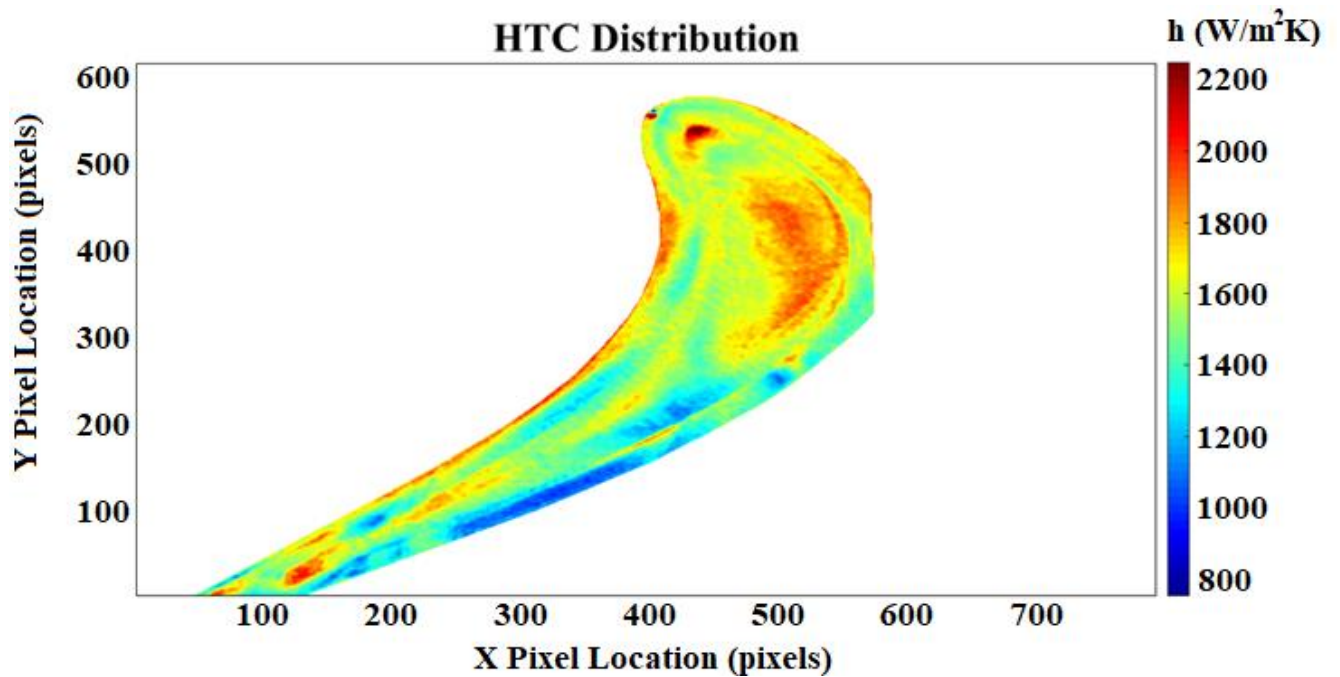


Figure 41. Heat transfer coefficient data 2020-01-12-1520 c0 baseline, no film cooling, with BR=0 and a tip gap of 1.4 mm for the B1 film cooling configuration.

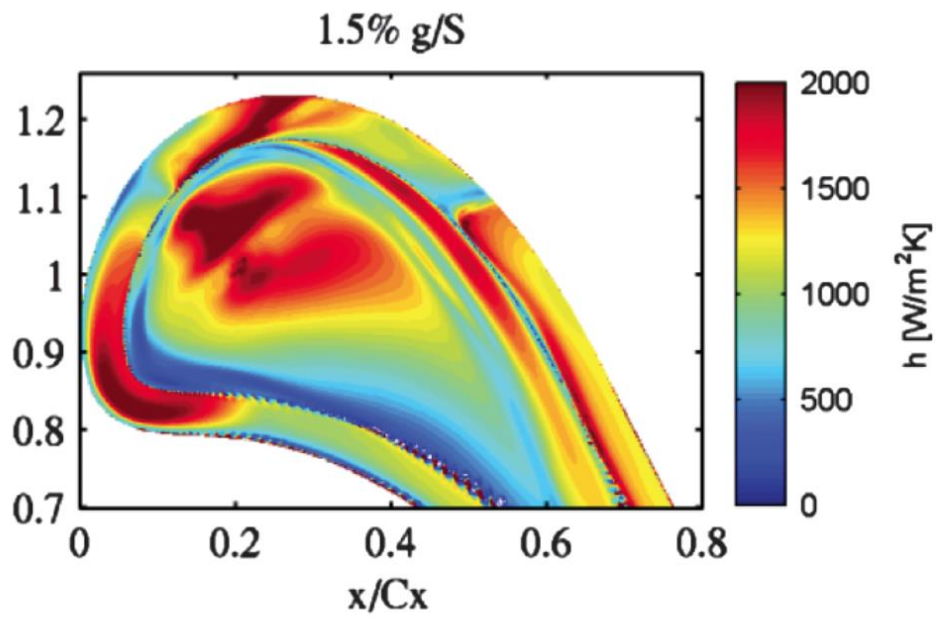


Figure 42. Numerically-predicted result. Viridi et al. (2015)

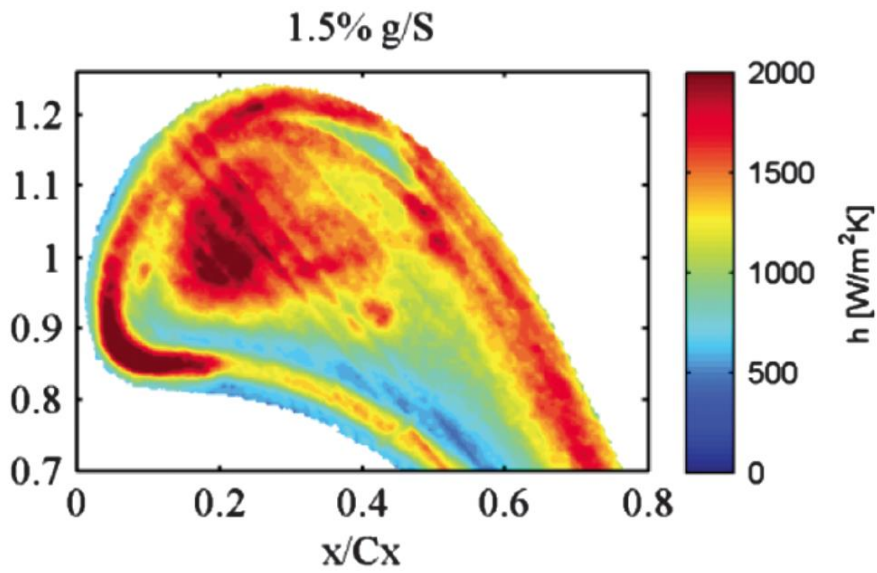


Figure 43. Experimentally-measured result. Viridi et al. (2015)

### 3.5 Data Defects

Defects exist in the heat transfer coefficient and film cooling effectiveness data because of tabs that are installed for thermocouples used to measure surface temperatures. These create local disturbances on the surface of the airfoil that locally increase the surface heat transfer coefficient slightly, as seen in Figure 46. These disturbances are present because the tabs are not perfectly aligned with the surface contour due to manufacturing tolerances.

As mentioned, these surface temperature measurements are used for calibration of infrared camera images. The locations of these thermocouple tabs for the B1 configuration airfoil are shown in Figure 44. The locations of thermocouples along these tabs, as well as additional information on tab locations and orientations are given in Figure 45. The exact thermocouple locations are tabulated in a table part (b) of Figure 45.

Also present are defects and data errors due to scratches on the zinc selenide window. These are most apparent in film cooling effectiveness data. An example of such a defect from a scratch on the zinc selenide window is shown in Figure 47.

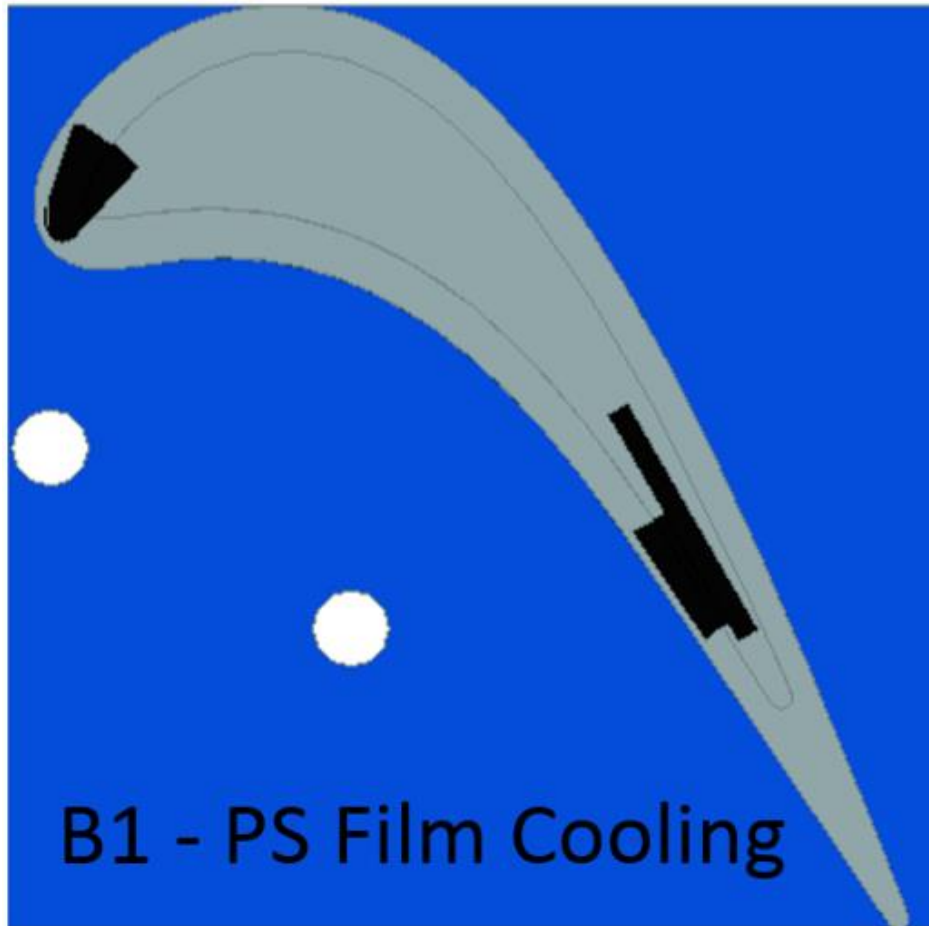
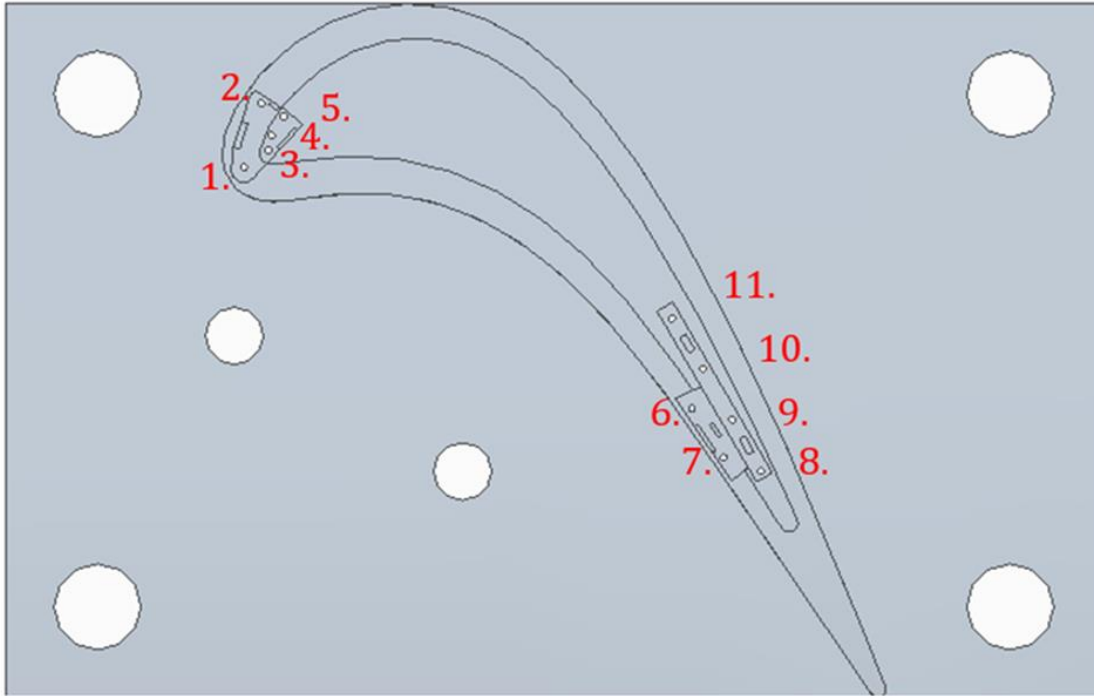


Figure 44. Blade tip thermocouple insert locations for the B1 film cooling configuration.

(a)



(b)

Thermocouple Inserts		
No.	x (mm)	x/Cx
1	2.41	0.033149
2	4.29	0.059009
3	5.07	0.069738
4	5.42	0.074552
5	6.78	0.093259
6	51.47	0.707968
7	54.96	0.755973
8	59.02	0.811818
9	55.89	0.768765
10	52.67	0.724474
11	49.28	0.677845

Figure 45. (a) Top view showing thermocouple locations and (b) exact thermocouple locations, measured in the axial direction.

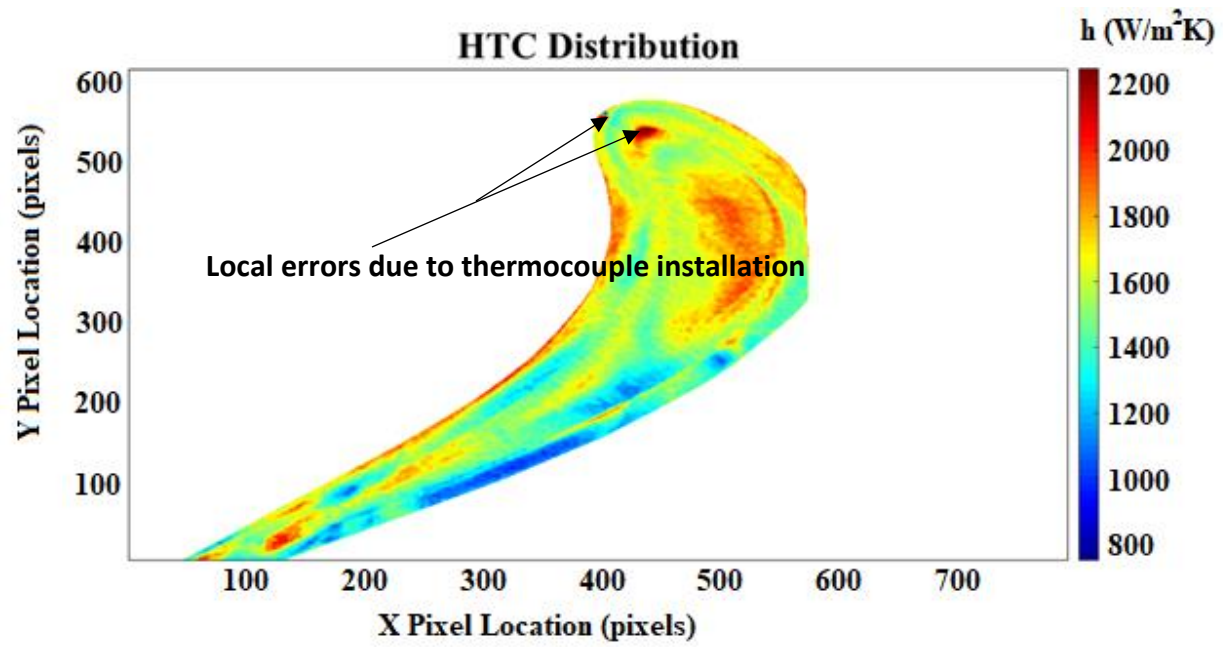


Figure 46. Local errors due to thermocouple installation.

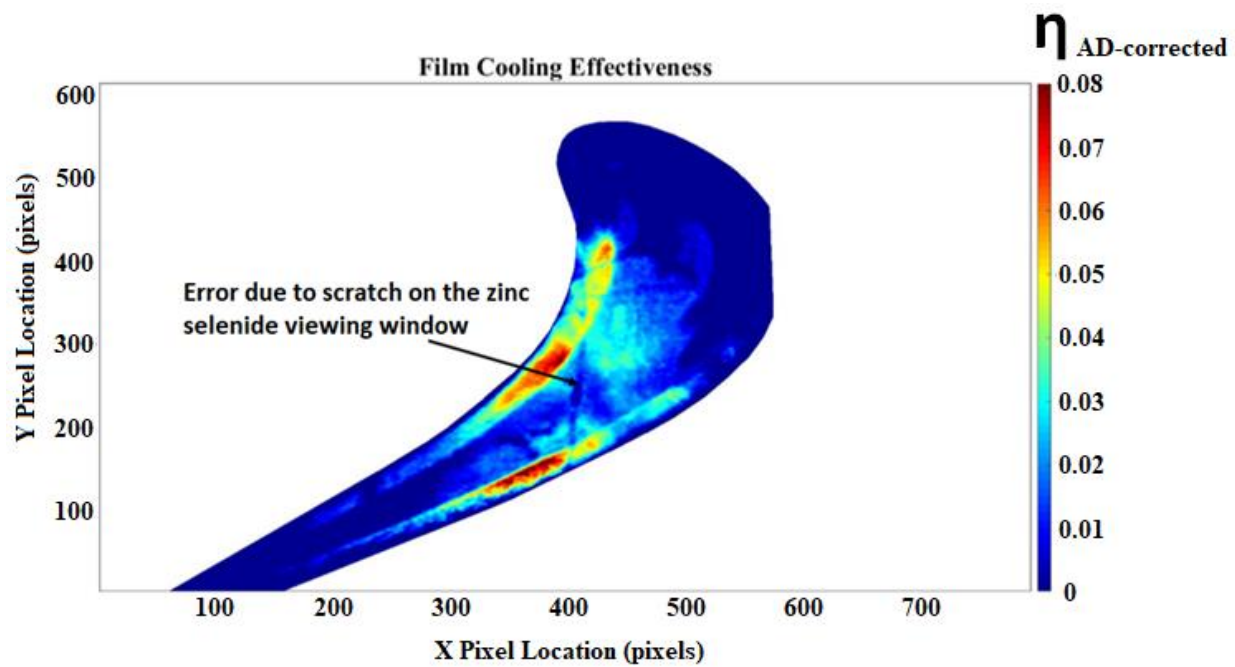


Figure 47. Local error due to scratch on zinc selenide viewing window.



### 3.6 Data for BR=3.18

Figures 48, 49, 50, and 51 show data for 2020-01-12-1445 c23. These data are obtained with a blowing ratio (BR) of 3.18 and a tip gap of 1.40 mm for the B1 film cooling configuration. Figure 48 shows heat transfer coefficient data. Figure 49 shows heat transfer coefficient ratio data. Figure 50 shows  $\eta_{AD-corrected}$  adiabatic film cooling effectiveness data. Figure 51 shows  $\eta_{AD-corrected-new}$  adiabatic film cooling effectiveness data. Note that  $\eta_{AD-corrected}$  and  $\eta_{AD-corrected-new}$  are given by equations (6) and (7).

The heat transfer coefficient data in Figure 48 are very similar to baseline data shown in Figures 40 and 41. Some small variations are evident along the pressure side of the squealer rim and on the suction side of the squealer rim. Otherwise, important quantitative differences with the baseline data are difficult to discern. Additional evidence of these variations are shown in the heat transfer coefficient ratio data in Figure 49. This heat transfer coefficient ratio is determined as the data with film cooling divided by the data without film cooling. The largest variations occur on the downstream part of the suction side squealer rim. These ratio values are as low as 0.70 to 0.75, locally. This is evidence of the presence of coolant, which affects the squealer rim on the suction side. To accomplish this, the coolant emerges from the pressure side film cooling holes, advects up the pressure surface, encounters the corner between the pressure surface and suction side squealer rim, then, separates along that rim and reattach within the recess. Some of the coolant also advects through the tip gap (1.4 mm) passage and collects near the suction side squealer rim.

Additional effects of the B1 film cooling arrangement on the blade tip with the squealer rim are evident from the adiabatic film cooling effectiveness data found in Figures 50 and 51. The increase in local film cooling effectiveness values, shown in Figures 50 and 51, illustrates the trajectory and distribution of the coolant along the pressure side rim, suction side rim, and the recess for the B1 film cooling configuration. Value variations are more apparent in Figure 51 where the  $\eta_{AD-corrected-new}$  are generally higher than the  $\eta_{AD-corrected}$  data in Figure 50, when compared at the same surface location. The B1 film cooling arrangement has effects locally on the pressure side rim, within the recess, and on the suction side rim. Note that the values are very low in the corner between the pressure side and the pressure side squealer rim because of local separation of the coolant from the surface. Values of film cooling effectiveness as high as 0.07 are found on the squealer rim in Figure 50 and as high as 0.08 in Figure 51. Within the recess, local values are

between 0.025 and 0.035 in Figure 50 and between 0.035 and 0.045 in Figure 51. On the pressure side rim, the values are between 0.03 and 0.04 in Figure 50 and between 0.045 and 0.055 in Figure 51. These values are augmented along the trajectory of the coolant which emerges from the B1 film cooling holes. Note that for other locations on the pressure side rim, suction side rim, and squealer recess, film cooling effectiveness values are generally very near zero.

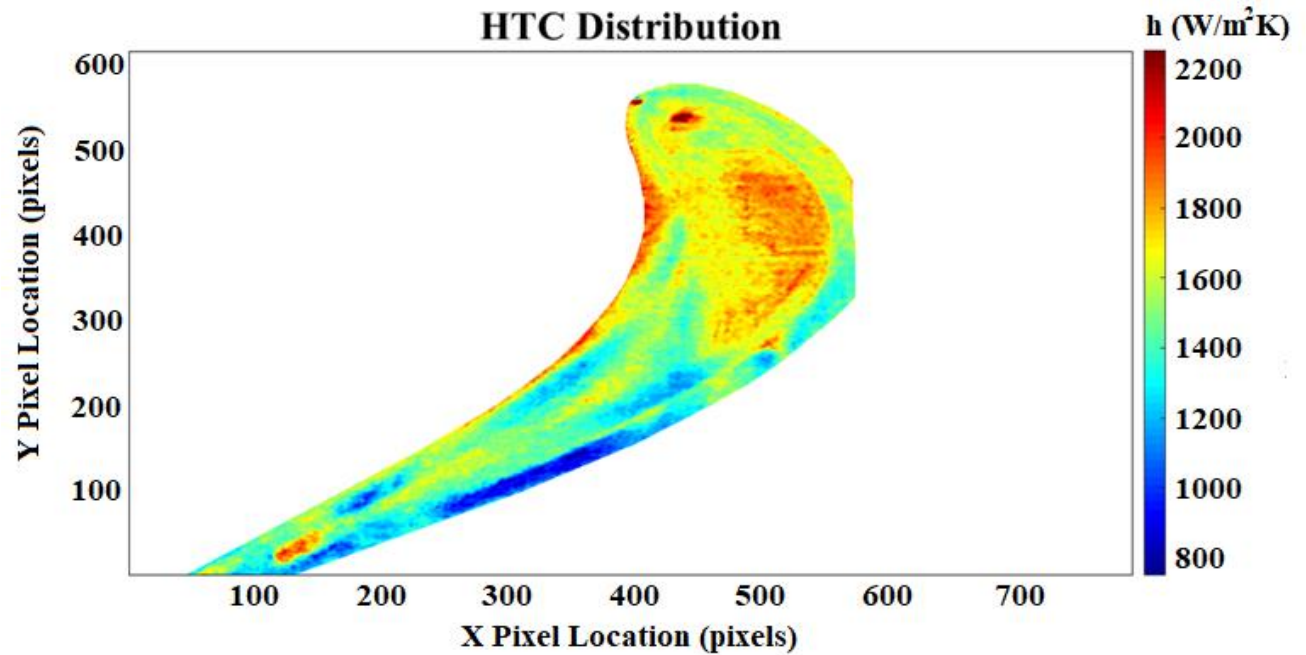


Figure 48. Heat transfer coefficient data 2020-01-12-1445 c23 with BR=3.18 and a tip gap of 1.4 mm for the B1 film cooling configuration.

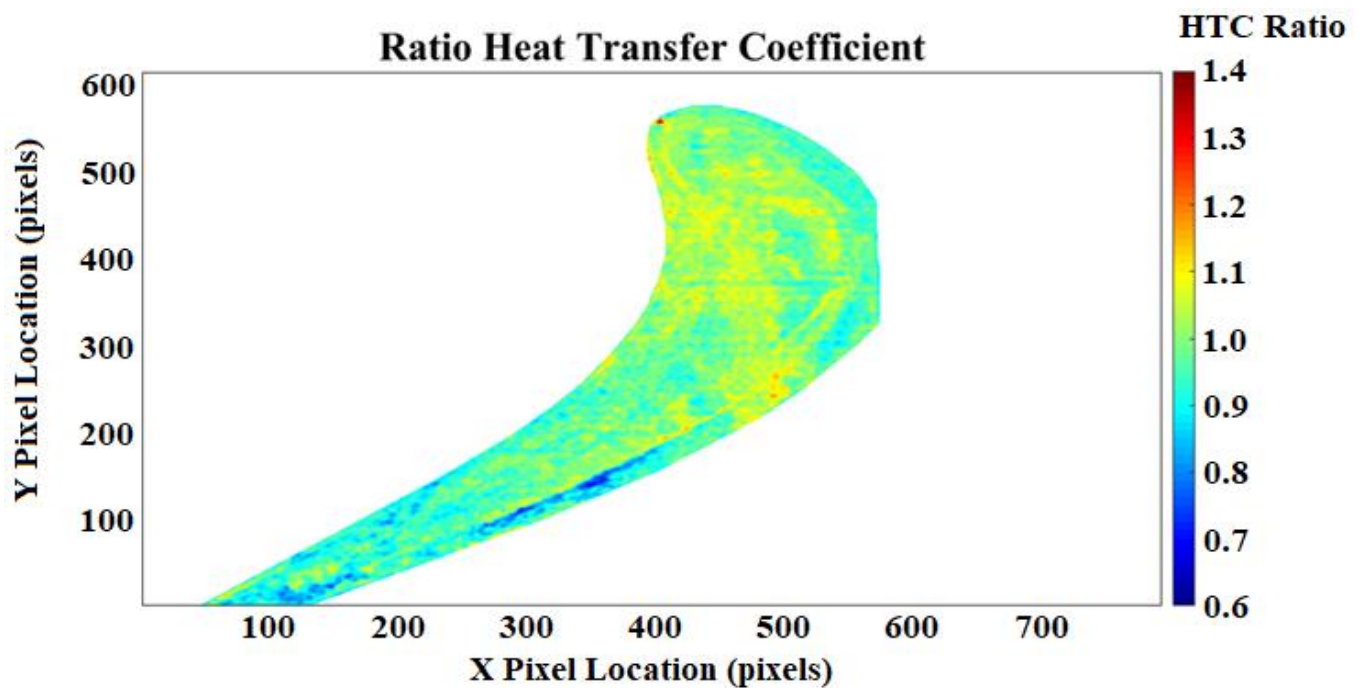
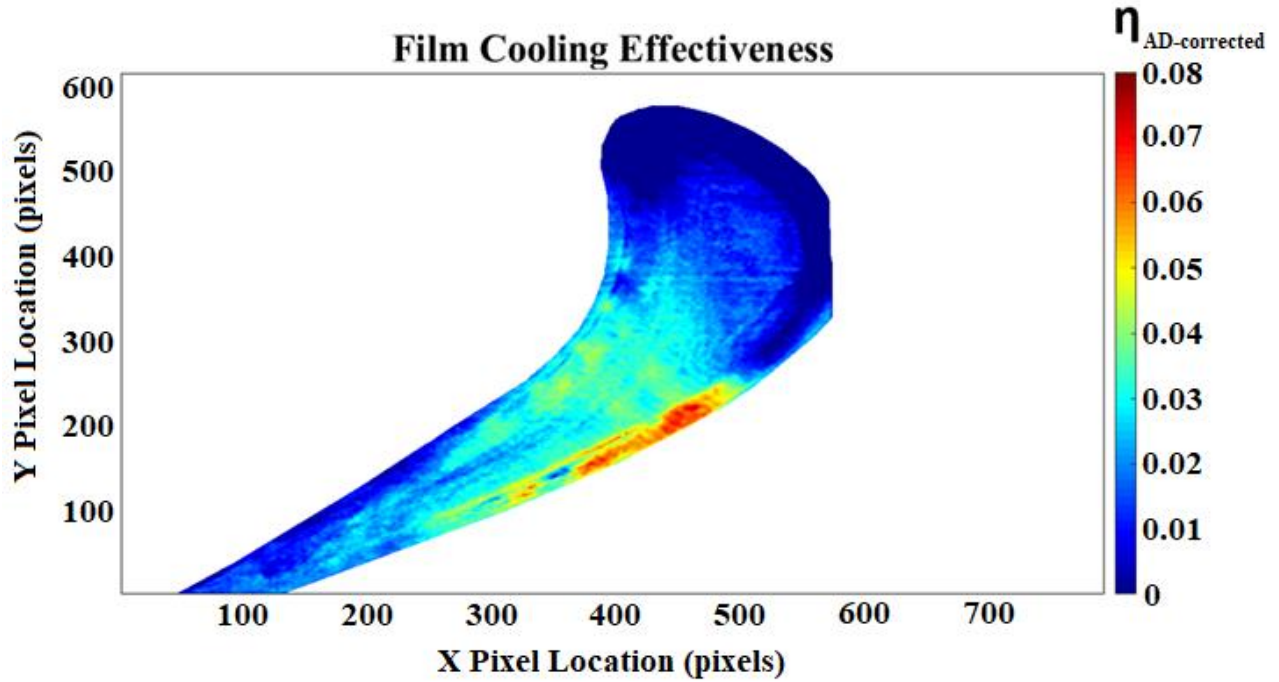
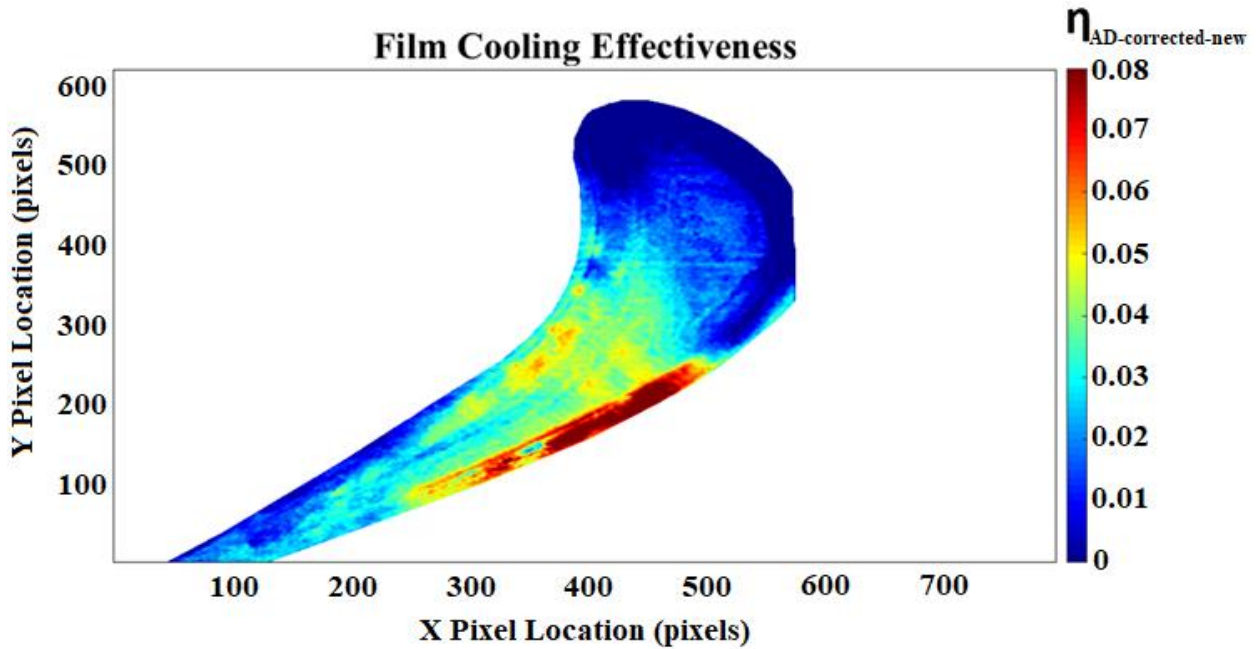


Figure 49. Heat transfer coefficient ratio data 2020-01-12-1445 c23 with BR=3.18 and a tip gap of 1.4 mm for the B1 film cooling configuration.



$$\eta_{AD-corrected} = [T_{AW-NFC} - T_{AW-FC}] / [T_{o-inlet} - T_{o-c}]$$

Figure 50. Adiabatic film cooling effectiveness data 2020-01-12-1445 c23 with BR=3.18 and a tip gap of 1.4 mm for the B1 film cooling configuration.

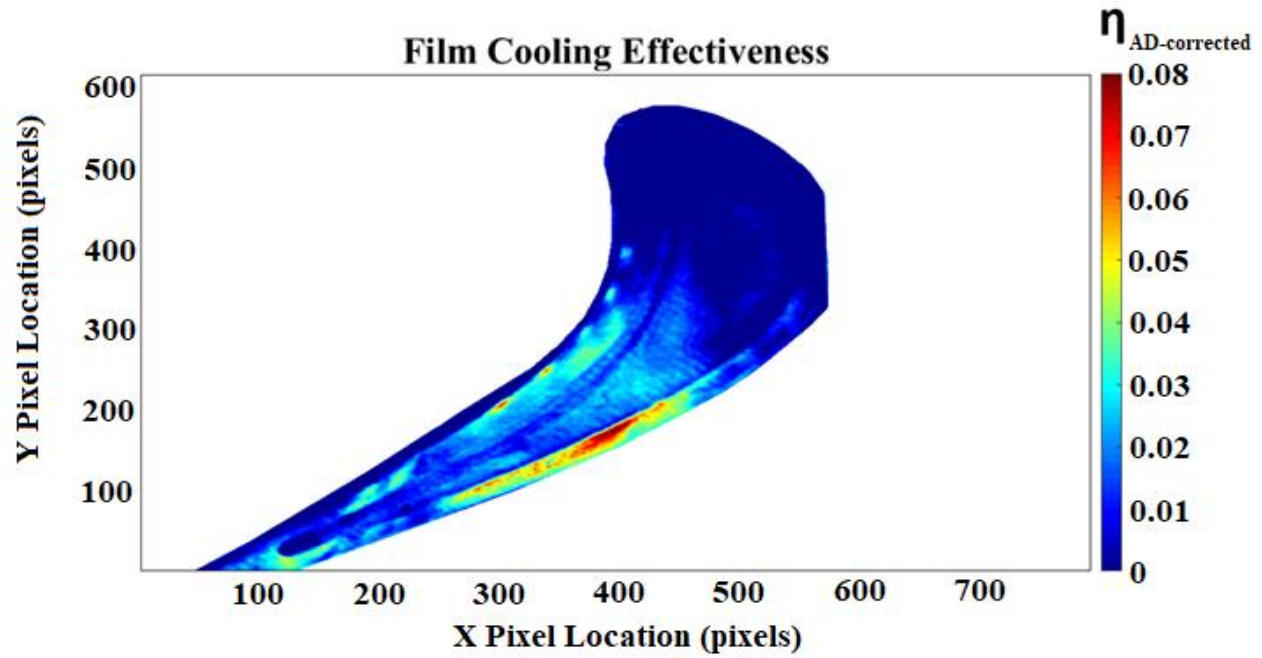


$$\eta_{AD-corrected-new} = [T_{AW-NFC} - T_{AW-FC}] / [T_{AW-NFC} - T_{o-c}]$$

Figure 51. Adiabatic film cooling effectiveness data 2020-01-12-1445 c23 with BR=3.18 and a tip gap of 1.4 mm for the B1 film cooling configuration.

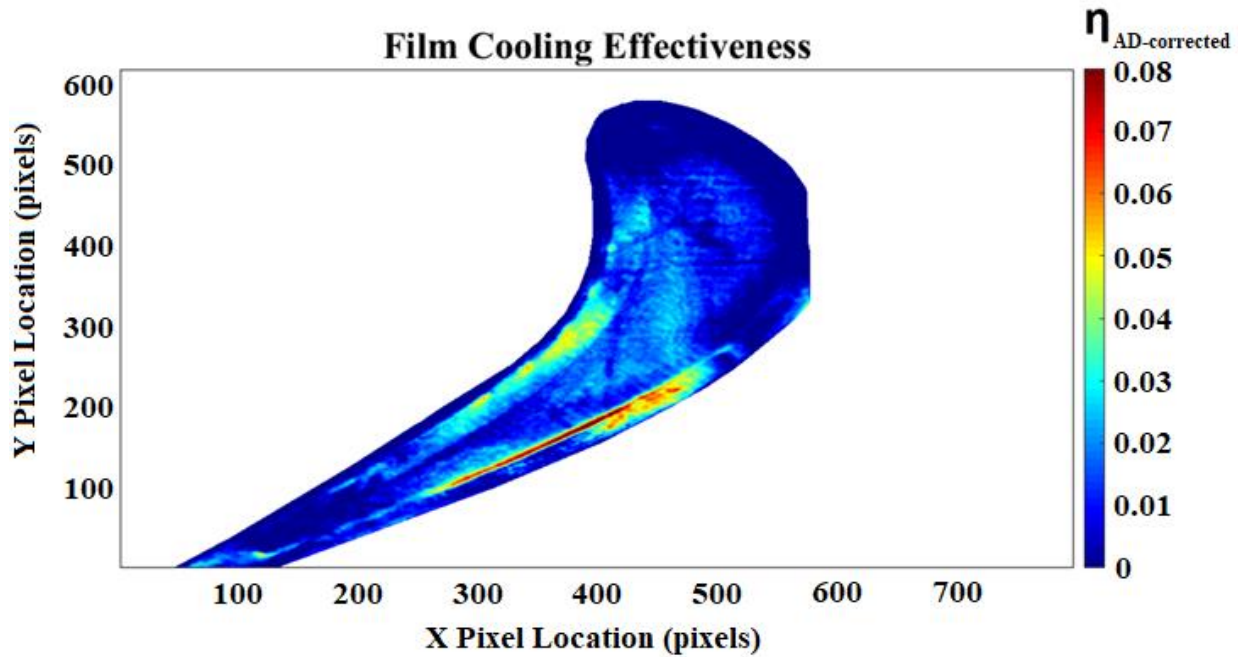
### 3.7 Comparison of First Type of Film Cooling Effectiveness

Figure 52 shows  $\eta_{AD-corrected}$  adiabatic film cooling effectiveness data 2020-01-12-1320 c16 with BR=0.49 and a tip gap of 1.4 mm for the B1 film cooling configuration. Figure 53 shows  $\eta_{AD-corrected}$  adiabatic film cooling effectiveness data 2020-01-07-1930 c15 with BR=1.12 and a tip gap of 1.4 mm for the B1 film cooling configuration. Figure 54 shows  $\eta_{AD-corrected}$  adiabatic film cooling effectiveness data 2020-01-12-1350 c18 with BR=2.01 and a tip gap of 1.4 mm for the B1 film cooling configuration. Figure 55 shows  $\eta_{AD-corrected}$  adiabatic film cooling effectiveness data 2020-01-12-1505 c26 with BR=3.85 and a tip gap of 1.4 mm for the B1 film cooling configuration. Note that these data are also compared to the data in Figure 50. The data are given for the sequence of blowing ratios equal to 0.49, 1.12, 2.01, 3.18, and 3.85. The same qualitative trends are apparent in all of these figures due to the trajectory of the coolant from the B1 film cooling holes. Locally higher film cooling effectiveness values are evident locally on portions of the pressure side rim, portions of the recess, and on portions of the suction side rim. These values of film cooling effectiveness at these locations increase to maximum values for blowing ratios of 2.01, 3.85, and 3.18. Values seem to increase as blowing ratio increases over this range. In some cases, such as in Figure 55 with a blowing ratio of 3.85, distinct signatures of the coolant are apparent along the rim near the pressure side. The film cooling effectiveness data in Figures 52 and 53, with respective blowing ratios of 0.49 and 1.12, are generally lower when compared to data at higher blowing ratios at the same blade tip locations.



$$\eta_{AD-corrected} = [T_{AW-NFC} - T_{AW-FC}] / [T_{o-inlet} - T_{o-c}]$$

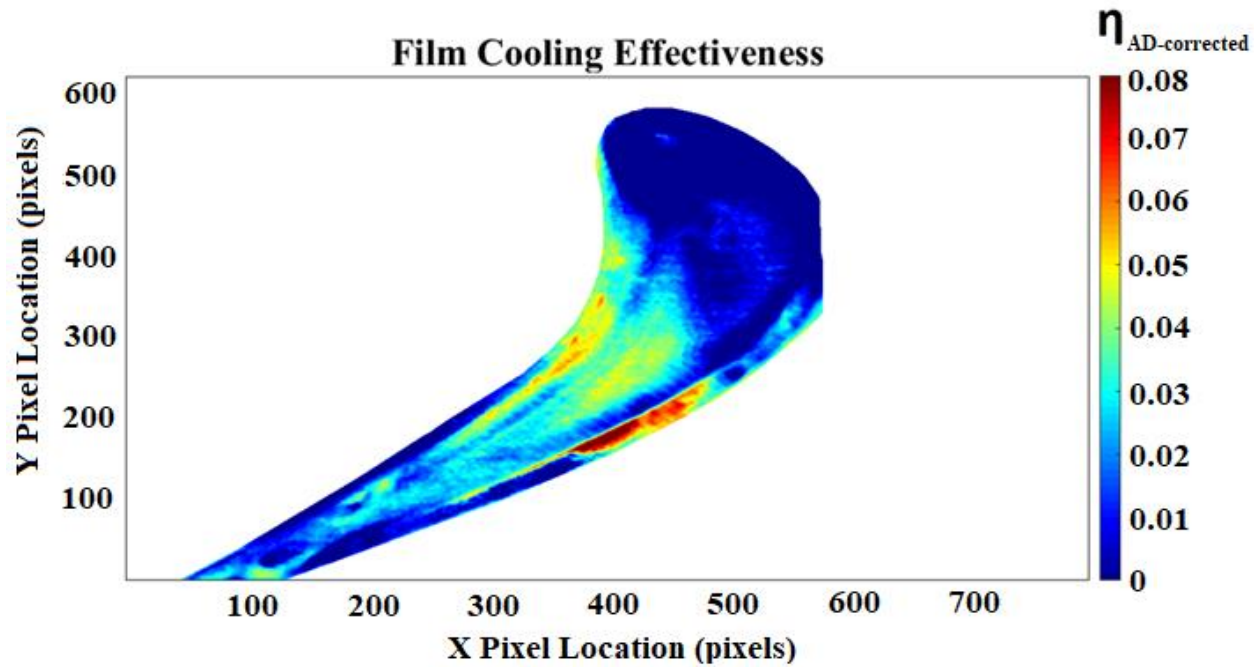
Figure 52. Adiabatic film cooling effectiveness data 2020-01-12-1320 c16 with BR=0.49 and a tip gap of 1.4 mm for the B1 film cooling configuration.



$$\eta_{AD-corrected} = [T_{AW-NFC} - T_{AW-FC}] / [T_{o-inlet} - T_{o-c}]$$

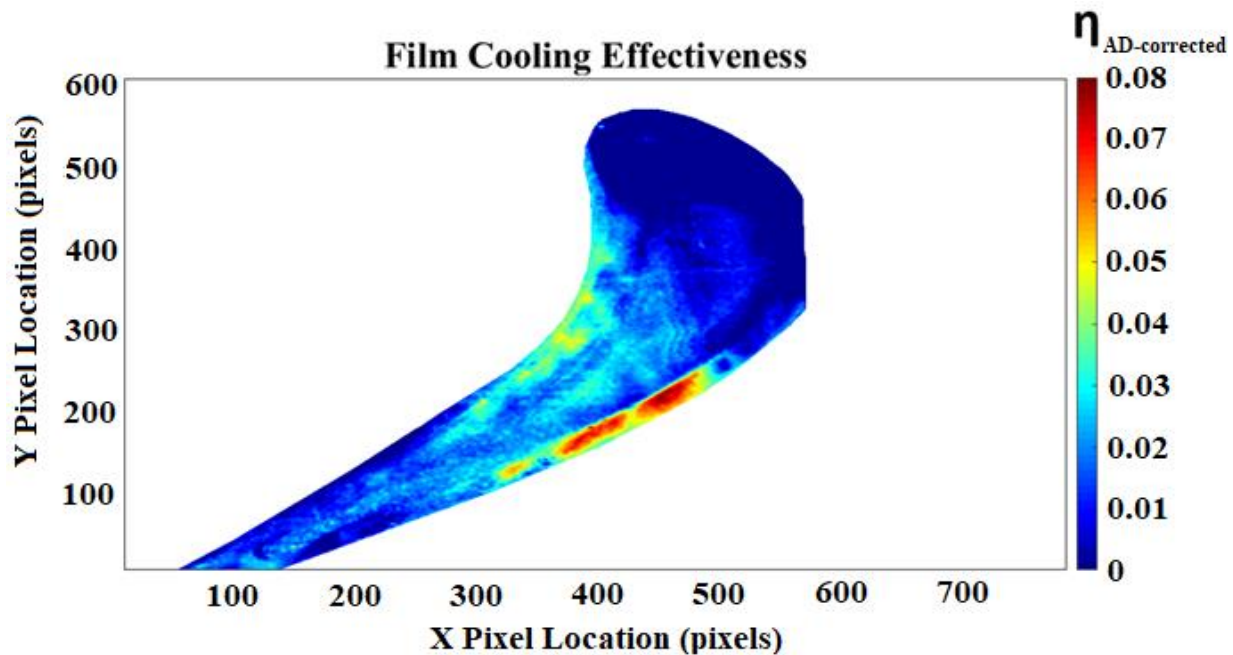
Figure 53. Adiabatic film cooling effectiveness data 2020-01-07-1930 c15 with BR=1.12 and a tip gap of 1.4 mm for the B1 film cooling configuration.





$$\eta_{AD-corrected} = [T_{AW-NFC} - T_{AW-FC}] / [T_{o-inlet} - T_{o-c}]$$

Figure 54. Adiabatic film cooling effectiveness data 2020-01-12-1350 c18 with BR=2.01 and a tip gap of 1.4 mm for the B1 film cooling configuration.



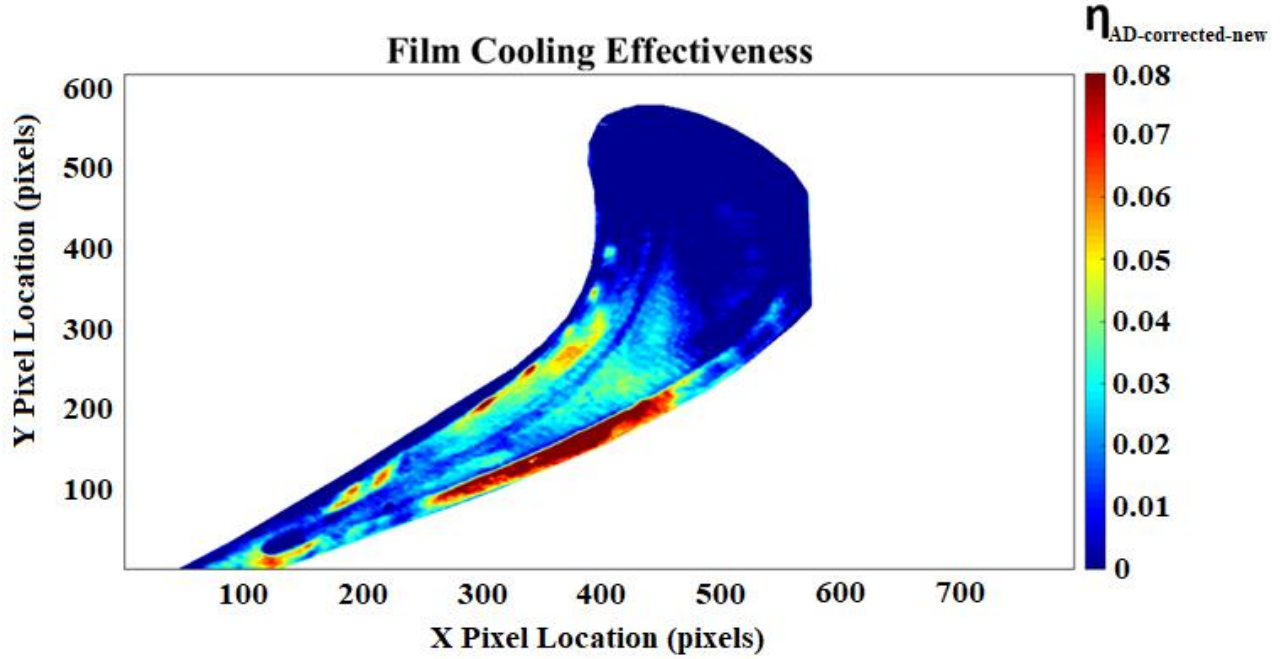
$$\eta_{AD-corrected} = [T_{AW-NFC} - T_{AW-FC}] / [T_{o-inlet} - T_{o-c}]$$

Figure 55. Adiabatic film cooling effectiveness data 2020-01-12-1505 c26 with BR=3.85 and a tip gap of 1.4 mm for the B1 film cooling configuration.

### 3.8 Comparisons of Second Type of Film Cooling Effectiveness

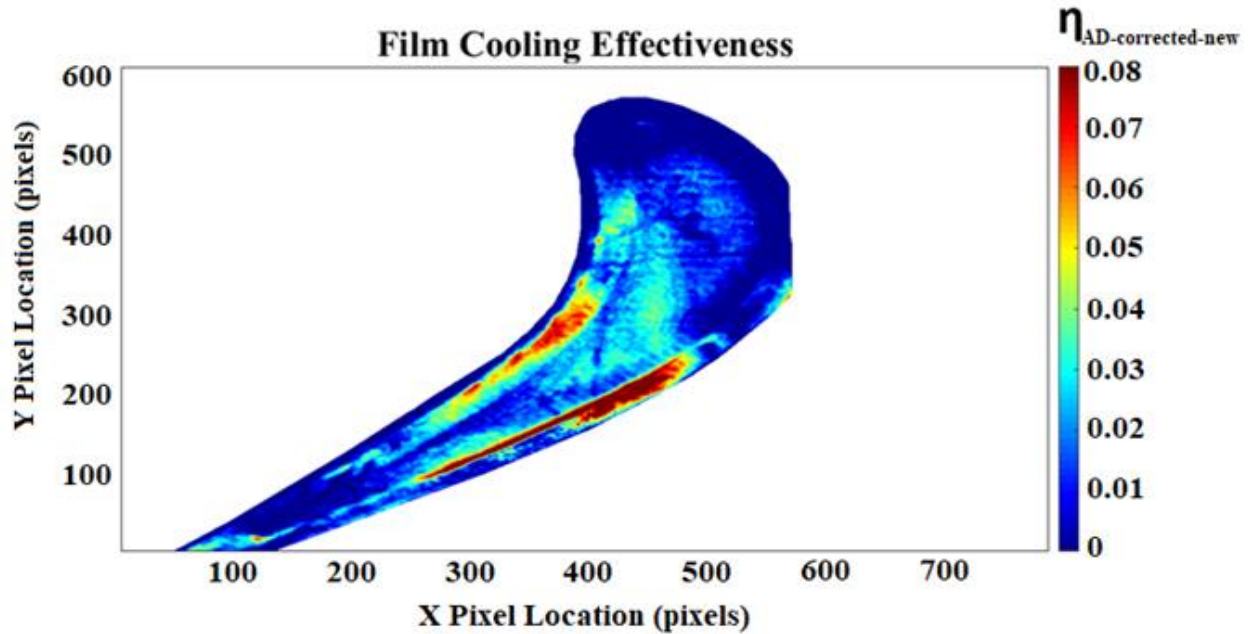
Figure 56 presents  $\eta_{AD-corrected-new}$  adiabatic film cooling effectiveness data 2020-01-12-1320 c16 with BR=0.49 and a tip gap of 1.4 mm for the B1 film cooling configuration. Figure 57 presents  $\eta_{AD-corrected-new}$  adiabatic film cooling effectiveness data 2020-01-07-1930 c15 with BR=1.12 and a tip gap of 1.4 mm for the B1 film cooling configuration. Figure 58 presents  $\eta_{AD-corrected-new}$  adiabatic film cooling effectiveness data 2020-01-12-1350 c18 with BR=2.01 and a tip gap of 1.4 mm for the B1 film cooling configuration. Figure 59 presents  $\eta_{AD-corrected-new}$  adiabatic film cooling effectiveness data 2020-01-12-1505 c26 with BR=3.85 and a tip gap of 1.4 mm for the B1 film cooling configuration. Figures 52, 53, 54, 55, and 50 are compared to data in Figures 56, 57, 58, 59, and 51. Note that the data in these different collections of figures are not directly proportional because of the varying values of  $T_{AW-NFC}$  which is present along the squealer tip and present from one data set to another. The trends in the two collections of figures are similar, but the values of  $\eta_{AD-corrected-new}$  are higher relative to  $\eta_{AD-corrected}$  values, when compared at the same squealer blade tip location.





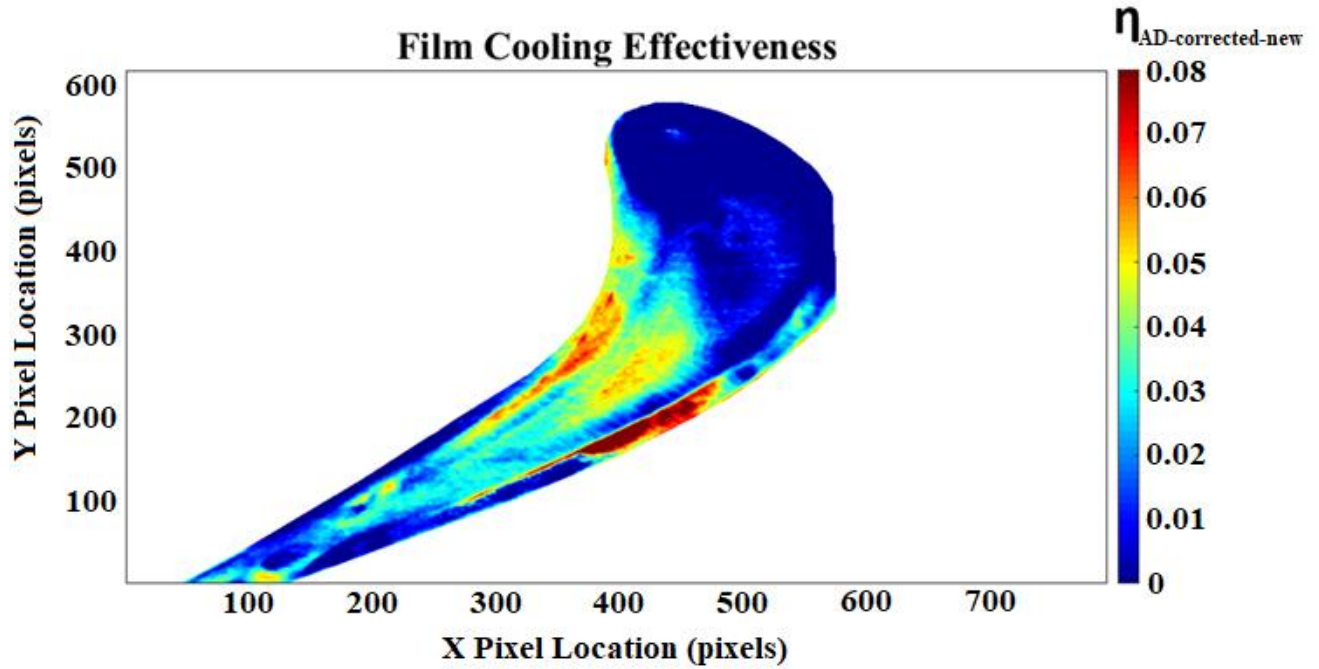
$$\eta_{AD-corrected-new} = [T_{AW-NFC} - T_{AW-FC}] / [T_{AW-NFC} - T_{o-c}]$$

Figure 56. Adiabatic film cooling effectiveness data 2020-01-12-1320 c16 with BR=0.49 and a tip gap of 1.4 mm for the B1 film cooling configuration.



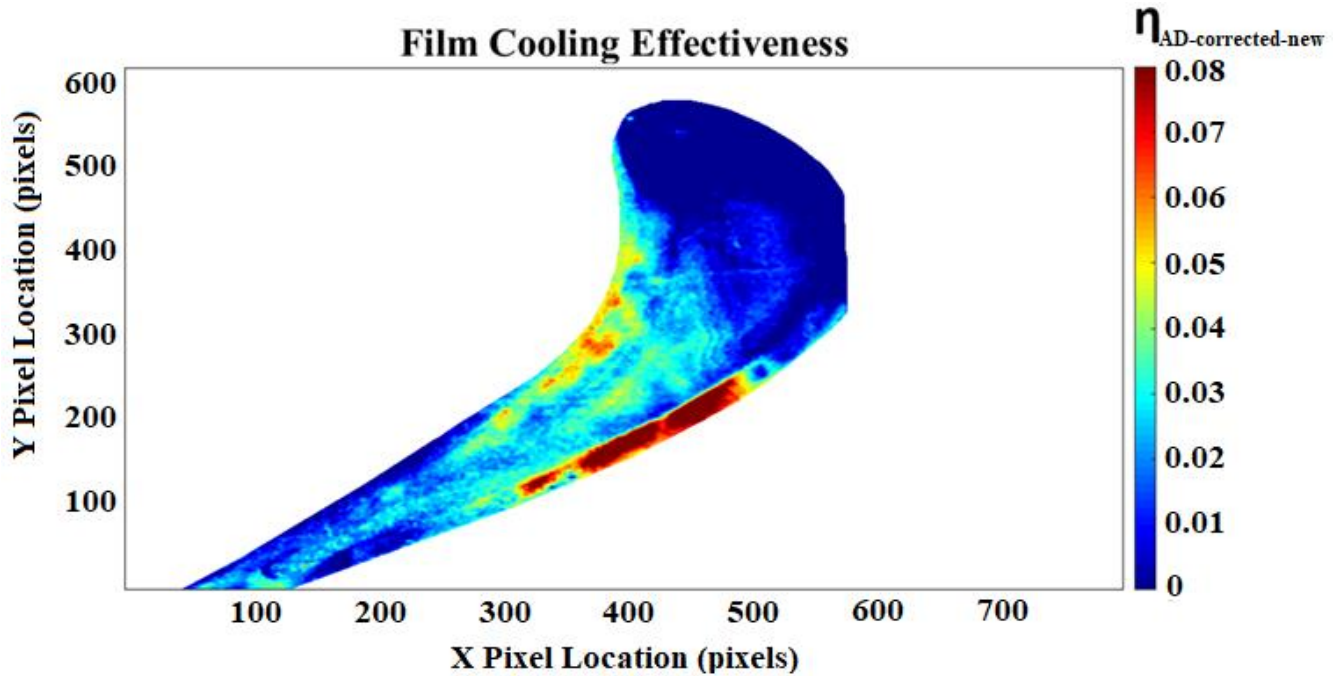
$$\eta_{AD-corrected-new} = [T_{AW-NFC} - T_{AW-FC}] / [T_{AW-NFC} - T_{o-c}]$$

Figure 57. Adiabatic film cooling effectiveness data 2020-01-07-1930 c15 with BR=1.12 and a tip gap of 1.4 mm for the B1 film cooling configuration.



$$\eta_{AD-corrected-new} = [T_{AW-NFC} - T_{AW-FC}] / [T_{AW-NFC} - T_{o-c}]$$

Figure 58. Adiabatic film cooling effectiveness data 2020-01-12-1350 c18 with BR=2.01 and a tip gap of 1.4 mm for the B1 film cooling configuration.



$$\eta_{AD-corrected-new} = [T_{AW-NFC} - T_{AW-FC}] / [T_{AW-NFC} - T_{o-c}]$$

Figure 59. Adiabatic film cooling effectiveness data 2020-01-12-1505 c26 with BR=3.85 and a tip gap of 1.4 mm for the B1 film cooling configuration.

## CHAPTER 4

### SUMMARY AND CONCLUSIONS

Within the present test facility, investigated are spatially-resolved distributions of surface adiabatic film cooling effectiveness and surface heat transfer coefficients for a transonic turbine blade tip. The tip contains a squealer rim, and a single row of film cooling holes is located on the pressure-side of the blade very near to the blade tip. Also measured are surface static pressure distributions, and associated isentropic Mach numbers, around the blade surface at the 50 percent airfoil span location, around the blade surface at the 90 percent airfoil span location, the blade tip, and the end wall. A two-dimensional linear cascade is employed with four flow passages and five complete blades is employed, which includes radial and circumferential boundary layer flow bleed devices, and an inlet grid to augment cascade inlet passage turbulence intensity. With the bar grid employed to augment the mainstream turbulence intensity level, the value is six to seven percent at the exit of the nozzle, which is upstream of the test section. The cascade is designed to provide geometric similarity with the engine application environment, including inlet boundary layer thickness, blade configuration (including blade axial chord length, and blade true chord length), cascade arrangement (including blade pitch, blade span, and inlet flow angle), blade tip geometry, squealer depth, squealer wall thickness, and tip gap magnitudes.

The wind tunnel is a blow-down facility. The working fluid is dried air. The facility is comprised of a high-pressure piping system, a low-pressure piping system, two test section assemblies, and exhaust piping. The facility has the capability to vary a number of different parameters, including tip gap magnitude, squealer depth, film cooling configuration, and all film cooling characterization parameters, with one squealer tip configuration for one blade airfoil. The facility also has the capability to vary the squealer tip configuration. In the present study, only one squealer configuration is employed. A transient thermal measurement technique is employed to determine spatially resolved distributions of adiabatic surface temperature, adiabatic film cooling effectiveness, and surface heat transfer coefficients along the blade tip with the squealer rim.

For both the 50 percent and 90 percent span locations, the pressure side of the blade is always subsonic, reaching a maximum Mach number of approximately 0.8 at the trailing edge where it meets the flow from the suction side of the blade. For the 50 percent span location, Mach numbers along the suction side increase with streamwise development, reaching a maximum value of 1.1 at  $0.8 x/C_x$ . Mach numbers along the suction side for the 90 percent span location increase

with streamwise development, reaching a maximum value of 1.24 at  $0.8 x/C_x$ . For the blade tip, the isentropic Mach number is approximately 0.5 from  $0.11 x/C_x$  to  $0.44 x/C_x$ , followed by a local increase to approximately Mach 1.25 from  $0.55 x/C_x$  to  $0.86 x/C_x$ . The end wall pressure taps, located at 0.5 and 1.0 axial chord lengths downstream of the turbine blades, show approximate periodicity and repeatability, relative to different blade passages.

The two baseline heat transfer data sets are obtained at different times, but are in excellent qualitative and quantitative agreement, including all surface heat transfer coefficient variations. Like other transonic blade tip data in the literature, these baseline data also show the higher heat transfer coefficients are present in the leading third of the airfoil surface. The data for a blowing ratio (BR) of 3.18 show small variations along the pressure side of the squealer rim and on the suction side of the squealer rim. Otherwise, important quantitative differences with the baseline data are difficult to discern. Additional evidence of these variations are shown in the heat transfer coefficient ratio data. This heat transfer coefficient ratio is determined as the data with film cooling divided by the data without film cooling. The largest variations occur on the downstream part of the suction side squealer rim. These ratio values are as low as 0.70 to 0.75, locally. Two different types of film cooling effectiveness data are given for blowing ratios equal to 0.49, 1.12, 2.01, 3.18, and 3.85. The same qualitative trends are apparent in both types of film cooling effectiveness. Variations of film cooling effectiveness are generally due to the trajectory, concentrations, and distributions of the coolant from the B1 film cooling holes. Highest film cooling effectiveness values are evident on the pressure side rim, within the recess, and on the suction side rim. These values of film cooling effectiveness are locally maximum for blowing ratios of 2.01, 3.18, and 3.85. Over this range of blowing ratios, values generally increase with blowing ratio. These values are augmented along the trajectory of the coolant which emerges from the B1 film cooling holes. Note that for other locations on the pressure side rim, suction side rim, and squealer recess, film cooling effectiveness values are generally very near zero.

## APPENDIX A

### EXPERIMENTAL CONDITIONS

(a) Constants for Facility					
Air		CO2		Dimensions	
R (kJ/kgmolK)	8.314	R (kJ/kgm	8.314	<b>Film Cooling Holes</b>	<b>Orifice</b>
M (kg/Kmol)	28.9647	M (kg/Km	44.01		
R=R/M (KJ/kgK)	0.287039	R=R/M (KJ	0.188911611	A_fc (m^2)	6.94E-07
k	1.4	k	1.3	A_fc (5 holes) (m^2)	3.47E-06
C_p (Kj/kgK)	1.006	C_p (Kj/k€	0.846 KJ/kgK		
</					

Figure A1. (a) Constants for facility and (b) measured information for 2020-01-12-1320 c16 data.

(a)

Film Cooling Calculations						
Film Cooling Calculations		Film Cooling Parameters				
$[\rho_{cs} v_c] = \frac{\dot{m}_c}{A_c}$	89.79462 kg/(m^2s)	Blowing Ratio	BR	0.494412056		
$Mc$	0.135986	Velocity Ratio	VR	0.31088301		
$T_{Sc}$	287.3838 K	Density Ratio	DR	1.590347625		
$\rho_{cs}$	3.757987 kg/(m^3)	Momentum Flux Ratio	I	0.153704308		
$C_c$	265.6637				Discharge Coefficient Parameters	
$v_c$	23.89434				3.47E-06 m^2	A_fc (5 holes) (m^2)
Mc	0.135986				M_c	0.135986
					k_co2	1.3
					R_co2	188.9116 J/KgK
					T_Tc	288.181
					PTc	205860

(b)

Variable Properties	
$\rho_{c,ideal}$	3.781592 kg/m <sup>3</sup>
$c_{c,ideal}$	266.0237 m/s
$M_{c,ideal}$	0.117536
$v_{c,ideal}$	31.26737 m/s
$\dot{m}_{c,ideal}$	0.00041 kg/s
$\dot{m}_c$	0.000312 kg/s
CD	0.759424

Figure A2. (a) Film cooling calculations and (b) variable properties for 2020-01-12-1320 c16 data.

(a)	Constants for Facility					
	Air		CO2		Dimensions	
R (kJ/kgmolK)	8.314	R (kJ/kgm	8.314	<u>Film Cooling Holes</u>		<u>Orifice</u>
M (kg/Kmol)	28.9647	M (kg/Km	44.01	d_fc (m)	0.00094	d_1 (in) 0.824
						d_1(m) 0.02093
R=R/M (KJ/kgK)	0.287039	R=R/M (KJ	0.188911611	A_fc (m^2)	6.94E-07	d_throat ( 0.1
						d_throat ( 0.00254
k	1.4	k	1.3	A_fc (5 holes) (m^2)	3.47E-06	A_throat ( 5.07E-06
C_p (KJ/kgK)	1.006	C_p (KJ/kg	0.846 KJ/kgK			A_1 (m^2) 0.000344
						Area Ratic 67.8976

	<u>Measured Information</u>			
(b)	Inlet Cascade	Main Flow at Exit Film Cooling Holes	Film Cooling Plenum	Sonic Orifice
	$P_{T_{oo,inlet}}$ 28.50995 psi 196569.3 Pa		Co2 Setting 15	$P_T$ 32.20422 psi 222040.4 Pa
	$P_{Soo,inlet}$ 26.96212 psi 185897.3 Pa		$P_{ct1}$ 31.16912 psi $P_{ct2}$ 31.16912 psi $P_{Tc}$ 31.16912 psi 214903.6 Pa	$T_T$ 14.71137 C 287.8614 K
	$M_{oo,inlet}$ 0.283519	$M_{fc}$ 0.221068853		
	$T_{r_{oo,inlet}}$ 28.20892 C	$\rho_{fc}$ 2.376361054	$T_{Tc}$ 13.17277 C	Sonic Orifice Calculations
	Recovery factor 301.3589 K	$T_{tfc}$ 302.0279418 K $T_{zfc}$ 299.1044093	286.3228 K	$\frac{\dot{m}_c \sqrt{T_T}}{A^* P_T} = 0.0485$
	$T_{soo,inlet}$ 297.2492 K	$c_{fc}$ 346.6936747 m/s		
	$T_{Too,inlet}$ 302.0279 K	$v_{fc}$ 76.64317302 m/s		$\dot{m}_c$ 0.000708 kg/s
	$C_{oo,inlet}$ 345.6168 m/s	Data Set:	Data Set 2020_01_07_1930_c	
	$V_{oo,inlet}$ 97.98879 m/s	2019_12_06 18_25 SP 50 at 20 s (x/cx 0.48)	15	
	$\rho_{oo,inlet}$ 2.17877 kg/(m <sup>3</sup> )			

Figure A3. (a) Constants for facility and (b) measured information for 2020-01-07-1930 c15 data.

(a)

Film Cooling Calculations					
Film Cooling Calculations		Film Cooling Parameters			
$[\rho_{cs} v_c] = \frac{\dot{m}_c}{A_c}$	204.1239 kg/(m <sup>2</sup> s)	<b>Blowing Ratio</b>	<b>BR</b>	<b>1.120748159</b>	
$M_c$	0.203451	<b>Velocity Ratio</b>	<b>VR</b>	<b>0.701730966</b>	
$T_{Sc}$	284.556 K	<b>Density Ratio</b>	<b>DR</b>	<b>1.597119428</b>	
$\rho_{cs}$	3.795332 kg/(m <sup>3</sup> )	<b>Momentum Flux Ratio</b>	<b>I</b>	<b>0.786463688</b>	
$c_c$	264.3534				Discharge Coefficient Parameters
$v_c$	53.78289				3.47E-06 m <sup>2</sup>   A_fc (5 holes) (m <sup>2</sup> )
$M_c$	0.203451				M_c 0.203451
					k_co2 1.3
					R_co2 188.9116 J/KgK
					T_Tc 286.3228
					PTc 214903.6

(b)

Variable Properties	
$\rho_{c,ideal}$	3.973341 kg/m <sup>3</sup>
$c_{c,ideal}$	265.1646 m/s
$M_{c,ideal}$	0.283593
$v_{c,ideal}$	75.19896 m/s
$\dot{m}_{c,ideal}$	0.001037 kg/s
$\dot{m}_c$	0.000708 kg/s
CD	0.683166

Figure A4. (a) Film cooling calculations and (b) variable properties for 2020-01-07-1930 c15 data.



(a)

Constants for Facility					
Air		CO2		Dimensions	
R (kJ/kgmolK)	8.314	R (kJ/kgm	8.314	<b>Film Cooling Holes</b>	
M (kg/Kmol)	28.9647	M (kg/Km	44.01	<b>Orifice</b>	
R=R/M (KJ/kgK)	0.287039	R=R/M (KJ	0.188911611	d_fc (m)	0.00094
k	1.4	k	1.3	A_fc (m^2)	6.94E-07
C_p (Kj/kgK)	1.006	C_p (Kj/kg	0.846 KJ/kgK	A_fc (5 holes) (m^2)	3.47E-06
				d_1 (in)	0.824
				d_1(m)	0.02093
				d_throat (	0.1
				d_throat (	0.00254
				A_throat (	5.07E-06
				A_1 (m^2)	0.000344
				Area Ratic	67.8976

(b)

Measured Information							
Inlet Cascade		Main Flow at Exit Film Cooling Holes		Film Cooling Plenum		Sonic Orifice	
$P_{T\infty,inlet}$	27.78572 psi			Co2 Setting	18	$P_T$	35.55785 psi
	191575.9 Pa			$P_{ct1}$	33.84525 psi		245162.8 Pa
$P_{S\infty,inlet}$	26.58906 psi			$P_{ct2}$	33.84525 psi	$T_T$	4.104006 C
	183325.2 Pa			$P_{Tc}$	33.84525 psi		277.254 K
$M_{\infty,inlet}$	0.251568	$M_{fc}$	0.221068853		233354.8 Pa		
$T_{T\infty,inlet}$	28.40414 C	$\rho_{fc}$	2.375929885	$T_{Tc}$	11.89818 C	Sonic Orifice Calculations	
	301.5541 K	$T_{tfc}$	302.082752 K		285.0482 K	$\frac{\dot{m}_c \sqrt{T_T}}{A^* P_T} = 0.0485$	
Recovery factor	0.86	$T_{zfc}$	299.158689				
$T_{S\infty,inlet}$	298.307 K	$c_{fc}$	346.7251313 m/s				
$T_{T\infty,inlet}$	302.0828 K	$v_{fc}$	76.65012708 m/s				
$c_{\infty,inlet}$	346.2312 m/s	Data Set:	2019_12_06 18_25 SP 50 at 20 s (x/cx 0.48)	Data Set	2020_01_12_350_c1	$\dot{m}_c$	0.001268 kg/s
$v_{\infty,inlet}$	87.10085 m/s				8		
$\rho_{\infty,inlet}$	2.141005 kg/(m^3)						

Figure A5. (a) Constants for facility and (b) measured information for 2020-01-12-1350 c18 data.

(a)

Film Cooling Calculations				
Film Cooling Calculations		Film Cooling Parameters		
$[\rho_{cs}v_c] = \frac{\dot{m}_c}{A_c}$	365.3547 kg/(m <sup>2</sup> s)	<b>Blowing Ratio</b>	<b>BR</b>	<b>2.006172146</b>
$Mc$	0.360966	<b>Velocity Ratio</b>	<b>VR</b>	<b>1.233946508</b>
$T_{Sc}$	279.5839 K	<b>Density Ratio</b>	<b>DR</b>	<b>1.625817758</b>
$\rho_{cs}$	3.862829 kg/(m <sup>3</sup> )	<b>Momentum Flux Ratio</b>	<b>I</b>	<b>2.475509115</b>
$c_c$	262.0336	<div>Discharge Coefficient Parameters</div> <div> <div>3.47E-06 m<sup>2</sup></div> <div>A_fc (5 holes) (m<sup>2</sup>)</div> </div> <div> <div>M_c</div> <div>0.360954</div> </div> <div> <div>k_co2</div> <div>1.3</div> </div> <div> <div>R_co2</div> <div>188.9116 J/KgK</div> </div> <div> <div>T_Tc</div> <div>285.0482</div> </div> <div> <div>P_Tc</div> <div>233354.8</div> </div>		
$v_c$	94.58216			
$Mc$	0.360954			

(b)

Variable Properties	
$\rho_{c,ideal}$	4.333777 kg/m <sup>3</sup>
$c_{c,ideal}$	264.5738 m/s
$M_{c,ideal}$	0.458154
$v_{c,ideal}$	121.2154 m/s
$\dot{m}_{c,ideal}$	0.001823 kg/s
$\dot{m}_c$	0.001268 kg/s
CD	0.695489

Figure A6. (a) Film cooling calculations and (b) variable properties for 2020-01-12-1350 c18 data.

(a)		Constants for Facility			
Air		CO2		Dimensions	
R (kJ/kgmolK)	8.314	R (kJ/kgm	8.314	<u>Film Cooling Holes</u>	<u>Orifice</u>
M (kg/Kmol)	28.9647	M (kg/Km	44.01	d_fc (m)	0.00094
				d_1 (in)	0.824
				d_1(m)	0.02093
R=R/M (KJ/kgK)	0.287039	R=R/M (KJ	0.188911611	d_throat (	0.1
				d_throat (	0.00254
k	1.4	k	1.3	A_fc (5 holes) (m^2)	3.47E-06
C_p (Kj/kgK)	1.006	C_p (Kj/kg	0.846 Kj/kgK	A_throat (	5.07E-06
				A_1 (m^2)	0.000344
				Area Ratic	67.8976

		Measured Information			
Inlet Cascade		Main Flow at Exit Film Cooling Holes		Film Cooling Plenum	Sonic Orifice
$P_{T, \text{inlet}}$	27.57517 psi			Co2 Setting 23	$P_T$ 40.90632 psi
	190124.2 Pa			$P_{ct1}$ 38.46143 psi	282039.3 Pa
$P_{Soo, \text{inlet}}$	26.15701 psi			$P_{ct2}$ 38.46143 psi	$T_T$ 1.473767 C
	180346.3 Pa			$P_{Tc}$ 38.46143 psi	274.6238 K
$M_{\infty, \text{inlet}}$	0.275679	$M_{fc}$ 0.221068853		265182.4 Pa	
$T_{\infty, \text{inlet}}$	28.43974 C	$\rho_{fc}$ 2.37482551		$T_{Tc}$ 11.15598 C	Sonic Orifice Calculations
	301.5897 K	$T_{tfc}$ 302.2232307 K		284.306 K	$\frac{\dot{m}_c}{A^*} \sqrt{\frac{T_T}{P_T}} = 0.0485$
Recovery factor	0.86	$T_{zfc}$ 299.2978079			
$T_{Soo, \text{inlet}}$	297.6983 K	$c_{fc}$ 346.8057413 m/s			
$T_{T\infty, \text{inlet}}$	302.2232 K	$P_{fc}$ 76.66794746 m/s			$\dot{m}_c$ 0.00201 kg/s
$c_{\infty, \text{inlet}}$	345.8778 m/s	Data Set:		Data Set 2020_01_07_1445_c	
$v_{\infty, \text{inlet}}$	95.35109 m/s	2019_12_06 18_25 SP 50 at 20 s (x/α 0.48)		23	
$\rho_{\infty, \text{inlet}}$	2.110522 kg/(m^3)				

Figure A7. (a) Constants for facility and (b) measured information for 2020-01-12-1445 c23 data.



(a)

Constants for Facility					
Air		CO2		Dimensions	
R (kJ/kgmolK)	8.314	R (kJ/kgm	8.314	<b>Film Cooling Holes</b>	
M (kg/Kmol)	28.9647	M (kg/Km	44.01	d_fc (m)	0.00094
R=R/M (KJ/kgK)	0.287039	R=R/M (KJ	0.188911611	A_fc (m^2)	6.94E-07
k	1.4	k	1.3	A_fc (5 holes) (m^2)	3.47E-06
C_p (KJ/kgK)	1.006	C_p (KJ/kg	0.846 KJ/kgK	<b>Orifice</b>	
				d_1 (in)	0.824
				d_1(m)	0.02093
				d_throat (	0.1
				d_throat (	0.00254
				A_throat (	5.07E-06
				A_1 (m^2)	0.000344
				Area Ratic	67.8976

(b)

Measured Information					
Inlet Cascade		Main Flow at Exit Film Cooling Holes		Film Cooling Plenum	
$P_{T\infty,inlet}$	27.36978 psi			Co2 Setting	26
	188708 Pa			$P_{ct1}$	41.17959 psi
$P_{S\infty,inlet}$	25.94677 psi			$P_{ct2}$	41.17959 psi
	178896.7 Pa			$P_{Tc}$	41.17959 psi
$M_{\infty,inlet}$	0.277235	$M_{fc}$	0.221068853		283923.4 Pa
$T_{\infty,inlet}$	29.65797 C	$\rho_{fc}$	2.365215894	$T_{Tc}$	12.36842 C
	302.808 K	$T_{tfc}$	303.4511311 K		285.5184 K
Recovery factor	0.86	$T_{sfc}$	300.5138226	<b>Sonic Orifice Calculations</b>	
$T_{\infty,inlet}$	298.8571 K	$c_{fc}$	347.5095444 m/s	$\frac{\dot{m}_c \sqrt{T_T}}{A^* P_T} = 0.0485$	
$T_{T\infty,inlet}$	303.4511 K	$v_{fc}$	76.82353638 m/s	$\dot{m}_c$	
$c_{\infty,inlet}$	346.5503 m/s	Data Set:		2020_01_12_1505_c	
$v_{\infty,inlet}$	96.07601 m/s	2019_12_06 18_25 SP 50 at 20 s (x/ $\alpha$ 0.48)		26	
$\rho_{\infty,inlet}$	2.085441 kg/(m^3)			0.002428 kg/s	

Figure A9. (a) Constants for facility and (b) measured information for 2020-01-12-1505 c26 data.

(a)

Film Cooling Calculations						
Film Cooling Calculations		Film Cooling Parameters				
$[\rho_{cs}v_c] = \frac{\dot{m}_c}{A_c}$	699.6581 kg/(m^2s)	Blowing Ratio	BR	3.850532314		
$Mc$	0.675719	Velocity Ratio	VR	2.253397815		
$T_{Sc}$	267.2169 K	Density Ratio	DR	1.708767217		
$\rho_{cs}$	4.041603 kg/(m^3)	Momentum Flux Ratio	I	8.676781102		
$C_c$	256.1728				Discharge Coefficient Parameters	
$v_c$	173.114				3.47E-06 m^2	A_fc (5 holes) (m^2)
$Mc$	0.67577				M_c	0.67577
					k_co2	1.3
					R_co2	188.9116 J/KgK
					T_Tc	285.5184
					PTc	283923.4

(b)

Variable Properties	
$\rho_{c,ideal}$	5.264232 kg/m <sup>3</sup>
$c_{c,ideal}$	264.7919 m/s
$M_{c,ideal}$	0.726855
$v_{c,ideal}$	192.4653 m/s
$\dot{m}_{c,ideal}$	0.003516 kg/s
$\dot{m}_c$	0.002428 kg/s
CD	0.690555

Figure A10. (a) Film cooling calculations and (b) variable properties for 2020-01-12-1505 c26 data.

## APPENDIX B

### DATA FILE DIRECTORY

Type of Data	Blowing Ratio	File Name	Date	Description
Pressure ratio and Mach number distributions	N/A	50 percent span 2019_10_09 17_30 SP 51 at 26.2s.xlsx	10-09-19	Excel file that contains output data from labview and calculations for pressure and Mach number distributions.
		90 percent span 2019_10_11_170 0_SP50 at 26.7 sec.xlsx	10-11-19	Excel file that contains output data from labview and calculations for pressure and Mach number distributions.
		2019_10_21_202 5_tip_SP50 at 24.4 tip.xlsx	10-21-19	Excel file that contains output data from labview and calculations for pressure and Mach number distributions.
		Downstream Pressure Results SP 47 EDIT.xlsx	10-09-19	Excel file that contains output data from labview and calculations for pressure distributions.
Heat transfer coefficient and adiabatic film cooling effectiveness	0	2020-01-12-1520 c0.xlsx	09-12-20	Pressure readings and Temperature readings from LabView
		2020-01-12- 1520_c0.avi		Raw output from Flir ResearchIR software containing all data from the infrared camera
		htc1520c0smooth .mat		Matrix of spatially resolved heat transfer coefficient

		Htc1520c0ratios mooth.mat		Matrix of ratio of spatially resolved heat transfer coefficient to baseline case without film cooling
		Eta1520c0asmoot h.mat		Matrix of adiabatic effectiveness relative to the mainstream temperature corrected for flow effects
		Eta1520c0bsmoot h.mat		Matrix of adiabatic effectiveness relative to the local wall temperature corrected for flow effects
Heat transfer coefficient and adiabatic film cooling effectiveness	0.49	2020_01_12_132 0_c16.xlsx	01-12-20	Pressure readings and Temperature readings from LabView
		2020_01_07_132 0_c16.avi		Raw output from Flir ResearchIR software containing all data from the infrared camera
		htc1320c16smoot h.mat		Matrix of spatially resolved heat transfer coefficient
		Htc1320c16ratios mooth.mat		Matrix of ratio of spatially resolved heat transfer coefficient to baseline case without film cooling
		Eta1320c16asmo oth.mat		Matrix of adiabatic effectiveness relative to the mainstream temperature corrected for flow effects
		Eta1320c16bsmo oth.mat		Matrix of adiabatic effectiveness relative to the



				local wall temperature corrected for flow effects
Heat transfer coefficient and adiabatic film cooling effectiveness	1.12	2020_01_07_193 0_c15.xlsx	01-07-20	Pressure readings and Temperature readings from LabView
		2020_01_07_193 0_c15.avi		Raw output from Flir ResearchIR software containing all data from the infrared camera
		htc1930c15smoot h.mat		Matrix of spatially resolved heat transfer coefficient
		htc1930c15ratios mooth.mat		Matrix of ratio of spatially resolved heat transfer coefficient to baseline case without film cooling
		eta1930c15asmoo th.mat		Matrix of adiabatic effectiveness relative to the mainstream temperature corrected for flow effects
		eta1930c15bsmoo th.mat		Matrix of adiabatic effectiveness relative to the local wall temperature corrected for flow effects
Heat transfer coefficient and adiabatic film cooling effectiveness	2.01	2020_01_12_135 0_c18.xlsx	01-12-20	Pressure readings and Temperature readings from LabView
		2020_01_07_135 0_c18.avi		Raw output from Flir ResearchIR software containing all data from the infrared camera

		htc1350c18smooth.mat		Matrix of spatially resolved heat transfer coefficient
		Htc1350c18ratiosmooth.mat		Matrix of ratio of spatially resolved heat transfer coefficient to baseline case without film cooling
		Eta1350c18asmooth.mat		Matrix of adiabatic effectiveness relative to the mainstream temperature corrected for flow effects
		Eta1350c18bsmooth.mat		Matrix of adiabatic effectiveness relative to the local wall temperature corrected for flow effects
Heat transfer coefficient and adiabatic film cooling effectiveness	3.18	2020_01_12_1350_c18.xlsx	01-12-20	Pressure readings and Temperature readings from LabView
		2020_01_07_1445_c23.avi		Raw output from Flir ResearchIR software containing all data from the infrared camera
		Htc1445c23smooth.mat		Matrix of spatially resolved heat transfer coefficient
		Htc1445c23ratiosmooth.mat		Matrix of ratio of spatially resolved heat transfer coefficient to baseline case without film cooling
		Eta1445c23asmooth.mat		Matrix of adiabatic effectiveness relative to the mainstream temperature corrected for flow effects

		Eta1445c23bsmooth.mat		Matrix of adiabatic effectiveness relative to the local wall temperature corrected for flow effects
Heat transfer coefficient and adiabatic film cooling effectiveness	3.85	2020_01_12_1505_c26.xlsx	01-12-20	Pressure readings and Temperature readings from LabView
		2020_01_07_1505_c26.avi		Raw output from Flir ResearchIR software containing all data from the infrared camera
		htc1505c26smooth.mat		Matrix of spatially resolved heat transfer coefficient
		Htc1505c26ratiosmooth.mat		Matrix of ratio of spatially resolved heat transfer coefficient to baseline case without film cooling
		Eta1505c26asmooth.mat		Matrix of adiabatic effectiveness relative to the mainstream temperature corrected for flow effects
		Eta1505c26bsmooth.mat		Matrix of adiabatic effectiveness relative to the local wall temperature corrected for flow effects

## APPENDIX C

### SOFTWARE DIRECTORY

Software	File Name	Description
LabView	PressureV3.vi	LabView program used to collect and store raw flow condition data from thermocouples and pressure transducers
Flir ResearchIR	N/A	Used to collect and store infrared images from the infrared camera
MATLAB	PostProccessing1update.m	Used to generate matrices of temperature from infrared video data
MATLAB	PostProccessing2update.m	Used to generate plots of results from matrices of heat transfer data
MATLAB	desT2qsiimp1.m	Subroutine used to calculate heat transfer
MATLAB	Airfoil.m	Used to plot ratios and line plot figures and extract the line plot data for heat transfer ratios and adiabatic effectiveness

## REFERENCES

- Anto, K., Xue, S., Ng, W., Zhang, L., Moon, H., 2013, “Effects of Tip Clearance Gap and Exit Mach Number on Turbine Blade Tip and Near-Tip Heat Transfer,” Paper No GT2013-94345, ASME Turbo Expo.
- Arisi, A., Phillips, J., Ng, W.F., Moon, H.K., Zhang, L., 2016, “An Experimental and Numerical Study on the Aerothermal Characteristics of a Ribbed Transonic Squealer-Tip Turbine Blade with Purge Flow,” *Journal of Turbomachinery*, 138, pp. 101007.
- Atkins, N.R., Thorpe, S.J., Ainsworth, R.W., 2012, “Unsteady Effects on Transonic Turbine Blade-Tip Heat Transfer,” *Journal of Turbomachinery*, 134, pp: 061002/1–061002/11.
- Chappell, J., Ligrani, P. M., Sreekanth, S., Lucas, T., and Vlasic, E., 2010, “Aerodynamic Performance of Suction-Side Gill Region Film Cooling,” *ASME Transactions-Journal of Turbomachinery*, 132(3), pp. 031020-1 to 031020-11.
- Collopy, H., Sampson, M., Ligrani, P. M., Moseley, J., Autrey, J., McNabb, E., Xu, H., Fox, M., 2020, “Adiabatic Effectiveness and Heat Transfer Coefficient Measurements for Innovative Film Cooling Arrangements on a Transonic Turbine Blade Tip”, Unpublished Manuscript.
- Didier, F., Denos, R., Arts, T., 2002, “Unsteady Rotor Heat Transfer in a Transonic Turbine Stage,” *Journal of Turbomachinery*, 123, pp. 81-89.
- Dunn, M.G., Haldeman, C.W., 2000 “Time-Averaged Heat Flux for a Recessed Tip, Lip, and Platform of a Transonic Turbine Blade,” *Journal of Turbomachinery*, 122, pp. 692-698.
- Gao, J., Zheng, Q., Dong, P., Fu, W., 2017, “Effects of Flow Incidence on Aerothermal Performance of Transonic Blade Tip Clearance Flows,” *Energy*, 139, pp. 196–209.
- Green, B.R., Barter, J.W., Haldeman, C.W., Dunn, M.G., 2005, “Averaged and Time-Dependent Aerodynamics of a High Pressure Turbine Blade Tip Cavity and Stationary Shroud: Comparison of Computational and Experimental Results,” *Journal of Turbomachinery*, 127, pp. 736-746.

- Hofer, T., Arts, T., 2009, "Aerodynamic Investigation of the Tip Leakage Flow for Blades with Different Tip Squealer Geometries at Transonic Conditions," ASME Turbo Expo: Power for Land, Sea, and Air, Turbomachinery, Parts A and B, Orlando, FL, USA, 7, pp. 1051-1061.
- Jung, J., Kwon, O., Son, C., 2016, "An Investigation on Aerodynamics Loss Mechanism of Squealer Tips of a High Pressure Turbine Blade Using URANS," ASME TurboExpo: TurboMachinery Technical Conference and Exposition, Seoul, SK.
- Key, N.L., Arts, T., 2006, "Comparison of Turbine Tip Leakage Flow for Flat Tip and Squealer Tip Geometries at High-Speed Conditions," Journal of Turbomachinery, 128, pp. 213-220.
- Kim, J., Kang, Y.S., Kim, D., Lee, J., Cha, B.J., Cho, J., 2016, "Optimization of a High Pressure Turbine Blade Tip Cavity with Conjugate Heat Transfer Analysis," Journal of Mechanical Science and Technology, 30, pp. 5529-5538.
- Kim, J.H., Lee, S.Y., Chung, J.T., 2019, "Numerical Analysis of the Aerodynamic Performance & Heat Transfer of a Transonic Turbine with a Partial Squealer Tip," Applied Thermal Engineering, 152, pp. 878–889.
- Kline, S. J., and McClintock, F. A., 1953, "Describing Uncertainties in Single Sample Experiments," Mechanical Engineering, 75, pp. 3-8.
- Li, W., Jiang, H., Zhang, Q., Lee, S.W., 2014, "Squealer Tip Leakage Flow Characteristics in Transonic Condition," Journal of Engineering for Gas Turbines and Power, 136, pp. 042601/1-7.
- Ma, H., Zhang, Q., He, L., Wang, Z., Wang, L., 2017, "Cooling Injection Effect on a Transonic Squealer Tip-Part I: Experimental Heat Transfer Results and CFD Validation," Journal of Engineering for Gas Turbines and Power, 139, pp. 052506.
- Ma, H., Zhang, Q., He, L., Wang, Z., Wang, L., 2017, "Cooling Injection Effect on a Transonic Squealer Tip-Part II: Analysis of Aerothermal Interaction Physics," Journal of Engineering for Gas Turbines and Power, 139, pp. 052507.
- Moffat, R. J., 1988, "Describing the Uncertainties in Experimental Results," Experimental Thermal and Fluid Science, 1(1), pp. 3-17.

- O'Dowd, D. O., Zhang, Q., He, L., Ligrani, P. M., and Friedrichs, S., 2011, "Comparison of Heat Transfer Measurement Techniques on a Transonic Turbine Blade Tip," ASME Transactions-Journal of Turbomachinery, 133(2), pp. 021028-1 to 021028-10.
- O'Dowd, D., Zhang, Q., He, L., Oldfield, M.L.G., Ligrani, P.M., Cheong, B.C.Y., Tibbott, I., 2011, "Aerothermal Performance of a Winglet at Engine Representative Mach and Reynolds Numbers," Journal of Turbomachinery, 133, pp. 041026.
- O'Dowd, D.O., Zhang, Q., Usandizaga, I., He, L., Ligrani, P.M., 2010, "Transonic Turbine Blade Tip Aero-Thermal Performance with Different Tip Gaps: Part I-Tip Heat Transfer," Journal of Turbomachinery, 133, pp. 041027.
- Oldfield, M. L. G., 2008, "Impulse Response Processing of Transient Heat Transfer Gauge Signals," ASME Transactions-Journal of Turbomachinery, Vol. 130, No. 2, pp. 021023-1 to 021023-9.
- Sampson, M., Fairbanks, A., Moseley, J., Ligrani, P. M., Xu, H., and Fox, M., 2019, "Linear Cascade and Wind Tunnel Development for Turbine Blade Tip Heat Transfer Investigations With and Without Film Cooling," Paper Number GT2019-91074, ASME TURBO EXPO 2019: Turbomachinery Technical Conference and Exposition, Phoenix, Arizona, USA, June 17-21, 2019.
- Shyam, V., Ameri, A., Chen, J.P., 2011, "Analysis of Unsteady Tip and Endwall Heat Transfer in a Highly Loaded Transonic Turbine Stage," Journal of Turbomachinery, 134, pp. 041022.
- Thorpe, S.J., Yoshino, S., Thomas, G.A., Ainsworth, R.W., Harvey, N.W., 2005, "Blade-Tip Heat Transfer in a Transonic Turbine," Proceedings of the Institution of Mechanical Engineers, Part A, Journal of Power, 219, pp. 421-430.
- Virdi, A.S., Zhang, Q., He, L., Li, H.D., Hunsley, R., 2013, "Aerothermal Performance of Shroudless Turbine Blade Tips with Effects of Relative Casing Motion," Paper NoTBTS2013-2021, ASME Turbine Blade Symposium.
- Wang, B., Sandham, N., Hu, Z., Liu, W., 2015, "Numerical Study of Oblique Shock-Wave/Boundary-Layer Interaction Considering Sidewall Effects," Journal of Fluid Mechanics, 767, pp. 526-561.

- Wang, Z., Zhang, Q., Liu, Y., He, L., 2015, "Impact of Cooling Injection on the Transonic Over-Tip Leakage Flow and Squealer Aerothermal Design Optimization," *Journal of Engineering for Gas Turbines and Power*, 137, pp. 062603.
- Wheeler, A.P.S., Atkins, N.R., He, L., 2011, "Turbine Blade Tip Heat Transfer in Low Speed and High Speed Flows," *Journal of Turbomachinery*, 133, pp. 041025.
- Wheeler, A.P., Saleh, Z., 2013, "Effect of Cooling Injection on Transonic Tip Flows," *Journal of Propulsion and Power*, 29, pp. 1374-1381.
- Wheeler, A.P.S., Sandberg, R.D., 2013, "Direct Numerical Simulations of a Transonic Tip Flow with Free-Stream Disturbances," *ASME Paper TBTS2013-2037*.
- Zhang, Q., He, L., 2014, "Impact of Wall Temperature on Turbine Blade Tip Aerothermal Performance," *Journal of Engineering for Gas Turbines and Power*, 136, pp. 052602.
- Zhang, Q., He, L., Rawlinson, A., 2014, "Effects of Inlet Turbulence and End-Wall Boundary Layer on Aerothermal Performance of a Transonic Turbine Blade Tip," *Journal of Engineering for Gas Turbines and Power*, 136, pp. 052603–052603–7.
- Zhang, Q., O'Dowd, D. O., He, L., Oldfield, M. L. G., and Ligrani, P. M., 2011, "Transonic Turbine Blade Tip Aerothermal Performance with Different Tip Gaps - Part I: Tip Heat Transfer," *ASME Transactions-Journal of Turbomachinery*, Vol. 133, No. 4, pp. 041027-1 to 041027-9.
- Zhang, Q., O'Dowd, D. O., He, L., Wheeler, A. P. S., Ligrani, P. M., and Cheong, B. C. Y., 2011, "Overtip Shock Wave Structure and Its Impact on Turbine Blade Tip Heat Transfer," *ASME Transactions-Journal of Turbomachinery*, Vol. 133, No. 4, pp. 041001-1 to 041001-8.
- Zhong, F., Zhou, C., Ma, H., Zhang, Q., 2017, "Heat Transfer of Winglet Tips in a Transonic Turbine Cascade," *Journal of Turbomachinery*, 139, pp. 012605.
- Zhou, C., 2015, "Thermal Performance of Transonic Cooled Tips in a Turbine Cascade," *Journal of Propulsion and Power*, 31, pp. 1268-1280.



Zhu, D., Lu, S., Ma, H., Zhang, Q., Teng, J., 2017, Rotating Effect on Transonic Squealer Tip Cooling Performance,” ASME Turbo Expo, Turbomachinery Technical Conference and Exposition, Volume 5A: Heat Transfer, Charlotte, NC, USA.